Analysis of Heterogeneous Hydrological Properties of a Mountainous Hillslope Based on Intensive Observations

Naoya Masaoka

Graduate School of Agriculture, Kyoto University

2012

TABLE OF CONTENTS

ACKNOWLEDGEMENTS

CHAPTER 1

Introduction

1.1 General introduction

1.1.1 Heterogeneous hydrological properties of a mountainous hillslope

Hydrological phenomena in a mountainous hillslope include water supply from the upstream slope area, water movement within the foot slope area, and water discharge into a river channel. In a natural mountainous hillslope area, these phenomena are influenced by the heterogeneous hydrological properties in the area. That is, complex bedrock topography results in complicated subsurface water flow paths (e.g., Sammori et al., 1995; Freer et al., 2002). Stratified soil layers with various hydraulic properties affect the shape of the active water flow domain (Yamakawa et al., 2010). Preferential flow pathways, irregularly distributed in a slope, can flush large amounts of water rapidly (e.g., Uchida et al., 2002; Tsutsumi et al., 2005; Jones, 2010). Moreover, groundwater running through bedrock fractures supplies water to the soil layer, resulting in soil water flux that is unpredictable on the basis of surface topography alone (e.g., Onda et al., 2001; Montgomery et al., 2002; Kosugi et al., 2006, 2008; Katsura et al., 2008). Schematic illustrations of these heterogeneous hydrological properties are shown in Figure 1.1. These heterogeneous hydrological properties should be assessed to understand hydrological phenomena in the mountainous hillslope and their effects on water, sediment, energy, and nutrient transport.
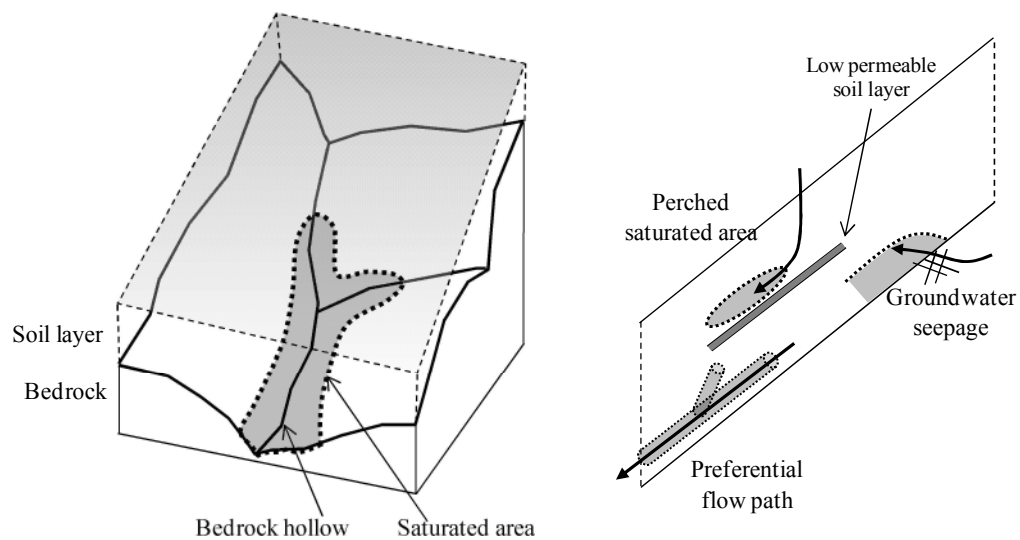
Figure 1.1 Schematic illustrations of the heterogeneous hydrological properties.

Numerical simulations of hillslope hydrological processes using a three-dimensional physics-based model have been proposed to predict runoff and the occurrence of shallow landslides (Wilkinson et al., 2002; Jones et al., 2008). If heterogeneous hydrological phenomena could be incorporated into models, the accuracy of runoff/landslide prediction would improve considerably. However, high-resolution and precise input parameters are required to reproduce heterogeneous hydrological phenomena using physics-based models.

Surface and subsurface topography as well as the distribution of soil thickness can be obtained with the soil penetration test (Okunishi and Iida, 1978; Okimura and Tanaka, 1980; McGlynn et al., 1999) to reproduce complicated subsurface water flow paths (Hopp and McDonnell, 2009). However, other parameters such as water supply and the distribution of soil hydraulic properties (e.g., saturated hydraulic conductivity, bulk density, and porosity) are difficult to obtain accurately due to their spatial heterogeneity. Water is supplied to the hillslope area not only by precipitation and lateral flow but also through groundwater seepage in bedrock fractures, which occur irregularly beneath the soil mantle and constantly supply water even in periods of no rainfall (Katsura et al., 2008; Kosugi et al., 2008). The distribution of soil hydraulic properties is often estimated from soil penetration resistance using a cone penetrometer. Penetration resistance reflects soil physical properties such as bulk density, porosity, and saturated hydraulic conductivity (Hiramatsu and Bitoh, 2001; Shanley et al., 2003; Wakatsuki et al., 2007). However, the accuracy of the estimate is insufficient to capture the local heterogeneity of hydraulic properties.

In contrast, the spatial distribution of water reflects the heterogeneity of hydrological phenomena. If detailed soil profile water distributions could be obtained in addition to penetration resistance, the location of groundwater seepage and the distribution of hydraulic properties could be estimated more precisely.

1.1.2 A combined penetrometer-moisture probe

The concept of a combined penetrometer-moisture probe (CPMP) has large potential to overcome these problems in investigating heterogeneous hydrological properties. The CPMP is a moisture sensor attached to a cone penetrometer that measures water content and penetration resistance in a soil profile. CPMPs have attracted a wide interest, particularly in agriculture. Vaz and Hopmans (2001) presented a basic construction and calibration technique. Topp et al. (2003) proposed detailed calibration equations through laboratory and field experiments. Moreover, other types of CPMPs with different moisture-measuring techniques have been developed (e.g., Sun et al., 2004; Lin et al. 2006). Because these CPMPs were designed for surveying agricultural soils, they have small

maximum measurable depths and are occasionally not robust enough to survey gravelly or rocky natural soils.

Kosugi et al. (2009) developed a new type of CPMP applicable to natural forested hillslopes where soils may be thick and include hard gravels and rocks. They proposed a calibration equation through a laboratory experiment and demonstrated that the new CPMP has sufficient robustness, measurable depth, and accuracy for in-field experiments. Using the new CPMP, Yamakawa et al. (2010) successfully detected spatial variation in the water table and stratified structures of loamy, sandy, and gravelly layers in a thick sediment deposit along a mountainous river channel. Kosugi et al. (2009) examined correlations between penetration resistance and water content as measured by the new CPMP at a natural hillslope.

Thus, the new CPMP has great potential for providing simultaneous measurements of water content and penetration resistance in natural forested hillslope soil. However, its applicability to investigate heterogeneous hydrological properties has not been shown by comparing the spatial distribution of penetration resistance and soil water content as well as spatial and temporal variations in pore water pressures densely observed by tensiometers.

1.1.3 Intensive and long-term observations of soil pore water pressure

Taking high-resolution, three-dimensional direct measurements of water flux using tensiometers are the most reliable way to analyze heterogeneous hydrological phenomena. Many tensiometers have been installed at the bedrock surface to cover a relatively broad area to detect water flow above the bedrock surface (Freer et al., 2002; Montgomery et al., 2002; Nishiguchi et al., 2005). However, these tensiometers are dispersed to cover a broad area, and thus provide insufficient spatial resolution to capture highly heterogeneous water movements. To date, intense observations using many tensiometers intended to analyze heterogeneous hydrological phenomena have not been conducted. The locations of heterogeneous hydrological phenomena should be detected before installing many tensiometers, because the observation area is limited in terms of time, cost, and effort. The spatial distribution of soil moisture throughout the entire study area should be investigated to detect the existence of heterogeneous hydrological properties hidden locally within a slope, which is often unrealistic due to the lack of a measurement technique. This is one reason behind the poor understanding of hydrological properties in hillslope areas.

Moreover, long-term water observations make it possible to capture the temporal variation in the hydraulic properties of a natural slope. Previous studies have suggested that specific heterogeneous hydrological phenomena vary in magnitude and position over time. Preferential pipe flow (e.g.,

Uchida et al., 2001; Jones, 2010) exhibits temporal variation in location and flow volume. Lateral water flow through preferential pipes contributes to subsurface soil erosion, which develops the pipe network (e.g., Tsukamoto et al., 1988; Brian and Jones, 1997; Holden, 2006). The improved drainage capacity within the enhanced pipe network may dissipate the perched water table during a rainfall event (McDonnell, 1990; Sidle et al., 1995). However, when the soil pipe is plugged, water readily fills the pipe cavity, leading to local elevation of soil pore water pressure in the surrounding soil matrix during a rainfall event. These concepts of pipe flow processes were estimated by relatively short-term pipe outlet discharge data or point-scale tensiometric data from field observations and have also been evidenced by bench scale experiments (e.g., Pierson, 1983). However, temporal variation in hydrological properties has not been observed directly in the field using long-term water movement measurements.

1.2 Objectives and the structure of this thesis

The heterogeneous hydrological properties hidden locally within a slope can be detected by the CPMP before installing the densely nested tensiometers. At the same time, the capability of the CPMP to survey heterogeneous hydrological properties can be evaluated by comparing to high-resolution water movement observed by tensiometers. The intensive observations will construct a physics-based model reproducing the heterogeneous hydrological phenomena occurring actually in natural mountainous hillslopes, because the input parameters such as water supply and hydraulic properties can be estimated more precisely from high-resolution water movement data. Moreover, intensive and long-term observations are possible to capture the temporal variation process of hydraulic properties, which have not been observed directly in natural hillslopes.

The aims of this study were to (1) detect heterogeneous hydrological phenomena using the new CPMP, (2) clarify the detailed three-dimensional water movement using a tensiometer nest, estimate the hydraulic properties inversely, and (3) investigate the temporal variation in hydrological properties using long-term observations. Figure 1.2 shows the study method.

As a study field, we focused on a foot slope area of the mountainous hillslope because the foot slope, forming the boundary zone between a hillslope and a river channel, is an area of active runoff generation. This area also plays an important role in sediment transport processes such as seepage erosion at a stream bank and resulting mass failure that supplies sediment into a river channel (Simon et al., 2000; Fox et al., 2007). Moreover, the foot slope regulates energy and nutrient fluxes between terrestrial and aquatic systems, greatly affecting river ecosystems (Gregory et al., 1991; Naiman and Decamps, 1997). All of these processes are dominantly controlled by the hydrological

Chapter 1

Introduction

Chapter 2

Materials and Methods

・ Basic information of study site

・ The structure of the new CPMP

Chapter 3

Application of a combined penetrometer-moisture probe for investigating heterogeneous hydrological properties of a foot slope area

・Comparison of the CPMP with tensiometer observation.

・ Evaluation of capability of the CPMP.

Chapter 4

Intensive three-dimensional water flow analysis using soil pore water pressure measurements and model calculation

・ 3D intensive observation of pore water pressure.

・ Model calculation to estimate hydraulic properties.

Chapter 5

The use of long-term intensive measurements of soil pore water pressure to analyze temporal variations in hydrological processes on a hillslope

・ Long-term observation of pore water pressure.

・ Analysis of water flow for 4 years.
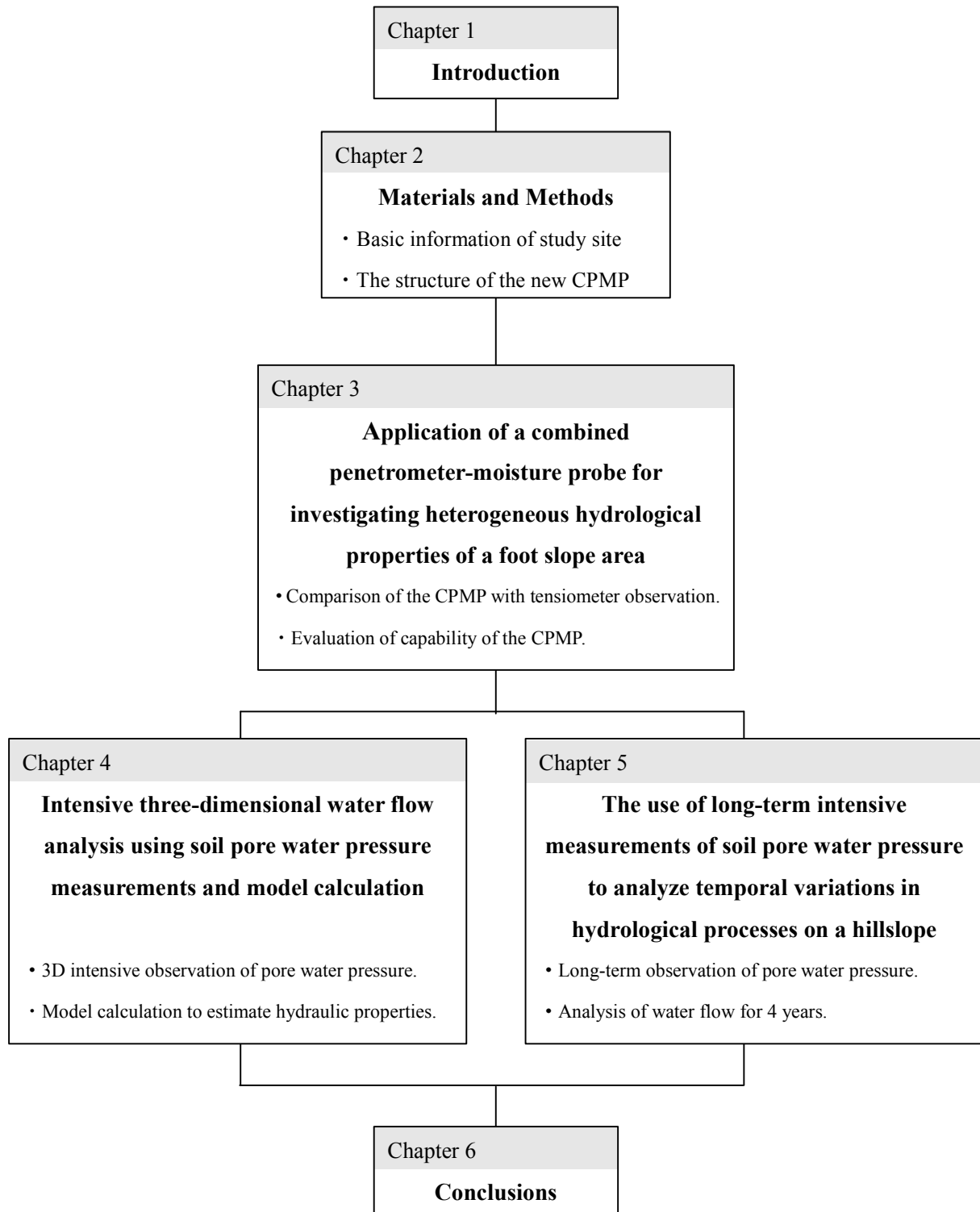
Chapter 6

Conclusions

Figure 1.2 Thesis structure.

properties in the foot slope area.

In Chapter 2, basic information of the study site is summarized, including location, topography, and soil parameters. The structure of the new CPMP is also explained. In Chapter 3, an evaluation of the performance of the CPMP technique for surveying heterogeneous hydrological properties is described. This included examining how CPMP data can be used to infer hydrological processes occurring in the foot slope area by comparing the spatial distributions of penetration resistance and soil water content as well as spatial and temporal variation in pore water pressures. In Chapter 4, the three-dimensional water movement induced by heterogeneous hydrological phenomena is presented in detail, based on field work using densely nested tensiometers. Estimations of the spatial distribution of the hydraulic properties using a physically based model calculation are also presented. Chapter 5 presents an analysis of the temporal variation in hydrological properties due to preferential channel development by the erosive action of lateral flow and weathering of fractured bedrock, based on long-term observation of pore water pressures over 4 years. Finally, Chapter 6 summarizes each chapter and provides a general conclusion of this thesis.

References

Bryan, R.B., and J.A.A. Jones. 1997. The significance of soil piping process: inventory and prospect. Geomorphology 20: 209-218.

Fox, G.A., G.V. Wilson, A. Simon, E.J. Langendoen, O. Akay, and J.W. Fuchs. 2007. Measuring streambank erosion due to ground water seepage: Correlation to bank pore water pressure, precipitation and stream stage. Earth Surf. Process. Landforms 32: 1558-1573, doi: 10.1002/esp.1490.

Freer, J., J.J. McDonnell, K.J. Beven, N.E. Peters, D.A. Burns, R.P. Hooper, B. Aulenbach, and C. Kendall. 2002. The role of bedrock topography on subsurface storm flow, Water Resour. Res. 38(12): 1269, doi: 10.1029/2001WR000872.

Gregory, S.V., F.J. Swanson, W.A. Mckee, and K.W. Cummins. 1991. An ecosystem perspective of riparian zones: focus on links between land and water. BioScience 41(8): 540-551.

Hiramatsu, S., and K. Bitoh. 2001. Study on easy set up method of input data to slope failure predicting model from a handy dynamic cone penetrometer. (In Japanese, with English abstract.) J. Jpn. Soc. Erosion Control Eng. 54: 12–21.

Holden, J. 2006. Sediment and particulate carbon removal by pipe erosion increase over time in blanket peatlands as consequence of land drainage. J. Geophys. Res. 111, F02010, doi: 10.1029/2005JF000386.

Hopp, L., and J.J. McDonnell. 2009. Connectivity at the hillslope scale: Identifying interactions between storm size, bedrock permeability, slope angle and soil depth. J. Hydrol. 376: 378-391, doi: 10.1016/j.jhydrol.2009.07.047.

Jones, J.A.A., E.A. Sudicky, and R.G. McLaren. 2008. Application of a fully-integrated surface-subsurface flow model at the watershed-scale: A case study. Water Resour. Res. 44. W03407, doi: 10.1029/2006WR005603.

Jones, J.A.A. 2010. Soil piping and catchment response. Hydrol. Process. 24: 1548-1566, doi: 10.1002/hyp.7634.

Katsura, S., K. Kosugi, T. Mizutani, S. Okunaka, and T. Mizuyama. 2008. Effects of bedrock groundwater on spatial and temporal variations in soil mantle groundwater in a steep granitic headwater catchment. Water Resour. Res. 44: W09430, doi: 10.1029/2007WR006610.

Kosugi, K., S. Katsura, M. Katsuyama, and T. Mizuyama. 2006. Water flow processes in weathered granitic bedrock and their effects on runoff generation in a small headwater catchment. Water Resour. Res. 42: W02414, doi: 10.1029/2005WR004275.

Kosugi, K., S. Katsura, T. Mizuyama, S. Okunaka, and T. Mizutani. 2008. Anomalous behavior of soil mantle groundwater demonstrates the major effects of bedrock groundwater on surface hydrological processes. Water Resour. Res. 44: W01407, doi: 10.1029/2006WR005859.

Kosugi, K., Y. Yamakawa, N. Masaoka, and T. Mizuyama. 2009. A combined penetrometer-moisture probe for surveying soil properties of natural hillslopes. Vadose Zone J. 8: 52-63, doi: 10.2136/vzj2008.0033.

Lin, C.P., S.H. Tang, and C.C. Chung. 2006. Development of TDR penetrometer through theoretical and laboratory investigations: 1. Measurement of soil dielectric permittivity. Geotech. Testing J. 29:306-321.

McDonnell, J.J. 1990. A rationale for old water discharge through macropores in a steep, humid catchment. Water Resour. Res. 26: 2821-2832.

McGlynn B.L., J.J. McDonnell, J.B. Shanley, and C. Kendall. 1999. Riparian zone flowpath dynamics during snowmelt in a small headwater catchment. J. Hydrol. 222:75-92.

Montgomery, D.R., W.E. Dietrich, and J.T. Heffner. 2002. Piezometric response in shallow bedrock at CB1: Implications for runoff generation and landsliding. Water Resour. Res. 38(12): 1274, doi: 10.1029/2002WR001429.

Naiman, R.J., and H. Decamps. 1997. The ecology of interfaces: Riparian zones. Annu. Rev. Ecol. Syst. 28: 621-658.

Nishiguchi Y., T. Uchida, T. Mizuyama, and K. Kosugi. 2005. An observation of spatial pore water pattern in a mountain hollow. (In Japanese, with English abstract.) J. Jpn. Soc. Erosion Cont.

Eng. 57(5): 53-58.

Okimura, T., and S. Tanaka. 1980. Researches on soil horizon of weathered granite mountain slope and failured surface depth in a test field. (In Japanese, with English abstract.) J. Jpn. Soc. Erosion Cont. Eng. 33(1):7–16.

Okunishi, K., and T. Iida. 1978. Study on the landslides around Obara village, Aichi prefecture (I)-Interrelationship between slope morphology, subsurface structure and landslides-. (In Japanese, with English abstract.) Bull. Disast. Prevent. Res. Instit. 21B:297-311.

Onda, Y., Y. Komatsu, M. Tsujimura, and J. Fujihara. 2001. The role of subsurface runoff through bedrock on storm flow generation. Hydrol. Process. 15:1693-1706, doi: 10.1002/hyp.234.

Pierson, T.C. 1983. Soil pipes and slope stability. Quality J. Engineering Geol. 16: 1-11.

Sammori, T., Y. Ohkura, H. Ochiai, and H. Kitahara. 1995. Effects of Soil Depth on Rain-induced Landslide. (In Japanese, with English abstract.) J. Jpn. Soc. Erosion Cont. Eng. 48(1):12-23.

Shanley, J.B., K.N. Hjerdt, J.J. McDonnell, and C. Kendall. 2003. Shallow water table fluctuations in relation to soil penetration resistance. Ground Water 41(7):964-972.

Sidle, R.C., Y. Tsuboyama, S. Noguchi, I. Hosoda, M. Fujieda, and T. Shimizu. 1995. Seasonal hydrologic response at various spatial scales in a small forested catchment, Hitachi Ohta. J. Hydrol. 168: 227-250.

Simon, A., A. Curini, S.E. Darby, and E.J. Langendoen. 2000. Bank and near-bank processes in an incised channel. Geomorphology 35:193-217.

Sun, Y., P.S. Lammers, and D. Ma. 2004. Evaluation of a combined penetrometer for simultaneous measurement of penetration resistance and soil water content. J. Plant Nutr. Soil Sci. 167:745-751, doi: 10.1002/jpln.200421365.

Topp, G.C., J.L. Davis, and A.P. Annan. 1980. Electromagnetic determination of soil water content: Measurements in coaxial transmission lines. Water Resour. Res. 16:574–582.

Tsukamoto, Y., H. Minematsu, and I. Tange. 1988. Pipe development in hillslope soils in humid climate. Rolling Land Res. 6: 268-280 (in Japanese with English summary).

Tsutsumi, D., R.C. Sidle, and K. Kosugi. 2005. Development of a simple lateral preferential flow model with steady state application in hillslope soils. Water Resour. Res. 41, W12420, doi: 10.1029/2004WR003877.

Uchida, T., K. Kosugi, and T. Mizuyama. 2001. Effects of pipeflow on hydrological process and its relation to landslide: a review of pipeflow studies in forested headwater catchments. Hydrol. Process. 15: 2151-2174, doi: 10.1002/hyp.281.

Uchida, T., K. Kosugi, and T. Mizuyama. 2002. Effects of pipeflow and bedrock groundwater runoff generation at a steep headwater catchment, Ashiu, central Japan. Water Resour. Res. 38(7) doi:

10.1029/2001WR000773.

Vaz, C.M.P., and J.W. Hopmans. 2001. Simultaneous measurements of soil penetration resistance and water content with a combined penetrometer-TDR moisture probe. Soil Sci. Soc. Am. J. 65:4-12.

Wakatsuki, T., Y. Sasaki, Y. Tanaka, and Y. Matsukura. 2007. Predictive equation of unit weights, shear-strength parameters and permeability of grus using by simplified dynamic cone penetrometer hardness and grain size. (In Japanese, with English abstract.) J. Jpn. Soc. Erosion Cont. Eng. 59(6):38-46.

Wilkinson, P.L., M.G. Anderson, and D.M. Lloid. 2002. An integrated hydrological model for rain-induces landslide prediction. Earth Surf. Process. Landforms 27: 1285-1297, doi: 10.1002/esp.409.

Yamakawa, Y., K. Kosugi, N. Masaoka, Y. Tada, and T. Mizuyama. 2010. Use of combined penetrometer-moisture probe together with geophysical methods to survey hydrological properties of a natural slope. Vadose Zone J. 9:768-779, doi: 10.2136/vzj2010.0012.

CHAPTER 2

Materials and Methods

2.1 Study site

2.1.1 Hirudani experimental basin

All observations in this thesis were performed in a headwater basin of the Hirudani experimental basin in the Hodaka Sedimentation Observatory of Disaster Prevention Research Institute, Kyoto University in Gifu, central Japan (36°15'N, 137°35'E; Fig. 2.1). The Hirudani experimental basin is located in a headwater area of the Jintsu River, where many studies of sediment discharge and transport have been conducted (e.g., Fujita et al., 2002). The basin area is 0.85 km^2. The mean annual air temperature is 9.5°C, and the mean annual precipitation is 1980 mm, a quarter of which falls as snow in winter (1979 to 2010, Japan Meteorological Agency).
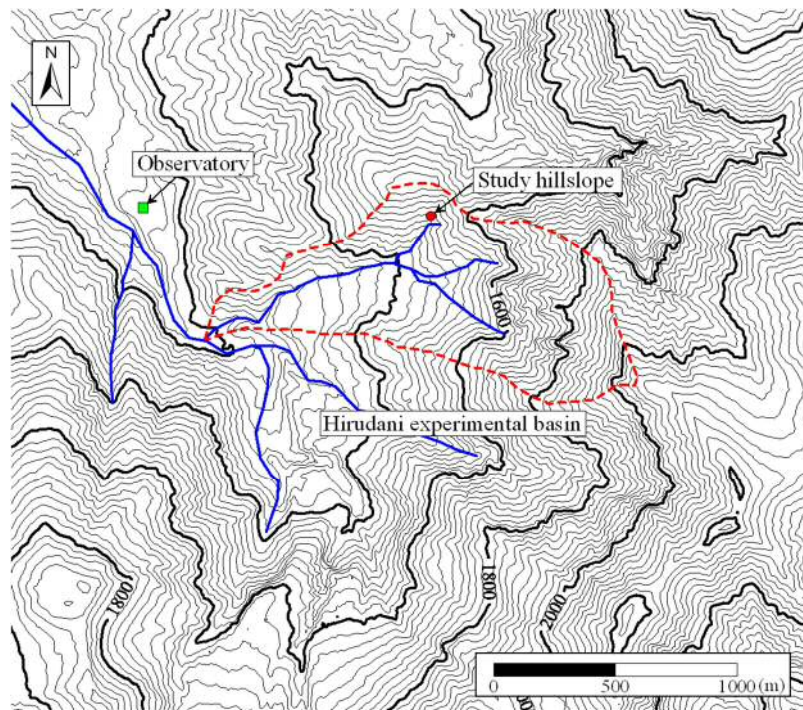
Figure 2.1 Map of Hirudani experimental basin and study hillslope.
Broken line indicates the watershed boundary.
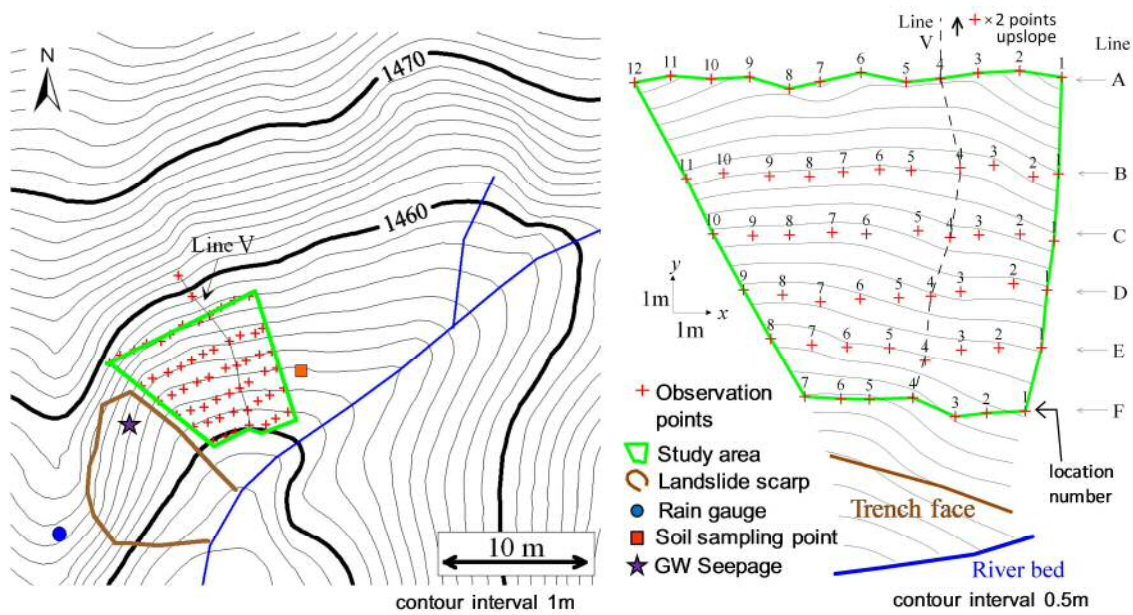
Figure 2.2 Left panel: map of the study area located at the foot of a valley-side slope. Right panel: enlarged map of the study area showing observation points along six horizontal lines (Lines-A to F) and one perpendicular line (Line-V).
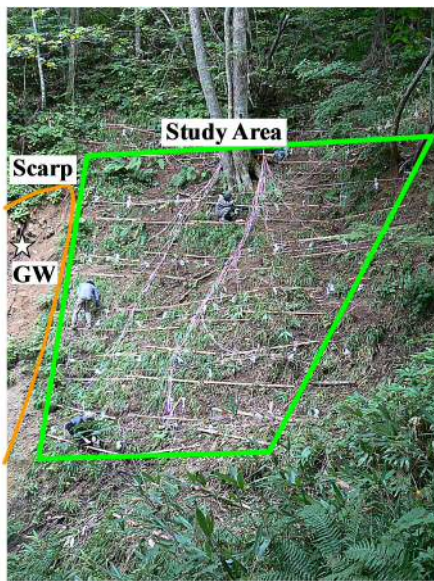
Figure 2.3 Photograph of the study area, landslide scarp, and groundwater seepage point.

As shown in Figures 2.2 and 2.3, the study area is located at a foot of the valley-side slope. In the area within a horizontal distance of 2 m from the stream channel, soil is always wet up to the ground surface by return flow. The study area, with a mean gradient of 40° and elevation ranging from 1450 to 1460 m above sea level, is underlain by weathered granite porphyry and covered by shrubs, ferns, and herbaceous species. The soil is classified as Cambisol (brown forest soil). The surface topography across the slope is planar and gently concave. An old landslide scarp is adjacent to the slope and a bedrock groundwater spring is located inside the scarp.

2.1.2 Soil parameters for the study site

To examine the correlations between soil characteristics and penetration resistance (i.e., N_c value), we conducted a cone penetration test at a point near the study hillslope area (left panel in Fig. 2.2; denoted as soil sampling point) with a Hasegawa-type penetrometer (Nishimura et al., 1987). After the penetration test, we collected 100 cm³ soil core samples by digging a pit (two samples from each four depths). For each soil sample, the saturated hydraulic conductivity, K_s, was measured using the falling-head test (Reynolds et al., 2002). In addition, we determined the water retention curve (i.e., the relationship between ψ and θ) in the range of -200<ψ<0 cm by the pressure plate method (Dane and Hopmans, 2002) for each soil sample.

Figure 2.4 shows the vertical distributions of N_c and K_s. The soil horizonation at the soil-sampling pit is denoted by the background colors in the figure. The A and B horizons were observed at 0–47 cm and the C horizon was below 47 cm. The groundwater table appeared at 80 cm. N_c sharply increased to more than 30 at approximately 47 cm depth, corresponding to the boundary between the B and C horizons. Therefore, here we refer to the layer between the surface and the depth of N_c=30 as the "surface soil layer" and the layer from the surface soil layer to the bedrock surface as the "subsurface soil layer." K_s exhibited a sharp contrast between the surface and subsurface layers, showing a negative correlation with N_c as also found in previous studies (e.g., Hiramatsu and Bitoh, 2001; Shanley et al., 2003; Wakatsuki et al., 2007). In the surface soil layer, K_s ranged from 0.13 to 0.91 cm/sec, which was two to four orders of magnitude greater than the range of 7.0×10^{-5} to 3.9×10^{-3} cm/sec in the subsurface soil layer.
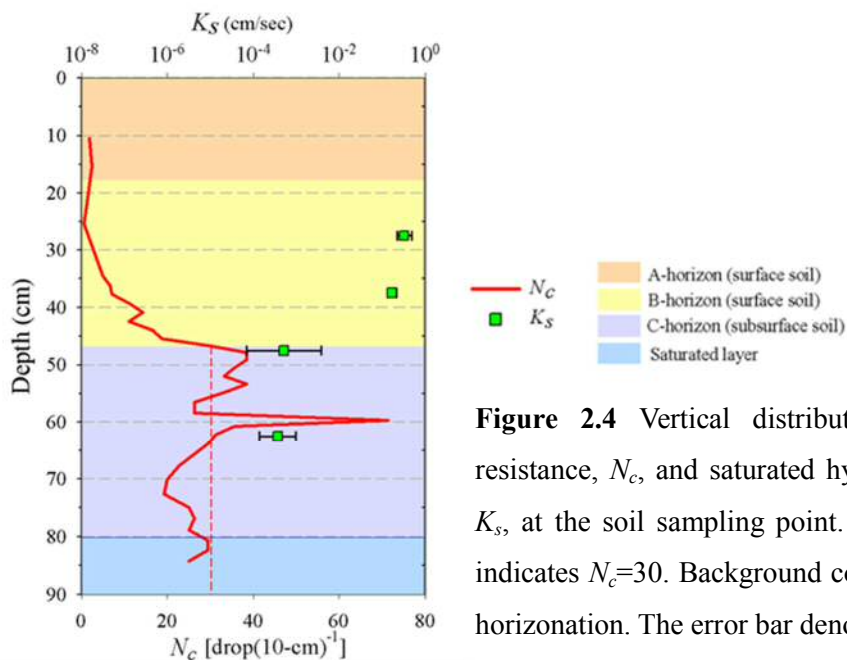
Figure 2.4 Vertical distributions of penetration resistance, N_c, and saturated hydraulic conductivity, K_s, at the soil sampling point. The broken red line indicates N_c=30. Background colors indicate the soil horizonation. The error bar denotes standard error.
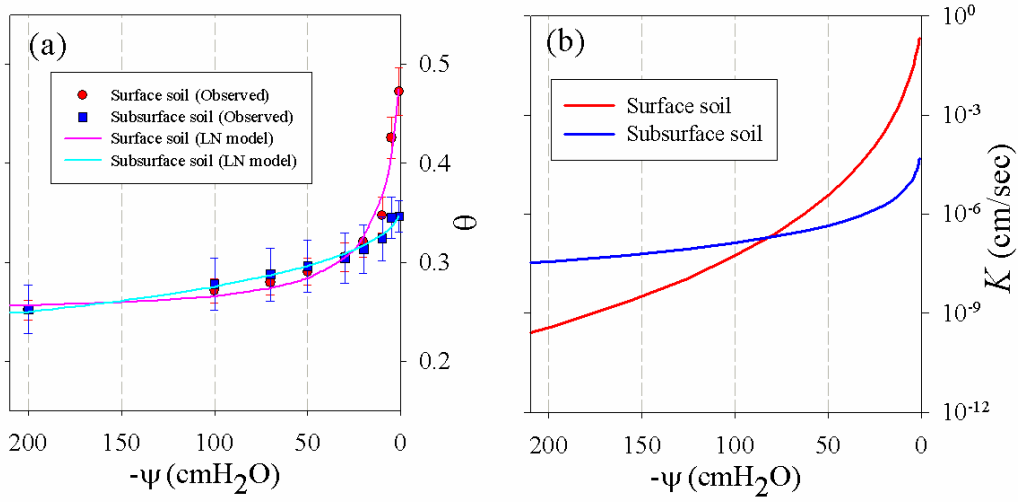
Figure 2.5 (a) Observed water retention, ψ-θ, data and functional ψ-θ curves fitted by the lognormal distribution (LN) model, and (b) functional hydraulic conductivity, K-ψ, curves of surface soil and subsurface soil in the range of -200<ψ<0 cm. The error bar denotes standard error.

The plots in Figure 2.5a is ψ-θ values observed in the range of -200<ψ<0 cm. For each layer, the volumetric water content, θ, was an average value of four samples. The surface soil showed greater θ_s than the subsurface soil. In the relatively wet range, the surface soil exhibited a steep decline in θ while the subsurface soil exhibited a gentle decline. As a result, the surface soil showed lower values of θ than the subsurface soil in the range of -100<ψ<-30 cm.

The observed retention data (in the range of -200<ψ<0 cm) were successfully fitted by the lognormal distribution (LN) model (Kosugi, 1996):

$$S_e = \frac{\theta - \theta_r}{\theta_s - \theta_r} = Q\left[\frac{\ln(\psi/\psi_m)}{\sigma}\right] \qquad [2\text{-}1]$$

where S_e represents the effective saturation, θ_s and θ_r are the saturated and residual volumetric water contents, respectively, ψ_m is the pressure head at S_e=0.5, σ is a dimensionless parameter characterizing the width of the pore radius distribution, and Q is the complementary normal distribution function defined as

$$Q(x) = \int_x^\infty \frac{1}{(2\pi)^{1/2}} \exp\left(-\frac{u^2}{2}\right) du \qquad [2\text{-}2]$$

The functional ψ-θ curves (Fig. 5a) expressed by Eq. [2-1] were derived by optimizing the parameters θ_r, ψ_m, and σ, while θ_s was fixed at the average of observed values. For the surface layer, θ_s=0.47,

θ_r=0.25, ψ_m=-10.6 cm, and σ=1.46. For the subsurface layer, θ_s=0.35, θ_r=0.05, ψ_m =-714 cm, and σ=2.78. Figure 5a shows that the plots of Eq. [2-1] fit the observed data well.

The hydraulic conductivity function, $K(\psi)$, was estimated by substituting the optimized ψ_m and σ values into the following equation (Kosugi, 1996):

$$K(\psi) = K_s S_e^{1/2} \left\{ Q \left[\frac{\ln(\psi / \psi_m)}{\sigma} + \sigma \right] \right\}^2 \qquad [2\text{-}3]$$

where the saturated hydraulic conductivity, K_s, was fixed at the geometric mean of the four samples for each soil layer. Figure 2.5b shows the plots of Eq. [2-3] in the range of -200<ψ<0 cm. Although K_s of the surface soil was larger than that of the subsurface soil by three orders of magnitude, the surface soil exhibited a steep decline in K in the relatively wet range, resulting in lower K values than those of subsurface soil in the range of ψ<-80 cm. This trend follows the results of a previous study (Hendrayanto et al., 1999) which compared K-ψ curves of surface and subsurface soils in a headwater catchment underlain by weathered granite.

2.2 The combined penetrometer-moisture probe

The combined penetrometer-moisture probe (CPMP) (Kosugi et al., 2009) consists of a moisture probe attached to a cone penetrometer (Hasegawa-type penetrometer) with a 60°bit, a cone diameter of 20 mm, a weight of 2 kg, and a fall distance of 50 cm (Fig. 2.6). Operation of the penetrometer involves a weight free-falling along a guide shaft to strike a knocking head that drives the cone into the soil. The penetration resistance, N_c, is calculated as the number of blows required for 10 cm of penetration. The CPMP produced about the same N_c values as the Hasegawa-type penetrometer (Kosugi et al., 2009).

Volumetric water content, θ, was measured using a detachable TDR moisture probe: two stainless wires (ground and conductor wires) coiled around an acrylic column to guide an electromagnetic wave act as a sensor detecting the water content. The coil-type waveguides have a major advantage in that they are markedly longer than the probe itself; they also provide high resolution and a small volume of influence. The wires are embedded in grooves on the acrylic column and glued with epoxy resin to prevent breakdown of the moisture sensor during penetration through gravelly and rocky soils. The wave guides connected with the coaxial cable are passed through the hollow penetrometer rod and connected to a time domain reflectometer.

Kosugi et al. (2009) showed that profiles of θ measured by the CPMP were about the same as those measured by the conventional gravimetric method, proving that the CPMP can establish
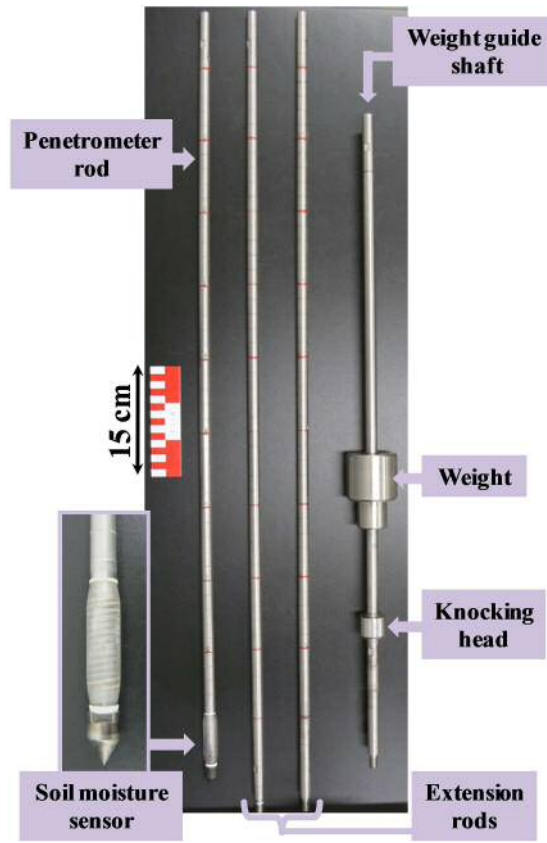
Figure 2.6 Photographs of the combined penetrometer-moisture probe (CPMP), showing the weight guide shaft with the weight and knocking head, two extension rods, and penetrometer rod with soil moisture sensor.

sufficient contacts between the waveguides and surrounding soils and, thus, provide reliable water content measurements. In field experiments, the CPMP measurements have been successfully conducted down to a depth of 482 cm by using the extension rods (Kosugi et al., 2009; Yamakawa et al., 2010).

The time domain reflectometer, TDR100, and PCTDR software ver. 2.0 (Campbell Scientific, Logan, UT, USA) were used for measurements of the dielectric constant. We derived θ from the observed square root of dielectric constant with CPMP, ξ, using the empirical relationship between ξ and θ, uniquely developed by laboratory calibration experiments (Kosugi et al., 2009). In the experiments, CPMP was inserted into a plastic container filled with soil and then the value of ξ was measured. After the measurements, the θ of the soil was obtained by the gravimetric method. These procedures were repeated for several increments of increasing soil water content. The whole measured

plots fit a single calibration curve very well, which is expressed by the following sixth-order polynomial equation:

$$\theta = (2.127491 \times 10^{-2})\xi^6 - (3.897577 \times 10^{-1})\xi^5 + (2.843453)\xi^4$$
$$- (10.47385)\xi^3 + (20.28508)\xi^2 - (19.04845)\xi + (6.571050)$$

[2-4]

This empirical relationship expressed in Eq. [2-4] produced satisfactory results also for field experiments (Kosugi et al., 2009).

References

Dane, J.H., and J.W. Hopmans. 2002. Water retention and storage: Laboratory. p. 688-690. *In* J.H. Dane and G.C. Topp (ed.) Methods of soil analysis. Part 4. SSSA Book Ser. 5. SSSA, Madison, WI.

Fujita, M., T. Sawada, and T. Mizuyama. 2002. Monitoring of sediment movement in a small mountain watershed. p. 33-40. *In* Congress publ.1. INTERPRAEVENT 2002 in the Pacific Rim, 14-18 October 2002. Matsumoto. Japan.

Hendrayanto, K. Kosugi, T. Uchida, S. Matsuda, and T. Mizuyama. 1999. Spatial variability of soil hydraulic properties in a forested hillslope. J. For. Res. 4: 107-114.

Hiramatsu, S., and K. Bitoh. 2001. Study on easy set up method of input data to slope failure predicting model from a handy dynamic cone penetrometer. (In Japanese, with English abstract.) J. Jpn. Soc. Erosion Control Eng. 54: 12–21.

Kosugi, K. 1996. Lognormal distribution model for unsaturated soil hydraulic properties. Water Resour. Res. 32(9): 2697-2703.

Kosugi, K., Y. Yamakawa, N. Masaoka, and T. Mizuyama. 2009. A combined penetrometer-moisture probe for surveying soil properties of natural hillslopes. Vadose Zone J. 8: 52-63, doi: 10.2136/vzj2008.0033.

Nishimura, N., M. Senge, and H. Isozaki. 1987. Estimation of dynamic bearing capacity from the dynamic penetration tests and the influence of soil layer on its tests. (In Japanese, with English abstract.) Res. Bull. Fac. Agric. Gifu Univ. 52: 265-272.

Reynolds, W.D., D.E. Elrick, E.G. Youngs, H.W.G. Booltink, and J. Bouma. 2002. Saturated and field-saturated water flow parameters: Laboratory methods. p. 802–817. *In* J.H. Dane and G.C. Topp (ed.) Methods of soil analysis. Part 4. SSSA Book Ser. 5. SSSA, Madison, WI.

Shanley, J.B., K.N. Hjerdt, J.J. McDonnell, and C. Kendall. 2003. Shallow water table fluctuations in relation to soil penetration resistance. Ground Water 41(7):964-972.

Wakatsuki, T., Y. Sasaki, Y. Tanaka, and Y. Matsukura. 2007. Predictive equation of unit weights, shear-strength parameters and permeability of grus using by simplified dynamic cone penetrometer hardness and grain size. (In Japanese, with English abstract.) J. Jpn. Soc. Erosion Cont. Eng. 59(6):38-46.

Yamakawa, Y., K. Kosugi, N. Masaoka, Y. Tada, and T. Mizuyama. 2010. Use of combined penetrometer-moisture probe together with geophysical methods to survey hydrological properties of a natural slope. Vadose Zone J. 9:768-779, doi: 10.2136/vzj2010.0012.

CHAPTER 3

Application of a combined penetrometer-moisture probe for investigating heterogeneous hydrological properties of a foot slope area

3.1 Introduction

A combined penetrometer-moisture probe (CPMP), which is a moisture sensor attached to the cone penetrometer providing ready measurements of water content and penetration resistance in a soil profile, has attracted a wide interest especially in the discipline of agriculture. The fundamental ideas of the CPMP have been proposed in recent years. Vaz and Hopmans (2001) presented basic construction and calibration technique. Topp et al. (2003) proposed detailed calibration equations through laboratory and in-field experiments. Moreover, other types of the CPMP having different moisture measuring techniques have been developed (e.g. Sun et al., 2004; Lin et al. 2006). Because these CPMPs were designed for surveying agricultural soils, they have small maximal measurable depths and sometimes they are not robust enough for surveying gravelly or rocky natural soils.

In the latest study, Kosugi et al. (2009) developed a new type of CPMP applicable to natural forested hillslopes where soils may be thick and include hard gravels and rocks (Fig. 2.6). They proposed a calibration equation through laboratory experiment, and proved that the new CPMP has enough robustness, measurable depth, and accuracy in moisture measuring through in-field experiments. Using the new CPMP, Yamakawa et al. (2010) successfully detected spatial variations in the water table and stratified structures of loamy, sandy, and gravelly layers in a thick sediment deposit along a mountainous river channel. Kosugi et al. (2009) examined correlations between penetration resistance and water content measured by the new CPMP at a natural hillslope.

In this chapter, we applied the new CPMP for investigating hydrological properties in a foot slope of mountainous hillslopes. For assessments of heterogeneous hydrological properties, it is potentially useful to survey spatial distributions of soil water content and of soil resistance obtained by a penetration test. The soil penetration resistance is generally used in hydro-geomorphological surveys for measuring soil mantle structure as well as bedrock topography (Okunishi and Iida, 1978; Okimura and Tanaka, 1980; McGlynn et al., 1999). The penetration resistance also reflects soil physical properties such as bulk density, porosity, and saturated hydraulic conductivity (Hiramatsu and Bitoh, 2001; Shanley et al., 2003; Wakatsuki et al., 2007). On the other hand, the spatial distribution of soil water content reflects heterogeneity in hydrological properties, such as flux convergence affected by bedrock topography, bedrock groundwater seepage, and water flow along preferential pathways. In

addition, the distribution of hydraulic properties in soil mantles can be estimated inversely from the spatial distribution of soil water content.

In recent years, soil water content has been conveniently measured using newly developed techniques such as time domain reflectometry (TDR; Topp et al., 1980) and electrostatic capacitance meters (Starr and Paltineanu, 1998). However, to detect heterogeneous hydrological properties hidden locally within a slope, a large number of closely spaced moisture sensors must be installed throughout the entire study area, which is often unrealistic in terms of time, cost, and effort. This is one reason behind the poor understanding of hydrological properties in foot slope areas.

The new CPMP (Kosugi et al., 2009), which enables more time- and cost-effective measurement of soil water content and its distribution, has a large potential to overcome this problem. That is, high spatial resolution data of both soil water content and penetration resistance obtained by the CPMP over a wide area of foot slope can provide effective information about the heterogeneous hydrological properties of the foot slope area.

In this chapter, we applied the CPMP technique to a foot slope area of a mountainous hillslope. The goal was to evaluate the capability of the CPMP to survey heterogeneous hydrological properties. At the same foot slope area, we continuously monitored soil pore water pressures using densely nested tensiometers. By comparing the spatial distributions of penetration resistance and soil water content as well as spatial and temporal variations in pore water pressures, we examined how CPMP data can be used to infer hydrological processes occurring in the foot slope area under no-rainfall conditions and during a storm event.

3.2 Materials and Methods

3.2.1 CPMP observation

We conducted observations with the CPMP at 57 points along six horizontal lines referred to as Lines-A to F from the top of the slope down (right panel in Fig. 2.2). Each line had seven to 12 points located at roughly 1-m intervals. Each point was named by the line name and the location number; for example, point F-1 indicates the point on the Line-F that has the location number of 1 (right panel in Fig. 2.2). The observations were conducted from 7 to 11 August 2007. Rainfall amount was 31 and 40 mm during antecedent seven and fourteen days, respectively. No rainfall was gauged during antecedent three days.

Using the CPMP, we measured the vertical profiles of volumetric water content, θ, and penetration resistance, N_c, at each of 57 points. We conducted the penetration tests until we reached the apparent soil-bedrock interface at all observation points. Vertical measuring intervals varied from

approximately 0.5 to 10 cm depending on the penetration length of each blow.

Previous studies have suggested various N_c values indicative of the soil-bedrock interface in granitic regions, most of which ranged from 60 to 100 (e.g. Okunishi and Iida, 1978; Terajima and Moroto, 1990; Ohsaka et al., 1992; Hasegawa, 2006). These N_c values were estimated by excavating soil profiles in the vicinity for observing stratified soil structures and elongation depths of tree roots. Among recent studies, Katsura et al. (2005) and Kosugi et al. (2006) demonstrated that a layer with an N_c value exceeding 100 clearly corresponded to the soil-bedrock interface by comparing N_c values and photographs of the soil-bedrock profile. Based on these previous studies, we conducted the penetration test down to the depths where N_c exceeded 100.

For drawing contour maps for N_c and θ spatial distributions, observed data ware interpolated by kriging analysis using Surfer software ver. 8 (Golden Software, Golden, CO, USA).

3.2.2 Tensiometer observation

From 28 May to 18 November 2008, we continuously monitored soil pore water pressure (soil matric pressure head, ψ) at the soil-bedrock interface. Fifty-seven tensiometers attached to Copal Electronics PA-850-102V-NGF pressure transducers (Copal Electronics, Shinjuku, Tokyo, Japan) were installed at all points of CPMP observation. Values for ψ were recorded at 5-min intervals throughout the observation period using a data logger (CR1000, Campbell Scientific, Logan, UT, USA). After 21 August 2008 in the observation period, we monitored ψ with an extra 24 tensiometers in addition to the original 57 tensiometers. Two extra tensiometers were installed at the soil-bedrock interface at two upslope points along Line-V (Fig. 2.2). Fourteen extra tensiometers were installed in shallow layers along Lines-C and V, and the other eight were installed in middle layers along Lines-C and V. All the shallow tensiometers were installed at a depth of 30 cm. The middle tensiometers were installed between the shallow and deep tensiometers at 80 to 160 cm depth. A rain gauge was placed in an open space on the ridge near the study hillslope (left panel in Fig. 2.2).

3.3 Results and Discussion

3.3.1 Measuring water content and penetration resistance with the CPMP

Figure 3.1 shows the obtained vertical distributions of N_c and θ at points B-4 and C-6 as example data for each observation point. At B-4, N_c started to increase gradually from a depth of approximately 70 cm and then sharply increased at 120 cm. It decreased to 10 at a depth of 150 cm, but increased again and exceeded 100 at 169 cm, indicating the soil-bedrock interface. Although θ
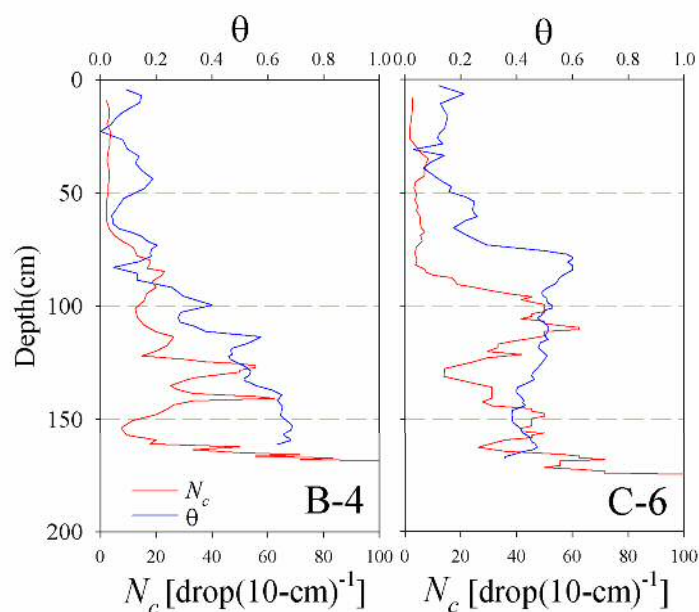
Figure 3.1 Vertical distributions of penetration resistance, N_c, and water content, θ, obtained by the CPMP observations at points B-4 and C-6.

started to increase gradually from a depth of 70 cm, similar to N_c, it kept increasing toward the bedrock surface. At C-6, on the other hand, N_c sharply increased at approximately 80 cm depth, indicating a clear boundary between the surface and subsurface soil layers. Below the sharp increase, N_c mostly stayed around 30 with only small fluctuations and exceeded 100 at a depth of 175 cm. θ also jumped to 0.6 at a depth of approximately 75 cm. However, below this peak value, it decreased slightly and progressively toward the bedrock.

As illustrated in Figure 3.1, the characteristics of N_c and θ distribution varied spatially from point to point within a relatively narrow study area. This is more clearly depicted in Figure 3.2, which maps the spatial distributions of N_c and θ in vertical cross-sections of Lines-A to F. The top edge of each cross-section indicates the ground surface and the bottom edge indicates the soil-bedrock interface determined by N_c values exceeding 100. Soil thickness over the whole slope ranges from 22 (at A-9) to 250 cm (at C-4). The boundary between the surface and subsurface soil layer (i.e., the line of N_c=30) is shown by brown lines in each cross-section. Within the area of Line-A, soil thickness varied considerably among the observation points and bedrock topography was complex. Almost the whole area had dry conditions (θ<0.2). In Line-B, a bedrock hollow was detected near B-5. A thick subsurface soil layer (N_c>30) was distributed inside the hollow, where θ showed high values (θ>0.5). In Line-C, bedrock hollowed from C-3 to 7, where a thick subsurface soil layer was distributed. At C-4
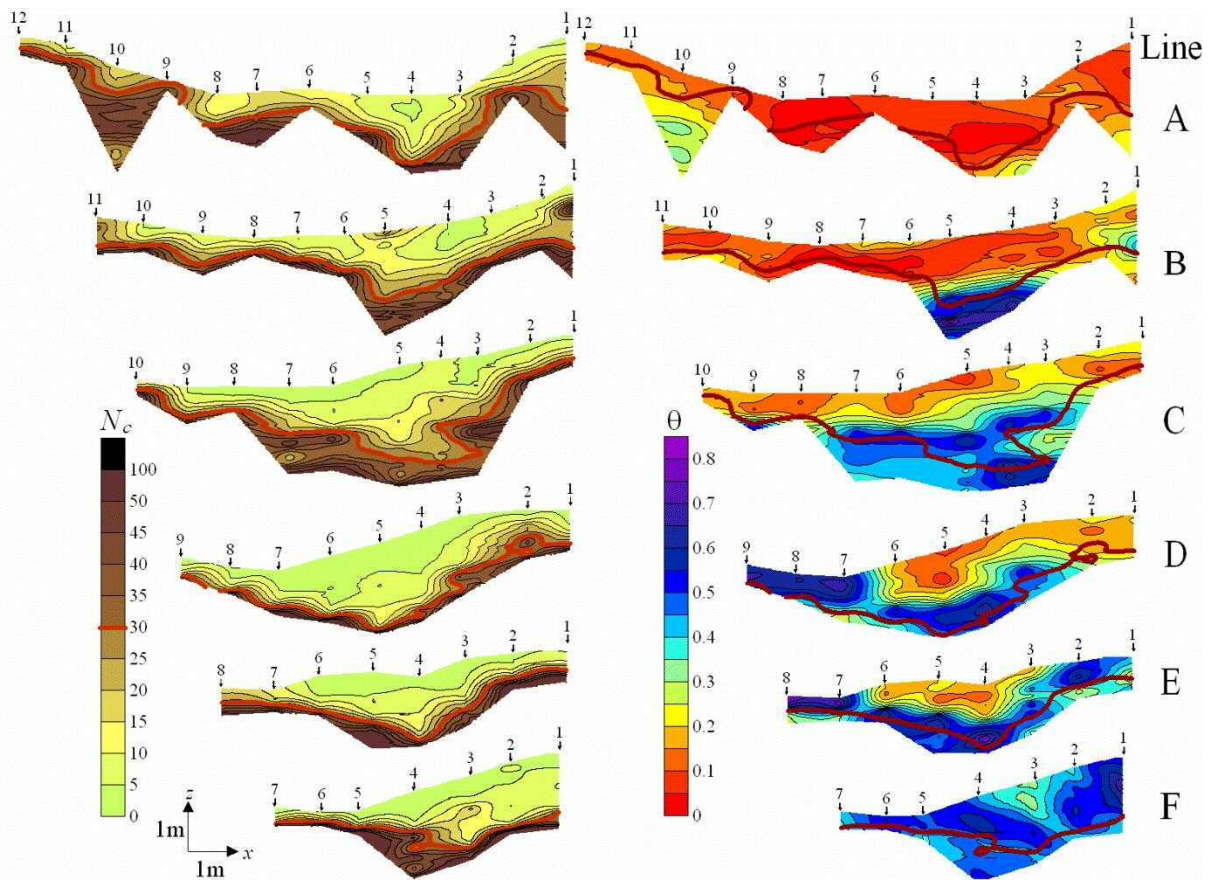
Figure 3.2 Spatial distribution maps of penetration resistance, N_c, and water content, θ, in vertical cross-sections of Lines-A to F. The top edge of each cross-section indicates the ground surface and the bottom edge indicates the soil-bedrock interface determined by N_c exceeding 100. Brown lines denote the boundary line of surface and subsurface soil layer (i.e., the line of N_c=30).

and 5, the surface soil layer (N_c<30) was relatively thick. From C-3 to 7, a region of high θ was distributed horizontally in the middle part of the soil profile. Above the soil-bedrock interface, θ showed high values at C-3 and 4 compared to at C-5, 6, and 7. High θ values were also detected at C-9. In Line-D, the subsurface soil layer was relatively thin. At D-3 through D-6, the high θ region was mostly distributed above the soil-bedrock interface. From D-7 through D-9, θ was high at all depths. In Line-E, the high θ region was distributed within the bedrock hollow from E-3 through E-6. On both sides of the line, the surface soil layer showed high θ values. In Line-F, a bedrock hollow was detected near F-4, where a thick subsurface soil layer was distributed. Most of the area showed wet conditions.

3.3.2 Relationship between topography and water content distribution

3.3.2.1 Surface and bedrock topographies

Figure 3.3a shows a topographic map of the ground surface. The ground surface has planar and low relief topography. Figure 3.3b presents the bedrock topography and soil thickness distribution map. The soil thickness showed heterogeneous distribution: a thick soil layer (over 1 m in thickness) was distributed along a line from A-4 to F-4 in a longitudinal direction, which clearly followed the hollow shape of the bedrock topography.

For quantitative evaluations of surface and bedrock topographies, we conducted digital terrain analysis by calculating the topographic index (Beven and Kirkby, 1979) for the areas shown in Figures 3.3a and 3.3b. The topographic index is defined as $\ln(a/\tan\beta)$, where a (m^2) is the upslope accumulated area and $\tan\beta$ is the local slope angle. The topographic index is used to theoretically estimate the accumulated flow at any point and approximate the likely distribution of variable source areas. We calculated the topographic indices of surface and bedrock topographies for the CPMP observation area using the multiple direction flow algorithm of Quinn et al. (1995) from 0.2 m grid data interpolated from the obtained topographic data.
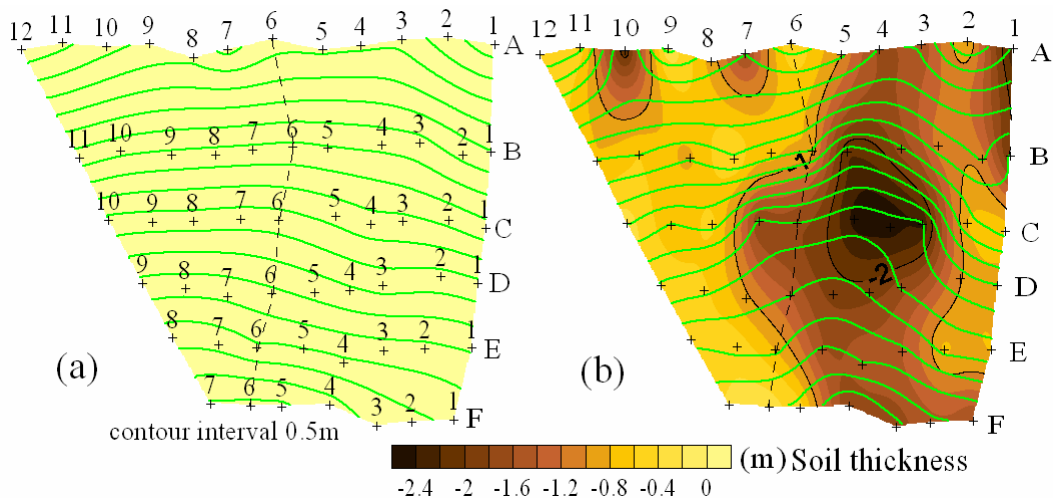
Figure 3.3 (a) Ground surface topographic map and location number of all observation points. (b) Bedrock surface topographic map and soil thickness distribution. (c) Topographic map and topographic index distribution of the ground surface. (d) Topographic map and topographic index distribution of the bedrock surface. Contour interval of each topographic map is 0.5 m. The broken line is a marker which connects the location number '6' in each line. The definition of each symbol is denoted in legend of Figure 9.
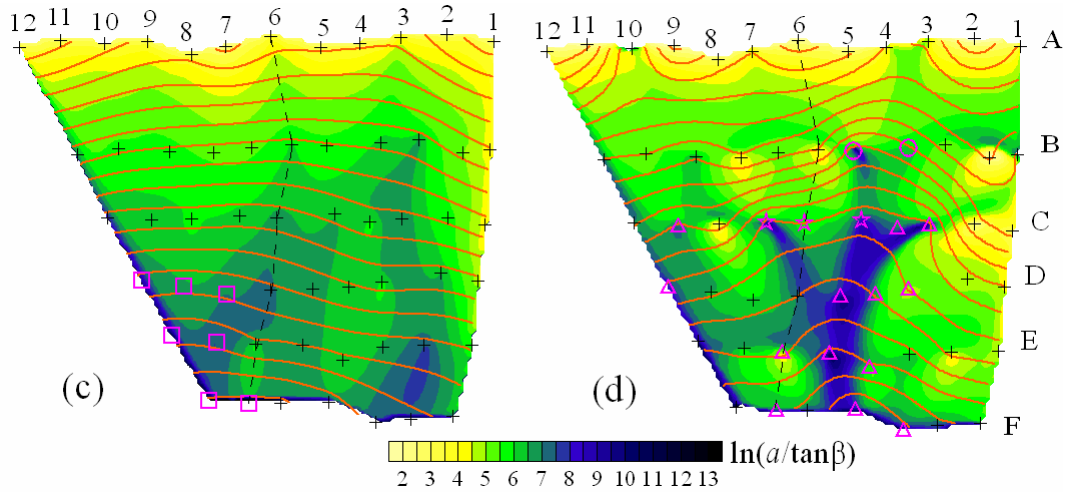
Figure 3.3 (continued)

Figures 3.3c and 3.3d illustrate the topographic index maps for ground and bedrock surfaces, respectively. The index of the ground surface showed a relatively flat distribution except for a slightly higher value in the lower right and lower left sections caused by the gentle concave topography. The index of bedrock surface, on the other hand, clearly showed high values attributable to the bedrock hollow near the center of the study area. Freer et al. (2002) found that the topography of a bedrock surface differed in shape from that of the ground surface, resulting in large disagreements in topographic indices between land and bedrock surfaces. Similar results were observed at the slope in this study.

3.3.2.2 Comparison of the topographic index and water content distribution

Figures 3.4a and 3.4b illustrate the distribution of θ observed at the ground surface and the bedrock surface. Values at each point show an average of θ from the soil surface to 5 cm depth (Fig. 3.4a) and from the bedrock surface to the point 5 cm above the bedrock surface (Fig. 3.4b). Moreover, Figure 3.4c illustrates the distribution of the water storage amount within the whole soil profile at each point, calculated by the integral of the vertical θ distribution observed from the soil surface to the bedrock surface.

At the ground surface, high θ values were mainly distributed in the lower left section (denoted by open squares in Fig. 3.4a). In contrast, high θ values at the bedrock surface were mainly distributed within the hollow (denoted by open circles and triangles in Fig. 3.4b). At C-9 and D-9, where a local small hollow was formed apart from the main hollow, θ also showed high values.

The distribution of water storage amount within the whole soil profile (Fig. 3.4c) depended
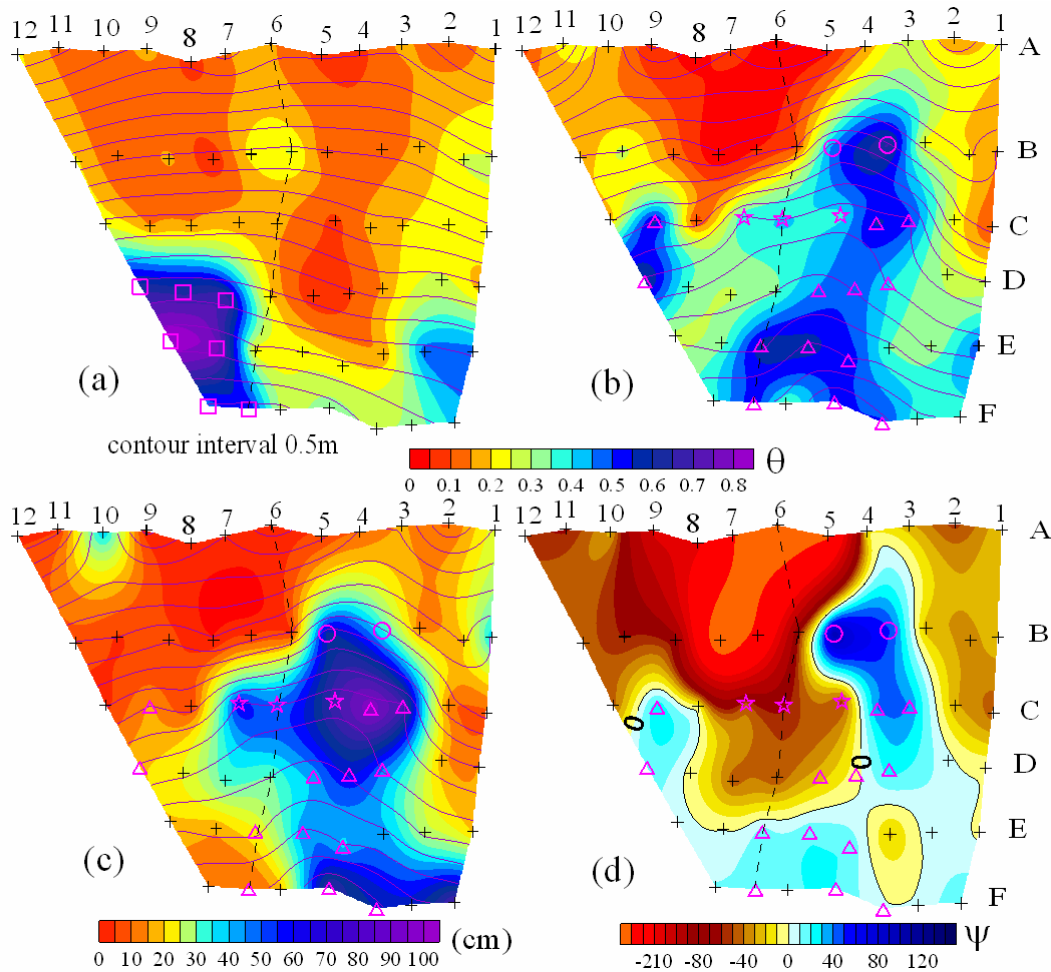
Figure 3.4 (a) Distribution of water content, θ, at the ground surface and ground surface topographic map. (b) Distribution of θ at the bedrock surface and bedrock surface topographic map. (c) Distribution of water storage amount and bedrock surface topographic map. (d) Distribution of pressure head, ψ, at the bedrock surface under a no-rainfall condition. Contour interval of each topographic map is 0.5 m. Open squares show a high θ region at the ground surface. Open triangles show a high θ region at the bedrock surface. Open circles and open stars show a high and low θ region at the bedrock surface not corresponding with the topographic index, respectively.

on both water content (Figs. 3.4a and 3.4b) and soil thickness distribution (Fig. 3.3b). Water storage amount was the highest from C-3 through C-5, which was attributed to the thick soil layer (Figs. 3.2 and 3.3b) and high θ values from the middle to the bottom part of the soil layer (Figs. 3.2 and 3.4b). At the lower left section of the slope, in spite of high θ values at land and/or bedrock surfaces (Figs. 3.4a and 3.4b), the water storage amount showed low values because of the thin soil layer (Fig. 3.3b). Thus,

these results prove the usefulness of the CPMP for measuring the heterogeneous distribution of water storage within a slope.

To evaluate the effect of topography on water distribution, we compared the distribution of the topographic index of the ground surface (Fig. 3.3c) with soil moisture distributions. The distribution of the high θ region at the ground surface (denoted by open squares in Figs. 3.3c and 3.4a) roughly corresponded with high values of the topographic index of the ground surface in the lower left section. However, θ did not show high values in the lower right section where the topographic index of the ground surface was highest (near E-2 and F-2).

To quantitatively discuss the relationship between the soil moisture distribution and effect of topography, coefficients of correlation, r, were calculated and are summarized in Table 3.1. The r value indicated the low correlation between the topographic index and θ at the ground surface (r =0.50; Table 3.1). The distribution of θ at the bedrock surface (Fig. 3.4b) and the water storage amount (Fig. 3.4c) also showed low correlations with the topographic index of the ground surface (Table 3.1). Thus, the topographic index of the ground surface was not a suitable index to describe soil moisture distribution in the studied slope.

When the distribution of topographic index of the bedrock surface (Fig. 3.3d) was compared with soil moisture distributions, θ at the ground surface (Fig. 3.4a) showed low correspondence with the topographic index of the bedrock surface (r =0.28; Table 3.1). On the other hand, the distribution of the high θ region at the bedrock surface roughly corresponded with high values of the topographic index of the bedrock surface within the bedrock surface hollow (denoted by open triangles in Figs. 3.3d and 3.4b). The r value indicated the relatively high correlation between the topographic index and θ at the bedrock surface (r =0.71). In addition, the water storage amount showed relatively high correlation (r =0.63) with the topographic index of the bedrock surface.

These results indicate that the topographic index of the bedrock surface was more effective than that of the ground surface for describing subsurface water convergence within the slope. These results agree with the findings of previous studies, which showed that spatial patterns of the

Table 3.1 Coefficient of correlation, r, values for comparing the topographic index (Figs. 3.3c and 3.3d) and water content/storage (Figs. 3.4a, 3.4b, and 3.4c) distributions.

Topographic index	Water content		Water storage
	Ground surface	Bedrock surface	
Ground surface	0.50	0.57	0.37
Bedrock surface	0.28	0.71	0.63

topographic index of the bedrock surface control lateral stormflow patterns. Freer et al. (2002) documented that point-scale matric pressure head showed high correlation with the topographic index of bedrock surface. Tromp-van Meerveld and McDonnell (2006a and b) also reported that subsurface storm flow including pipe flow showed high correlation with the bedrock contributing area.

However, as indicated by the r value of 0.71 (Table 3.1), the topographic index of the bedrock surface did not perfectly reflect the heterogeneous distribution of soil water content on the bedrock surface. For example, the region around B-4 and 5 was one of the highest regions of θ at the bedrock surface (denoted by open circles in Fig. 3.4b), whereas the topographic index of this region was not so high (denoted by open circles in Fig. 3.3d). Moreover, at C-5 to 7, θ at the bedrock surface was relatively low (denoted by open stars in Fig. 3.4b) while the topographic index was relatively high (denoted by open stars in Fig. 3.3d). Thus, detailed observations of soil thickness and water content by the CPMP revealed some water content distributions that overwhelm the topographic control. Hydrological phenomena causing such discrepancies are discussed in the following sections.

3.3.3 Comparison of the CPMP data with water movement under no-rainfall conditions
3.3.3.1 Soil-bedrock interface

Figure 3.4d illustrates the distribution of pressure head, ψ, at the soil-bedrock interface under a no-rainfall condition (6:00 on 20 September 2008). Rainfall amount was 15 and 22 mm during antecedent seven and fourteen days, respectively. No rainfall was gauged during antecedent three days, and this condition was as dry as that when the results in Figures 3.4a, 3.4b, and 3.4c were obtained by the CPMP observation. Whereas the distribution of θ at the ground surface (Fig. 3.4a) showed low correlation with the distribution of ψ, the distribution of θ at the bedrock surface (Fig. 3.4b) showed good correspondence. The positive-pressure area in Figure 3.4d correlated well with the high θ region in Figure 3.4b ($\theta>0.45$; denoted by open circles and triangles): specifically, the continuous high θ region that expanded from B-4 and 5 (denoted by open circles) to downstream corresponded well with the expansion of the positive-pressure area. Local high θ regions at C-9 and D-9 also corresponded with the local expansion of the positive-pressure area. Since the hydraulic conductivity values of the study hillslope showed sharp increases near saturation (Fig. 2.5b), a high water flow rate was expected in the positive-pressure area. Thus, the continuous high θ region detected by the CPMP measurement at the bedrock surface coincided well with the shape of the high water flow domain under no-rainfall conditions. The results indicate that the CPMP is effective for determining water flow pathways on the soil-bedrock interface.

At C-5 to 7, where relatively low θ values did not correspond with relatively high

topographic index values at the bedrock surface, ψ showed low values (denoted by open stars in Figs. 3.3d, 3.4b, and 3.4d). Moreover, at B-4 and 5, where the largest θ values did not correspond with relatively low topographic index values at the bedrock surface, extremely large positive ψ values were observed (denoted by open circles in Figs. 3.3d, 3.4b, and 3.4d). Hydrological properties at these points are discussed below.

3.3.3.2 Line-C

Figure 3.5a illustrates the spatial distribution of ψ in the cross section of Line-C under the no-rainfall condition (6:00 on 20 September 2008; the same time as in Fig. 3.4d). Plus symbols, stars, and triangles in the figure denote the positions of installed tensiometer porous caps. Figures 3.5b and 3.5c show the distributions of θ and N_c in the cross section of Line-C, respectively (the same data as shown in Fig. 3.2). In Figure 3.5a, the boundary between the surface and subsurface soil layer (N_c=30) is denoted by a brown line. Moreover, arrows denote the magnitude and direction of water flux vectors, q. For the calculation of q, we set triangular elements composed of three tensiometer position nodes. From the hydraulic head (i.e., total head, H) in each node, calculated as the sum of ψ and vertical coordinates, the mean hydraulic gradient in each element was estimated. In addition, K in each element was calculated using the functional K-ψ curves shown in Figure 2.5b. Then q was calculated by multiplying K by the mean hydraulic gradient. Note that no data existed from the top edge (ground surface) to the shallowest tensiometers which were installed at a depth of 30 cm.

In Figure 3.5a, ψ at C-6 to 7 showed negative values above the bedrock surface while ψ showed positive values in the middle part of the profile. The saturated region in the middle part of the profile existed horizontally just above the line of N_c=30, suggesting that the line of N_c=30 corresponds to the hydrological base line. The results of soil hydraulic conductivity tests also indicated that the line of N_c=30 corresponds to the boundary between the high permeability surface soil and the low permeability subsurface (Fig. 2.4). At C-5 the line of N_c=30 was depressed and the high permeability surface soil expanded toward the bottom part of C-3 and C-4 (Fig. 3.5c). In this region, a large flux vector was computed (Fig. 3.5a) which suggested large movements of water from the saturated region in the middle part of the soil profile toward the bottom of the soil profile at C-3 and C-4. As a result, the bedrock surface was fully saturated at C-3 and C4. At C-6 and C-7, on the other hand, the vertical flux was small and the bedrock surface was unsaturated. Thus, Figure 3.5a illustrated that the complex shape of the line of N_c=30, which behaved as the hydrological base line, caused a heterogeneous distribution of the water flow domain.

In Figure 3.5b, the high θ region (i.e., θ>0.45) corresponded well with the distribution of the

positive-pressure area shown in Figure 3.5a, indicating that the CPMP captured the distribution of the saturated region accurately. As shown in Figure 3.1, the high θ region at C-6 existed just above the line of N_c=30. In Figure 3.5b, a similar trend was observed at C-3, 4, and 7. At C-5 the line of N_c=30 showed a depression and the high θ region in the middle part of the profile expanded toward the bedrock surface at C-3 and 4, indicating the presence of large vertical water flux. Thus, from the CPMP measurements, we can infer the complicated hydrological phenomena occurring in Line-C (Fig. 3.5a), which were revealed by the intensive tensiometric measurements and observations of soil hydraulic properties. Therefore, the CPMP can be an effective tool for investigating heterogeneous hydrological properties of natural slopes. As shown in Figure 3.2, in Lines-D through F, the high θ region distributed above the line of N_c=30, indicating that the same hydrological processes as in Line-C also occurred on Lines-D through F.

Figure 3.5 Spatial distributions of (a) pressure head, ψ, (b) water content, θ, and (c) penetration resistance, N_c, in vertical cross-section of Line-C under the no-rainfall condition. Brown lines denote the boundary of the surface and subsurface soil layers (i.e., the line of N_c=30). In (a), arrows denote the magnitude and direction of water flux vectors. Definitions of each symbol are given in the legend of Figure 3.4.

3.3.3.3 Line-V

Figure 3.6a illustrates the spatial distribution of ψ in the cross section of Line-V (Fig. 2.2) under the no-rainfall condition (6:00 on 20 September 2008; the same time as Figs. 3.4d and 3.5a). Symbols and arrows in the figure are as defined in Figure 3.5a, and the brown line denotes N_c=30. Moreover, Figures 3.6b and 3.6c illustrate the vertical distributions of θ and N_c in the cross section of Line-V with the line of N_c=30.

Figure 3.6a shows that groundwater appeared within the subsurface layer between A-4 and B-4 and expanded in the downstream region. In the region between C-4 and F-4, the saturated zone was observed not only in the subsurface soil layer but also in the bottom of the surface soil layer. Large flux vectors toward the downslope direction were computed, indicating that lateral flow dominantly occurred inside of this region. Around the shallowest part of the surface soil layer, evapotranspiration caused upward water fluxes. Contrastingly, within the saturated subsurface layer around B-4, relatively large horizontal or upward fluxes ($10^{-3}<q<10^{-4}$ cm/sec) occurred in spite of the low K_s of this layer. In the upstream region from A-4, ψ showed the quite dry conditions and upward fluxes dominantly occurred due to water consumption by evapotranspiration in the shallow part of the soil profile. The magnitude of the fluxes was extremely low ($10^{-7}<q<10^{-9}$ cm/sec) because K is low for such a low ψ range (Fig. 2.5b). These results indicated that the saturated zone around B-4 was probably not developed by lateral flow from the upstream region but by exfiltration of bedrock groundwater. In the old landslide scarp adjacent to the observation slope, bedrock exfiltration point was present at about the same level as the point B-4 (Figs. 2.2 and 2.3). Figure 3.6a thus illustrates the hydrological phenomena occurring in Line-V whereby the exfiltration of bedrock groundwater at B-4 expands toward the downstream region and creates saturated lateral flow in the subsurface layer and the bottom of the surface soil layer.

In Figure 3.6 b, while θ showed quite dry conditions in the whole soil profile at A-4, the high θ region suddenly appeared in the subsurface soil layer at B-4. Moreover, Figure 3.1 shows that the high θ region at B-4 was not observed at the boundary between the surface and subsurface layers but within the subsurface soil layer. These results strongly indicate the presence of bedrock exfiltration around B-4. In the downstream region from C-4 to F-4, the high θ region was observed within the subsurface soil layer and in the bottom part of the surface soil layer. Therefore, the generation and expansion of the high θ region corresponded well with the distribution of the positive-pressure area (Fig. 3.6a). The results in Figure 3.6 clearly indicate that the CPMP measurements are effective for detecting the locations of bedrock groundwater exfiltration.
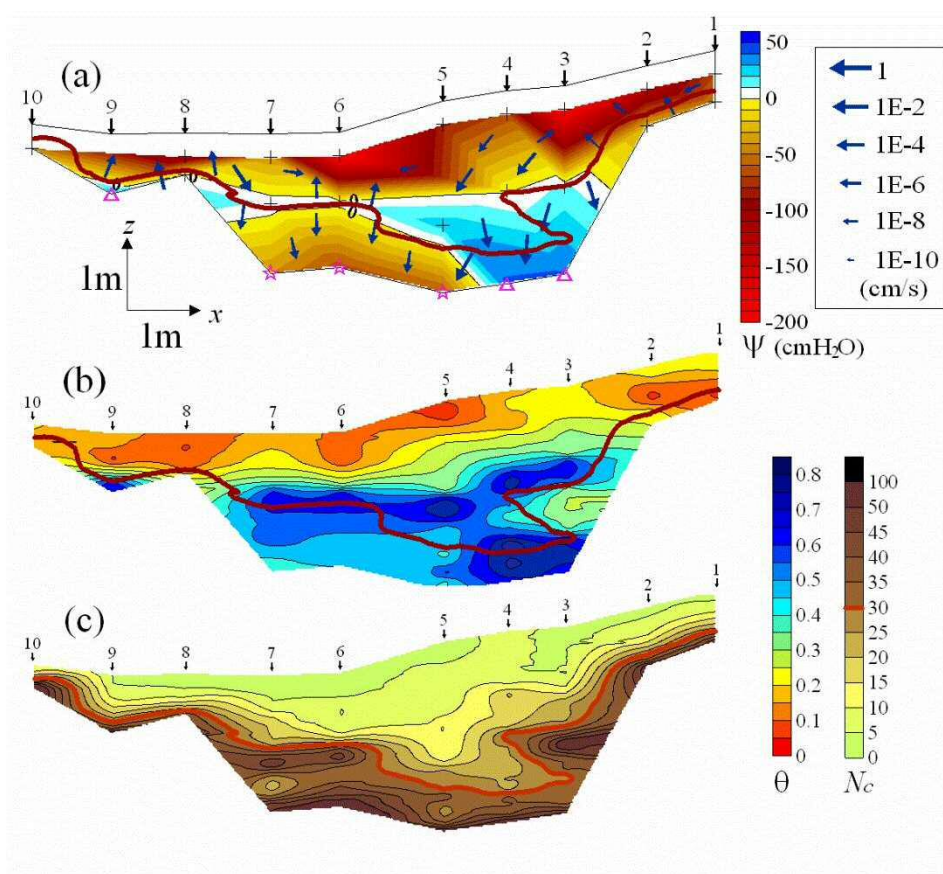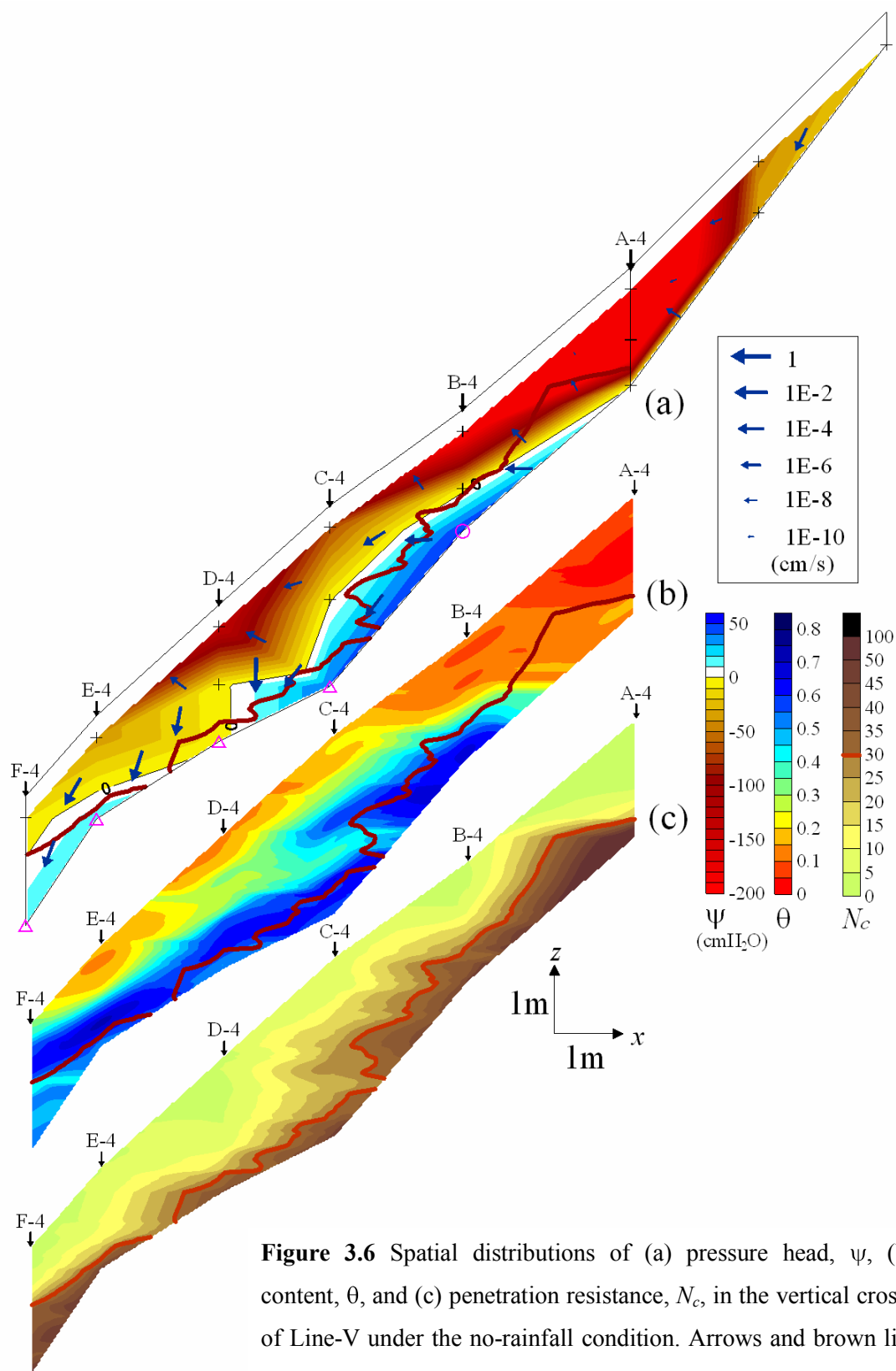
Figure 3.6 Spatial distributions of (a) pressure head, ψ, (b) water content, θ, and (c) penetration resistance, N_c, in the vertical cross-section of Line-V under the no-rainfall condition. Arrows and brown lines have the same meaning as in Figure 3.5. Definitions of each symbol are given in the legend of Figure 3.4.

3.3.4 Comparing the CPMP data with water movement during a rainfall event

3.3.4.1 Preferential flow at the soil-bedrock interface

The previous section compared the movement of subsurface water under the no-rainfall condition with the CPMP data. In this section, we focus on the temporal variation of ψ during a rainfall event and discuss how we can evaluate soil water movement under storm conditions from CPMP data that were observed under a no-rainfall condition.

We studied a storm event that occurred from 26 June to 5 July 2008 (total rainfall was 112 mm; maximum rainfall intensity was 10.2 mm/hr; Fig. 3.7). Figures 3.8a, 3.8b, and 3.8c illustrate the ψ distributions at the bedrock surface for three time points indicated by dotted lines in Figure 3.7: before the rainfall (T1; 20:00 on 28 June), the peak of rainfall (T2; 9:00 on 29 June), and approximately 2 days after the cessation of rainfall (T3; 0:00 on 2 July). The amounts of change in the pressure head, $\Delta\psi$, from time T1 to T2, and from time T2 to T3, are shown in Figures 3.8d and 3.8e, respectively. Temporal variations in ψ at representative points are shown in Figures 3.7a, b, and c.

Before the rainfall (Fig. 3.8a), a saturated area was detected that was quite similar to that in Figure 3.4d in terms of distribution: the saturated area was mainly distributed in the lower section and upper right section. Quite high ψ values were observed at B-4 and 5. At the peak of rainfall, a transient saturated zone expanded into upslope regions (Fig. 3.8b). A continuous high pressure zone (i.e., ψ>100 cm) expanded from B-4 and 5 through F-3, in which a remarkable increase in ψ was observed at D-3, 4, E-4, and F-3 (denoted by solid triangles in Fig. 3.8d). After the cessation of rainfall, ψ at these points showed significant decreases (Figs. 3.8c and 3.8e). Most likely, a preferential water channel (e.g., Uchida et al., 2002; Jones, 2010) was passing through these points, which was activated during the rainfall event, flushing a large quantity of water rapidly to the lower end of the slope. The preferential water channel (i.e., the points D-3, 4, E-4, and F-3) was located within the region where high θ values at the bedrock surface were observed by the CPMP (denoted by open triangles in Fig. 3.4b), indicating that we can predict the location where the preferential water channel potentially exists from the CPMP observations.

Figure 3.7a shows the temporal variations in ψ on a part of Line-E, which cut across the preferential water channel at E-4 (Fig. 3.8b). At E-3 and 7, where the CPMP detected low θ values before the storm event (Fig. 3.4b), ψ kept negative or near-zero values and exhibited no responses to hyetographs (Fig. 3.7a). At E-4 to 6, where the CPMP detected high θ values (denoted by open triangles in Fig. 3.4b), ψ showed positive values. This result confirms that the high θ region observed by the CPMP corresponds to the saturated water channel on the bedrock surface.

Among E-4 to 6, ψ at E-4 increased sharply coinciding with rainfall peaks, while ψ exhibited no response to hyetographs at E-5 and 6 (Fig. 3.7a). In Figure 3.2, the N_c=30 line, which corresponds
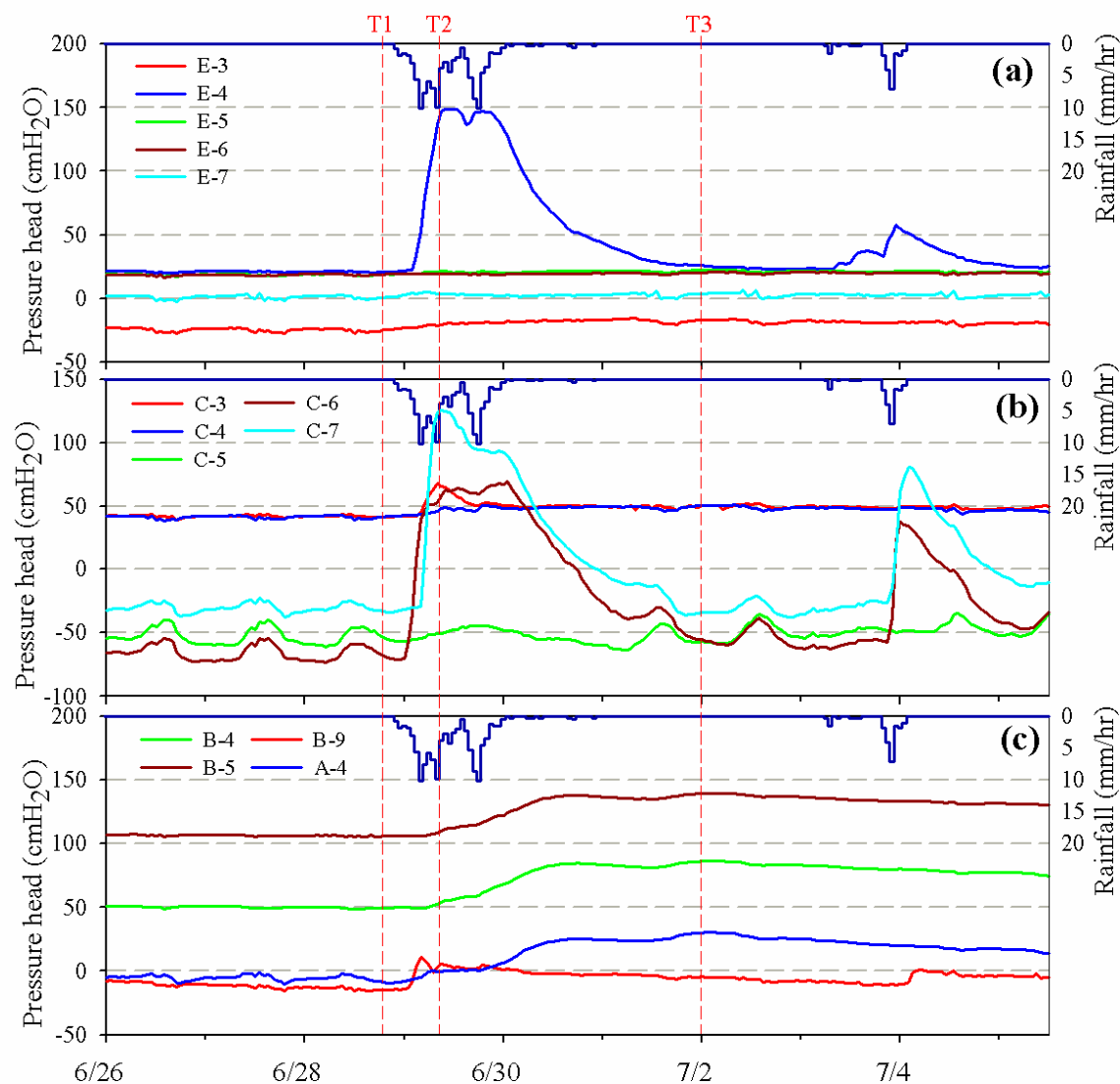
Figure 3.7 Hyetograph and temporal variations of pressure head, ψ, from 26 June to 5 July 2008 for representative points (a) E-3 to 7, (b) C-3 to 7, and (c) A-4, B-4, B-5, and B-9. Broken red lines indicate time points T1, T2, and T3.

to the boundary between the surface and subsurface soil layers, formed a hollow at E-4 where extremely high θ values were observed. Such careful evaluations of the penetration resistance and water content distributions obtained by CPMP measurements may allow for detection of the location of the preferential water channel. It should be noted that at D-4 and F-3, where the preferential water channel was passing through (Figs. 3.8b and 3.8d), similar trends to those at E-4 were observed (Fig. 3.2).

Figure 3.8 Distributions of the pressure head, ψ, at time points denoted in Fig. 3.7: (a) T1; 20:00 on 28 June, (b) T2; 9:00 on 29 June, and (c) T3; 0:00 on 2 July. Distributions of pressure head variation, $\Delta\psi$, between time points: (d) from T1 to T2 and (e) from T2 t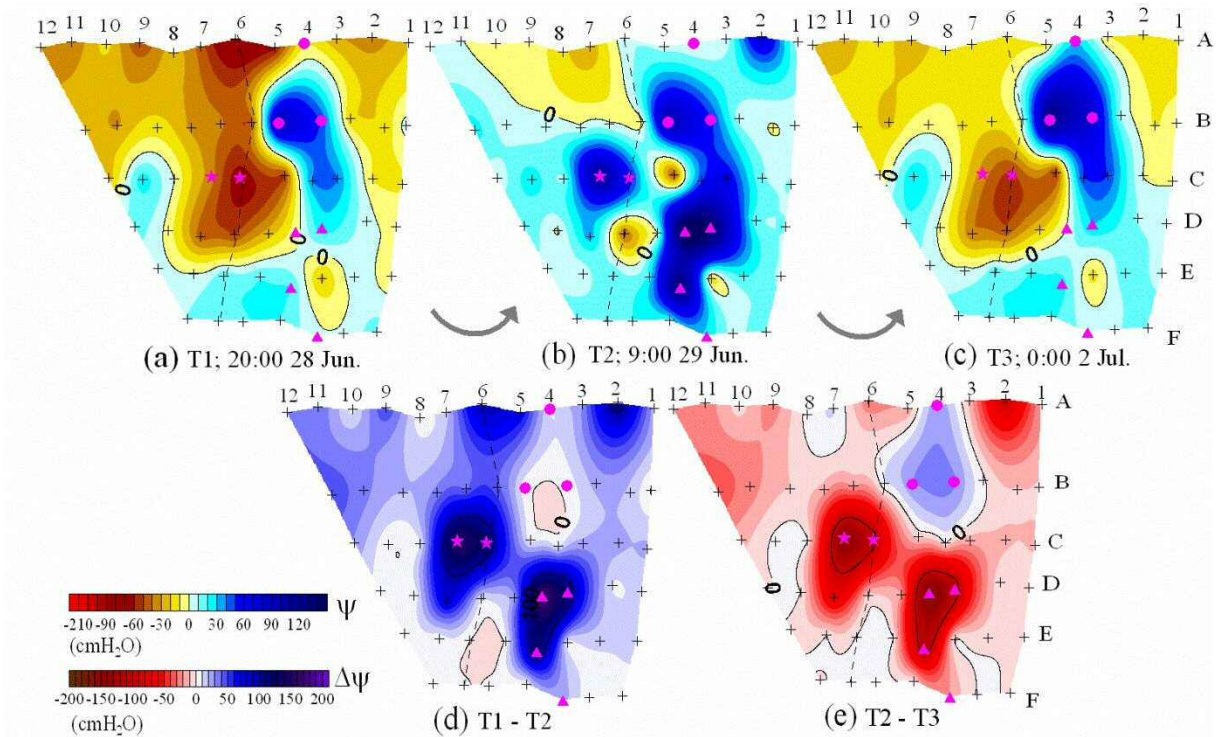o T3. Solid triangles, stars, and circles show the locations of the preferential water channel, variable hydrological base line, and bedrock groundwater exfiltration, respectively.

3.3.4.2 Variation in the hydrological base line on Line-C

At the peak of rainfall, ψ remarkably increased at C-6 and 7 (denoted by solid stars in Figs. 3.8b and 3.8d), where low θ and negative ψ values were observed under the no-rainfall condition (Figs. 3.4b and 3.4d). After the cessation of the rainfall, ψ values at these points quickly decreased to negative values (Figs. 3.8c and 3.8e). It is likely that the remarkable ψ increases at C-6 and 7 were independent from the connection of the preferential water channel observed at D-3, 4, E-4, and F-3 (denoted by filled triangles in Fig. 3.8b), where ψ and θ showed high values under the no-rainfall condition (Figs. 3.4b and 3.4d). The points C-6 and 7 were among the three points (i.e., C-5 to 7) where the presence of a thick low-permeability subsurface soil layer resulted in the low θ and negative ψ at the soil-bedrock interface under the no-rainfall condition (Fig. 3.5). That is, the boundary between the surface and subsurface soil layers (i.e., the line of N_c=30) worked as the hydrological base line, preventing expansion of the positive-pressure area into the subsurface soil layer.

Figure 3.7b shows the temporal variations in ψ at C-3 to 7. At C-3 and 4, both of which were on the preferential water channel, ψ showed positive high values throughout the observation period. Particularly at C-3, ψ showed large responses coinciding with the rainfall peaks. In contrast, at C-5 to 7, ψ remained negative under the no-rainfall condition. Among these points, ψ at C-6 and 7 increased sharply with positive values during the storm event and quickly returned to negative values once rainfall had ceased. It is likely that large vertical hydraulic gradients during storm events activated infiltration pathways within the subsurface layer. That is, at these points, the hydrological base line was deepened during heavy rainfall conditions from the boundary between the surface and subsurface soil layers (i.e., the line of N_c=30) to the soil-bedrock interface (i.e., the line of N_c=100).

The hydrological base line is defined as the surface that intercepts vertical water infiltration into the deeper layer. The shape of the hydrological base line is fundamental information for hydro-geomorphological surveys, such as those used for predicting runoff generation (e.g., Tromp-van Meerveld and McDonnell, 2006a, b) and rain-induced shallow landslides (e.g., Sammori et al., 1995), because it defines the domain where active water movement occurs and pore pressures may affect slope stability. Our results indicate that the position of the hydrological base line varies during a storm event. This phenomenon is considered to be attributable to preferential water infiltration through the low-permeability surface. Olofsson et al. (1994) documented the existence of flow from soil to bedrock through heterogeneously distributed bedrock fractures. In addition, Tsuboyama et al. (1994) found an increase in the macropore flow rate, which they attributed to the extension of macropore networks during wetter conditions. It is a possibility that below the N_c=30 line at C-6 to 7, water infiltration was activated when the preferential flow networks were filled with water due to large hydraulic gradients during storm events.

Under the no-rainfall condition, θ at C-6 to 7 showed medium values (0.35 to 0.5) in the thick subsurface soil layer below the hydrological base line (i.e., the line of N_c=30; Figs. 3.5b and 3.5c), probably because of the limited amount of water infiltration from the saturated zone above the hydrological base line (Fig. 3.5a). Around the hydrological base line, a region with high θ values was detected by the CPMP measurements (Fig. 3.5b). Regions with such distributions of soil water content and penetration resistance may have variable hydrological base lines during storm events.

3.3.4.3 Bedrock groundwater seepage on Line-V

At A-4, B-4, and B-5, where ψ showed almost no increases at the peak of rainfall (denoted by solid circles in Figs. 3.8b and 3.8d), ψ increased substantially 2 days after the cessation of the rainfall (Figs. 3.8c and 3.8e). There was no other point which showed such a delayed ψ increase as A-4, B-4, and B-5. Among these points, B-4 and 5 were points where the existence of bedrock

groundwater seepage was detected under the no-rainfall condition.

Figure 3.7c shows the temporal variations of ψ at A-4, B-4, and 5, in comparison with that at B-9, which is in the same horizontal line as B-4 and 5 but did not show the delayed ψ increases. At B-9, ψ showed rapid peaks with near-zero pressure values coinciding with rainfall peaks and a persistent decrease with negative values during no rain periods. At A-4, B-4, and B-5, on the other hand, ψ showed unique waveforms, with delayed broad peaks after the large rainfall input on 28 to 29 June 2008. Peak values were observed at T3 (0:00 on 2 July) after 68 hours from the peak of rainfall at T2 (9:00 on 29 June), followed by gradual recession limbs. ψ values showed no response to the relatively small rainfall event on 3 July 2008 (total rainfall was 20 mm; maximum rainfall intensity was 7.1 mm/hr). Such delayed responses, only to heavy storm events, and gradual recession limbs are distinctive trends of seepage flow through bedrock fractures (Hirose et al., 1994; Onda et al., 2001; Katsura et al., 2008; Kosugi et al., 2008). These results supported the existence of bedrock groundwater seepage around B-4, as found in Figure 3.6.

Many previous studies have pointed out the contribution of groundwater to runoff generation (e.g., Wilson and Dietrich, 1987; Terajima and Moroto, 1990; Onda et al., 2001) and the occurrence of shallow landslides (e.g., Iverson and Major, 1986; Kato et al., 2000; Montgomery et al., 2002) in headwater catchments. Recently, Kosugi et al. (2006) estimated that approximately 65 to 71% of annual discharge from a 0.086-ha headwater catchment consisted of exfiltration from weathered granitic bedrock. Moreover, Kosugi et al. (2008) and Katsura et al. (2008) documented that the semi-perennial groundwater forms a considerably high water table in soil mantles which cannot be explained by the topographic flow convergence in shallow soils. These studies documented the importance of bedrock groundwater seepage into the soil layer to runoff generation, soil mantle groundwater formations, and landslide occurrence. However, a method of detecting the detailed positions of subsurface seepage points within a slope was not proposed because of the lack of accurate and efficient procedures for investigating the soil water distribution in soil mantles. In this study, we detected sudden and local θ increases beneath the line of N_c=30 at B-4 and 5, which clearly indicated the presence of exfiltration of bedrock groundwater as discussed above. The locations which experienced increases in θ values were not detected using the distribution of classically used topographic indices (Figs. 3.3c and 3.3d). Thus, the CPMP represents an exclusive tool that is currently available for accurately detecting groundwater seepage points.

3.4 Conclusions

We applied a combined penetrometer-moisture probe (CPMP) to investigate hydrological

properties in a foot slope area of a mountainous watershed by simultaneous measurements of the soil water content, θ, and the penetration resistance, N_c, of soil mantles. Using the CPMP, we obtained detailed spatial patterns of θ within the slope as well as soil thickness distributions for calculating the topographic indices. By comparing the topographic indices and θ, we confirmed that the topographic index of the bedrock surface was more effective than that of the ground surface for describing water flow convergence. Moreover, we could effectively detect the heterogeneous water distribution that exists independently of topographic flow convergence. Such anomalous patterns of water content distribution suggested the presence of preferential pathways, a low permeability soil layer, and bedrock groundwater exfiltration.

The CPMP data corresponded well with pressure head values, ψ, observed by tensiometers under the no-rainfall condition. The distribution of a positive-pressure area with concentrated soil water flux corresponded well with the high θ region observed by the CPMP, indicating that we can estimate the complex shape of the hydrological base line and water flow domain from CPMP measurements, without measuring ψ by tensiometers and soil hydraulic conductivity by collecting soil samples. Moreover, the CPMP successfully located a point of bedrock groundwater exfiltration which was otherwise hidden in the studied hillslope because it could detect a sudden increase in θ in the low permeability subsurface layer.

During a heavy rainfall event, preferential water flow occurred within the region where high θ values at the bedrock surface were observed by the CPMP. At points where the CPMP data indicated a thick subsurface layer with medium water content value below a surface layer with large water content, intensive rainwater infiltration shifted the hydrological base line from the boundary between the surface and subsurface layers to the bottom of the subsurface layer. Moreover, around the points where the CPMP data suggested an occurrence of bedrock groundwater exfiltration, ψ exhibited delayed dull peaks responding solely to heavy storm events. Thus, complicated water movement phenomena during a storm event in a foot slope area of a natural hillslope can be inferred from the penetration resistance and water content distributions simultaneously measured by the CPMP under a no-rainfall condition.

This study suggests the large potential of the CPMP for estimating heterogeneous hydrological properties of foot slope areas of natural hillslopes. Future studies should conduct CPMP measurements at various sites and more thoroughly evaluate the distributions of penetration resistance and water content to establish efficient and sound techniques for surveying hillslope hydrological properties.

References

Beven, K.J., and M.J. Kirkby. 1979. A physically based variable contributing area model of basin hydrology. Hydrol. Sci. Bull. 24(1): 43-69.

Freer, J., J.J. McDonnell, K.J. Beven, N.E. Peters, D.A. Burns, R.P. Hooper, B. Aulenbach, and C. Kendall. 2002. The role of bedrock topography on subsurface storm flow, Water Resour. Res. 38(12): 1269, doi: 10.1029/2001WR000872.

Hiramatsu, S., and K. Bitoh. 2001. Study on easy set up method of input data to slope failure predicting model from a handy dynamic cone penetrometer. (In Japanese, with English abstract.) J. Jpn. Soc. Erosion Control Eng. 54: 12–21.

Hirose T., Y. Onda, and Y. Matsukura. 1994. Runoff and solute characteristics in four small catchments with different bedrocks in the Abukuma mountains. Transactions, Jpn. Geomorphol. Uni. 15A: 31-48.

Iverson, R.M., and J.J. Major. 1986. Groundwater seepage vectors and the potential for hillslope failure and debris flow mobilization. Water Resour. Res. 22(11): 1543-1548, doi: 10.1029/WR022i011p01543.

Jones, J.A.A. 2010. Soil piping and catchment response. Hydrol. Process. 24: 1548-1566, doi: 10.1002/hyp.7634.

Kato, Y., Y. Onda, T. Mizuyama, K. Kosugi, A. Yoshikawa, M. Tsujimura, K. Hata, and M. Okamoto. 2000. The difference of runoff peak response time in upstream of Ibi river underlain by different geology. (In Japanese, with English abstract.) J. Jpn. Soc. Erosion Control Eng. 53(4): 38–43.

Katsura, S., K. Kosugi, N. Yamamoto, and T. Mizuyama. 2005. Saturated and unsaturated hydraulic conductivities and water retention characteristics of weathered granitic bedrock. Vadose Zone J. 5: 35–47, doi: 10.2136/vzj2005.0040.

Katsura, S., K. Kosugi, T. Mizutani, S. Okunaka, and T. Mizuyama. 2008. Effects of bedrock groundwater on spatial and temporal variations in soil mantle groundwater in a steep granitic headwater catchment. Water Resour. Res. 44: W09430, doi: 10.1029/2007WR006610.

Kosugi, K., S. Katsura, M. Katsuyama, and T. Mizuyama. 2006. Water flow processes in weathered granitic bedrock and their effects on runoff generation in a small headwater catchment. Water Resour. Res. 42: W02414, doi: 10.1029/2005WR004275.

Kosugi, K., S. Katsura, T. Mizuyama, S. Okunaka, and T. Mizutani. 2008. Anomalous behavior of soil mantle groundwater demonstrates the major effects of bedrock groundwater on surface hydrological processes. Water Resour. Res. 44: W01407, doi: 10.1029/2006WR005859.

Kosugi, K., Y. Yamakawa, N. Masaoka, and T. Mizuyama. 2009. A combined penetrometer-moisture probe for surveying soil properties of natural hillslopes. Vadose Zone J. 8: 52-63, doi:

10.2136/vzj2008.0033.

Lin, C.P., S.H. Tang, and C.C. Chung. 2006. Development of TDR penetrometer through theoretical and laboratory investigations: 1. Measurement of soil dielectric permittivity. Geotech. Testing J. 29:306-321.

McGlynn B.L., J.J. McDonnell, J.B. Shanley, and C. Kendall. 1999. Riparian zone flowpath dynamics during snowmelt in a small headwater catchment. J. Hydrol. 222:75-92.

Montgomery, D.R., W.E. Dietrich, and J.T. Heffner. 2002. Piezometric response in shallow bedrock at CB1: Implications for runoff generation and landsliding. Water Resour. Res. 38(12): 1274, doi: 10.1029/2002WR001429.

Ohsaka, O., T. Tamura, J. Kubota, and Y. Tsukamoto. 1992. Process study of the soil stratification on weathered granite slopes. (In Japanese, with English abstract.) J. Jpn. Soc. Erosion Cont. Eng. 45(3): 3-12.

Okimura, T., and S. Tanaka. 1980. Researches on soil horizon of weathered granite mountain slope and failed surface depth in a test field. (In Japanese, with English abstract.) J. Jpn. Soc. Erosion Cont. Eng. 33(1):7–16.

Okunishi, K., and T. Iida. 1978. Study on the landslides around Obara village, Aichi prefecture (I)-Interrelationship between slope morphology, subsurface structure and landslides-. (In Japanese, with English abstract.) Bull. Disast. Prevent. Res. Instit. 21B:297-311.

Olofsson, B. 1994. Flow of groundwater from soil to crystalline rock. Hydrogeol. J. 2(3):71-83, doi: 10.1007/s100400050052.

Onda, Y., Y. Komatsu, M. Tsujimura, and J. Fujihara. 2001. The role of subsurface runoff through bedrock on storm flow generation. Hydrol. Process. 15:1693-1706, doi: 10.1002/hyp.234.

Quinn, P., K. Beven, and A. Culf. 1995. The introduction of macroscale hydrological complexity into land surface-atmosphere transfer models and the effect on planetary boundary layer development. J. Hydrol. 166:421-444.

Sammori, T., Y. Ohkura, H. Ochiai, and H. Kitahara. 1995. Effects of Soil Depth on Rain-induced Landslide. (In Japanese, with English abstract.) J. Jpn. Soc. Erosion Cont. Eng. 48(1):12-23.

Shanley, J.B., K.N. Hjerdt, J.J. McDonnell, and C. Kendall. 2003. Shallow water table fluctuations in relation to soil penetration resistance. Ground Water 41(7):964-972.

Starr, J.L., and I.C. Paltineanu. 1998. Real-time soil water dynamics over large areas using multisensor capacitance probes and monitoring system. Soil Tillage Res. 47:43–49.

Sun, Y., P.S. Lammers, and D. Ma. 2004. Evaluation of a combined penetrometer for simultaneous measurement of penetration resistance and soil water content. J. Plant Nutr. Soil Sci. 167:745-751, doi: 10.1002/jpln.200421365.

Terajima, T., and K. Moroto. 1990. Stream flow generation in a small watershed in granitic mountain. (In Japanese, with English abstract.) Transactions, Jpn. Geomorphol. Uni. 11:75-96.

Topp, G.C., J.L. Davis, and A.P. Annan. 1980. Electromagnetic determination of soil water content: Measurements in coaxial transmission lines. Water Resour. Res. 16:574–582.

Topp, G.C., D.R. Lapen, M.J. Edwards, and G.D. Young. 2003. Laboratory calibration, in-field validation and use of a soil penetrometer measuring cone resistance and water content. Vadose Zone J. 2:633-641.

Tromp-van Meerveld, H.J., and J.J. McDonnell. 2006. Threshold relations in subsurface stormflow: 1. A 147-storm analysis of the Panola hillslope. Water Resour. Res. 42:W02410, doi: 10.1029/2004WR003778.

Tromp-van Meerveld, H.J., and J.J. McDonnell. 2006. Threshold relations in subsurface stormflow: 2. The fill and spill hypothesis. Water Resour. Res. 42:W02411, doi: 10.1029/2004WR003800.

Tsuboyama, Y., R. C. Sidle, S. Noguchi, and I. Hosoda. 1994. Flow and solute transport through the soil matrix and macropores of a hillslope segment. Water Resour. Res. 30:879-890.

Uchida, T., K. Kosugi, and T. Mizuyama. 2002. Effects of pipeflow and bedrock groundwater runoff generation at a steep headwater catchment, Ashiu, central Japan. Water Resour. Res. 38(7) doi: 10.1029/2001WR000773.

Vaz, C.M.P., and J.W. Hopmans. 2001. Simultaneous measurements of soil penetration resistance and water content with a combined penetrometer-TDR moisture probe. Soil Sci. Soc. Am. J. 65:4-12.

Wakatsuki, T., Y. Sasaki, Y. Tanaka, and Y. Matsukura. 2007. Predictive equation of unit weights, shear-strength parameters and permeability of grus using by simplified dynamic cone penetrometer hardness and grain size. (In Japanese, with English abstract.) J. Jpn. Soc. Erosion Cont. Eng. 59(6):38-46.

Wilson, C.J., and W.E. Dietrich. 1987. The contribution of bedrock groundwater flow to storm runoff and high pore pressure development in hollows. p. 49-59. *In* R.L. Beschta et al. (ed.) IAHS Publ. 165. Erosion and Sedimentation in the Pacific Rim, 3-7 August 1987. Oregon State Univ. Corvallis, Oregon, USA.

Yamakawa, Y., K. Kosugi, N. Masaoka, Y. Tada, and T. Mizuyama. 2010. Use of combined penetrometer-moisture probe together with geophysical methods to survey hydrological properties of a natural slope. Vadose Zone J. 9:768-779, doi: 10.2136/vzj2010.0012.

CHAPTER 4

Intensive three-dimensional water flow analysis using soil pore water pressure measurements and model calculation

4.1 Introduction

High-resolution and three-dimensional direct observations of water flow using tensiometers are the most reliable method for analyzing heterogeneous hydrological phenomena. In previous studies on slope hydrology, tensiometers were often installed in vertical cross-sections in order to observe the vertical infiltration and lateral flow processes along a hillslope (e.g., Terajima and Moroto, 1990). However, lateral flow in the horizontal direction (perpendicular to the soil profile) was ignored because wide areas were rarely covered. In recent studies, thanks to the development of measuring technology, a lot of tensiometers have been installed at the bedrock surface to cover relatively broad areas in order to detect the water flow domain above the bedrock surface (Freer et al., 2002; Montgomery et al., 2002; Nishiguchi et al., 2005). However, in these studies, tensiometers were installed at scattered positions to cover broader areas. Thus, they lacked sufficient spatial resolution to capture highly heterogeneous water movements. Intensive observations using densely nested tensiometers intended to analyze heterogeneous hydrological phenomena have not been conducted in previous studies.

In recent years, numerical simulations of hillslope hydrological processes using a three-dimensional, physically-based model have been proposed to predict runoff generation and occurrence of shallow landslides (Wilkinson et al., 2002; Jones et al., 2008). If the heterogeneous hydrological phenomena could be incorporated into these models, the accuracy of runoff/landslide prediction would improve to a great extent. Hopp and McDonnell (2009) simulated the effect of subsurface saturation connectivity on the discharge at a natural hillslope with a heterogeneous soil thickness and bedrock topography. However, the heterogeneous hydrological phenomena attributed to the distribution of hydraulic properties (e.g., saturated hydraulic conductivity) were not taken into account. In most of the studies modeling natural hillslopes, a relatively homogeneous distribution of hydraulic properties was assigned because of the difficulties in surveying hydraulic properties in high resolution. On the other hand, heterogeneous hydrological phenomena such as preferential pipe flow have been analyzed using the modeling approach (e.g., Barcelo and Nieber, 1981 and 1982; Jones and Connelly, 2002). Tsutsumi et al. (2005) developed a model describing three-dimensional lateral preferential flow with soil pipes and compared this to a bench-scale experiment. Although these studies represented the concepts of the phenomena, the actual water movement occurring within

natural hillslopes was not reproduced. Because the spatial distribution and movement of soil water reflects the heterogeneity of the hydraulic properties, it is possible to use high-resolution water movement data to construct a model that reproduce the heterogeneous hydrological phenomena that actually occur in natural slopes. Moreover, the distributions of hydraulic properties can be estimated more precisely.

The objectives of this chapter are (1) to clarify the three-dimensional hydrological process, including heterogeneous phenomena, in detail and (2) to reproduce the hydrological process by estimating the spatial distribution of the hydraulic properties in a model calculation. We carefully observed the pore water pressure using densely nested tensiometers and then attempted to model the studied hillslope.

4.2 Materials and Methods

4.2.1 Tensiometer observation

At the study site (described in Chapter 2), we continuously monitored the soil pore water pressure (soil matric pressure head, ψ) using densely nested tensiometers. Figure 4.1a shows a ground surface topographic map and the numbered locations of all of the observation points. Figures 4.1b and 4.1c show the topographic maps and soil thickness distributions of the middle layer and bedrock surface, respectively. The bedrock surface was determined by a penetration resistance value, N_c, exceeding 100, based on recent studies conducted in granitic watersheds (Katsura et al., 2005; Kosugi et al., 2006). A description of the penetration test using the CPMP was given in Chapter 3. The middle layer was the midpoint between the bedrock surface and shallow tensiometers (described below). At points where the shallow tensiometers were not installed, the middle layer was the midpoint between the bedrock surface and ground surface.

From 15 June to 14 November 2011, we monitored ψ using 111 tensiometers. Among these, 57 tensiometers were installed at the soil-bedrock interface (denoted by dots in Fig. 4.1c). They were installed at all of the CPMP observation points (described in Chapter 3) along six horizontal lines, referred to as Lines-A to F from the top of the slope down (Fig. 4.1a). We also monitored ψ using an additional 54 tensiometers. Thirty five of these were installed at a depth of 30 cm (dots in Fig. 4.1b), which are referred to as shallow tensiometers hereafter. The other 19 were installed in the middle layer (squares in Fig. 4.1b). The middle tensiometers were installed between the shallow and deep tensiometers at depths of 80 to 160 cm.

The tensiometers were attached to pressure transducers (PA-850-102V-NGF; Copal Electronics, Shinjuku, Tokyo, Japan). ψ values were recorded at 5-min intervals throughout the observation period using a data logger (CR1000; Campbell Scientific, Logan, UT, USA).
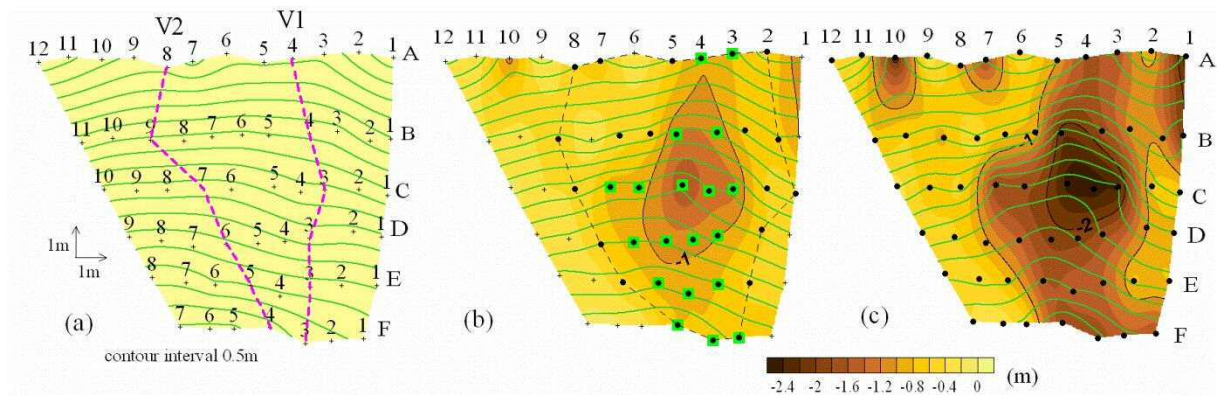
Fig. 4.1 (a) Ground surface topographic map and locations of all observation points. The broken line indicates the location of the vertical cross-section regarded as Lines-V1 and V2. (b) Middle layer topographic map and soil thickness distribution from ground surface to the middle layer. Dots and squares denote the tensiometers installed in shallow and middle layers, respectively. Tensiometers were not installed in shallow and middle layers outside the domain bounded by the broken line. (c) Bedrock surface topographic map and soil thickness distribution from ground surface to bedrock surface. Dots denote tensiometers installed at the soil–bedrock interface. The contour interval of each topographic map is 0.5 m.

4.2.2 Rainfall and discharge observations

From 15 June to 14 November 2011, we observed discharge from a bedrock groundwater spring located inside an old landslide scarp adjacent to the study site (left panel in Fig. 2.2). The springwater was channeled into a 0.5-L tipping bucket, which was leveled and fixed to a solid structure. The accumulated bucket tips were recorded at 5-min intervals throughout the observation period using the data logger (CR1000). From 15 June to 6 September 2011, we observed subsurface trench flow from an artificial trench excavated approximately two meters downslope from Line-F (right panel in Fig. 2.2). We monitored the trench flow volume using a 30° V-notch weir with a water-level recorder (DL/N70; Sensor Technik Sirnach AG, Sirnach, Switzerland) at 5-min intervals throughout the observation period. A rain gauge was placed in an open space on the ridge near the studied hillslope (left panel in Fig. 2.2).

4.2.3 Model description

We used the finite element model KEnIC-3D (e.g., Fujimoto et al., 2011) for our calculations. To predict the matrix flow within the soil, a three-dimensional Richards' equation was solved numerically using a finite element method (Istoc, 1989). The unsaturated hydraulic conductivity, $K(\psi)$, was represented using the lognormal distribution (LN) model expressed by Eqs. [2-1], [2-2], and [2-3] (Kosugi, 1996).
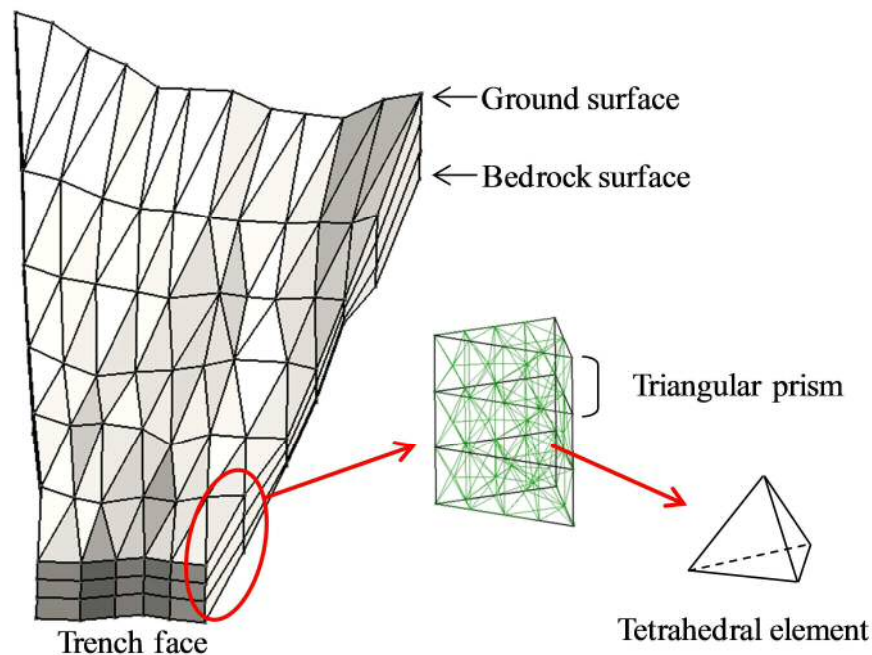
Fig. 4.2 Model domain divided by finite element mesh and method for establishing tetrahedral finite elements.

Figure 4.2 shows the model domain divided by a finite element mesh, along with the methods used to establish the tetrahedral finite elements. First, 96 triangular grids were formed by lines connecting 57 observation points and six trench face points at the ground surface. From the vertex of each triangle, a perpendicular line was drawn to the bedrock surface, generating 96 triangular prisms. Each prism was sliced into two to four layers, which resulted in the generation of 303 small triangular prisms. The hydraulic properties for each of these 303 prisms can be set arbitrarily. Second, each prism was divided into tetrahedrons using Gmsh (a three-dimensional finite element mesh generator; Geuzaine and Remacle, 2009). As a result, a finite element grid with 2119 nodes and 9974 elements was used in the calculations. The boundary conditions were set up as follows: the bedrock surface and side faces of the model domain were assumed to be impermeable, and zero-flux conditions were assigned to these boundaries. Precipitation was imposed on the ground surface of the domain. The seepage face condition was assigned to nodes at the ground surface and trench face. Perennial groundwater seepage from the bedrock was also incorporated into the domain and represented as a source term (described below).

4.3 Results and Discussion

4.3.1 Observed hydrological process of studied hillslope
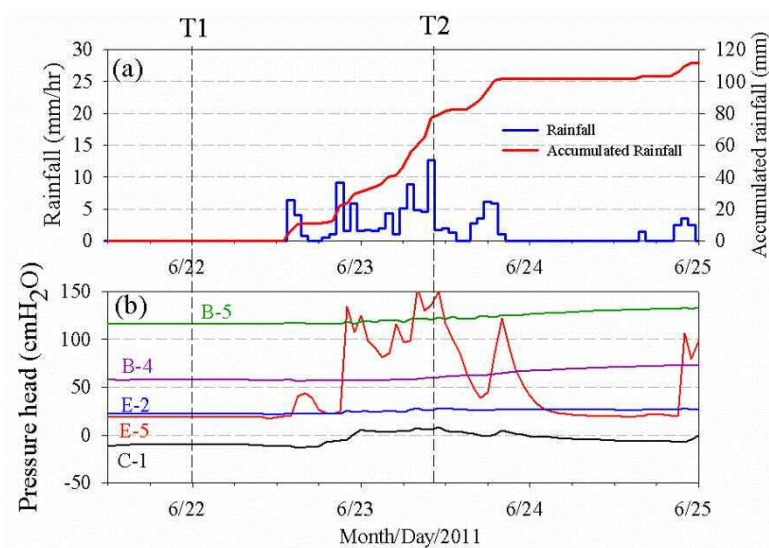
4.3.1.1 No-rainfall condition

Fig. 4.3 (a) Hyetograph and accumulated rainfall from 21 to 25 June 2011. (b) Temporal variation of pressure head, ψ, at B-4 and 5, C-1, and E-2 and 5 from 21 to 25 June 2011.

First, we focus on the distributions of ψ before the beginning of rainfall at time point T1, which is indicated by a broken line in Figure 4.3. Figures 4.4a and 4.4b illustrate the distribution of the pressure head, ψ, in the middle layer and at the soil-bedrock interface, respectively, before the beginning of rainfall (T1; 0:00 on 22 June 2011). The rainfall amounts were 11 and 49 mm during the antecedent seven and fourteen days, respectively. At the points where tensiometers were not installed in the middle layer, the ψ values for the middle layer were calculated by interpolating the ψ values at the shallow layer and soil-bedrock interface (denoted by just dots in Fig. 4.1b) or by subtracting the difference in elevation head (vertical coordinates) from the ψ value at the soil-bedrock interface (outside the domain bounded by a broken line in Figs. 4.1b and 4.4a). The arrows in the figures denote the values and directions of the water flux vectors, q. For the calculation of q, we set triangular elements composed of three tensiometer position nodes. From the hydraulic head (i.e., total head, H) in each node, calculated as the sum of ψ and the vertical coordinates, the mean hydraulic gradient in each element was estimated. In addition, the hydraulic conductivity, K, in each element was calculated using the functional K-ψ curves shown in Figure 2.5b. Then q was calculated by multiplying K by the mean hydraulic gradient.

In the middle layer (Fig. 4.4a), the saturated area ($\psi \geq 0$) started from B-5 and spread toward the lower region, where the flux vectors mostly pointed in the downslope direction and showed large values. At the soil-bedrock interface (Fig. 4.4b), the saturated area began at B-4, 5, and C-9 (denoted by circles) and spread in the downslope direction. At B-4 and 5, especially high ψ values were observed, despite the no-rainfall condition. In the saturated area, the flux vectors pointed in the downslope direction and showed a large volume. However, ψ showed an unsaturated condition in the

middle section of the slope (C-6, 7, D-4 to 8, and E-3), where the bedrock surface was hollowed, which did not correspond to the bedrock topography (Fig. 4.1c). In the unsaturated area, the flux vectors showed very small values because of the steep decline of K in the negative ψ range (Fig. 2.5b).

Figure 4.4c illustrates the distribution of the vertical flux values, calculated by multiplying K by the mean hydraulic gradient between the middle layer and soil-bedrock interface at each point. Note that we cut off the data at points where tensiometers were installed only at the soil-bedrock interface (outside the domain bounded by a broken line in Fig. 4.1b), because at least two data points are required to estimate the hydraulic gradient. Negative values indicate the infiltration flux and positive values indicate the exfiltration flux. A local exfiltration flux existed at B-4 and 5, where especially high ψ values were observed at the soil-bedrock interface (circles in Fig. 4.4c), although the infiltration flux was dominant throughout the slope.

As shown in Figures 4.4a and 4.4b, the ψ distributions varied vertically within the soil profile. Figure 4.5a illustrates the ψ distributions in the vertical cross-sections of Lines-A to F before the rainfall event (T1; Fig. 4.3a). The top edge of each cross-section indicates the ground surface, and the bottom edge indicates the soil-bedrock interface. The dots and circles in the figures denote the positions of the installed tensiometer porous caps. The broken lines in the figure correspond to the location of the middle layer (e.g., Fig. 4.4a). Note that no data existed from the top edge (ground surface) to the shallowest tensiometers, which were installed at a depth of 30 cm.

The whole area in Line-A was unsaturated and showed a small infiltration flux. In Line-B, a saturated area with exfiltration flux was detected within a bedrock hollow at B-4 and 5 (denoted by circles), suggesting that bedrock groundwater was seeping despite the no-rainfall condition. In Line-C, the ψ at C-6 and 7 showed negative values above the bedrock surface, whereas positive values were seen in the middle layer, indicating the existence of perched water in the middle layer. In Lines-D and E, similar trends were also detected at D-4 to 8 and E-3. In Line-F, the soil was almost saturated up to the ground surface. Except for B-4 and 5, the flux vectors pointed downward over the entire area in Lines-A to F.

Figures 4.6a and 4.6c illustrate the distributions of ψ in the vertical cross-sections of Lines-V1 and V2, respectively, before the rainfall event (T1; Fig. 4.3a). In Line-V1, groundwater appeared between A-4 and B-4 and expanded in the downstream region. Within the saturated area around B-4, relatively large horizontal or upward fluxes ($10^{-3} < q < 10^{-4}$ cm/sec) occurred, while ψ showed a dry condition and small infiltration flux at A-4. These results indicated that the saturated zone around B-4 was probably not developed by lateral flow from the upstream region but by exfiltration of the bedrock groundwater.

On the other hand, a perched saturated area was observed in the region between D-3 and F-3, where flux vectors indicated the occurrence of a large lateral flow. In the unsaturated area beneath the perched water, the flux vectors indicated the occurrence of a very small vertical infiltration, showing
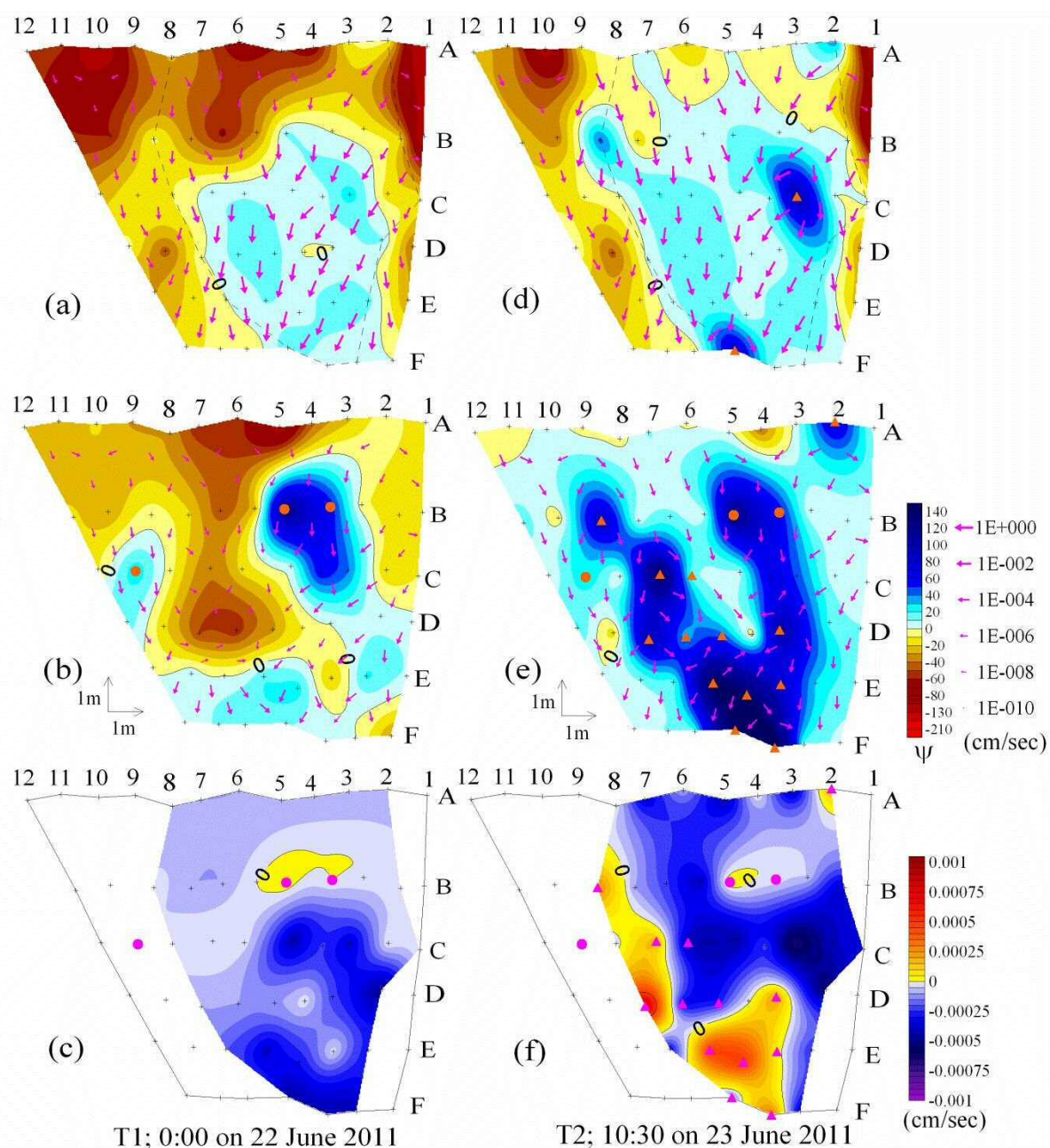
Fig. 4.4 Distributions of pressure head, ψ, (a) in the middle layer and (b) at the bedrock surface, and (c) distribution of the vertical flux value at time point T1 denoted in Fig. 4.3a. Distributions of ψ (d) in the middle layer and (e) at the bedrock surface, and (f) distribution of the vertical flux value at time point T2 denoted in Fig. 4.3a. Circles denote the generation point of the saturated area at the soil–bedrock interface under the no-rainfall condition. Triangles denote points showing a large increase in ψ at the peak of rainfall. Arrows denote the magnitude and direction of water flux vectors. Broken line in (a) and (d) has the same meaning as in Fig. 4.1b.
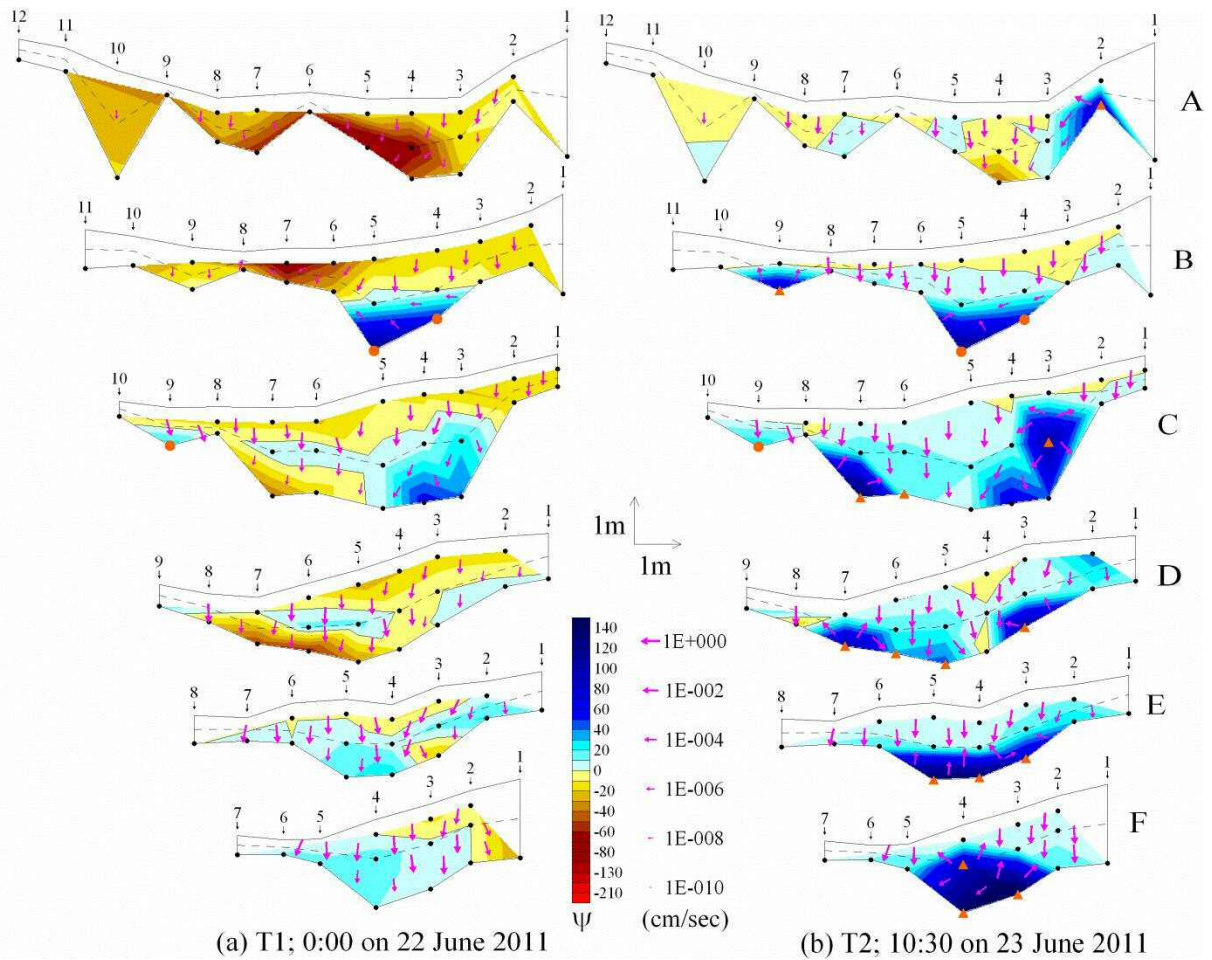
Fig. 4.5 Distributions of pressure head, ψ, in the vertical cross-sections of Lines-A to F at time points denoted in Fig. 4.3a: (a) T1 and (b) T2. Broken lines correspond to the location of the middle layer (e.g., Fig. 4.4a). Symbols and arrows have the same meaning as in Fig. 4.4.

that the water mostly flowed above the middle layer, with very little infiltration toward the bedrock surface under the no-rainfall condition. In line-V2 (Fig. 4.6c), a perched saturated area was also observed in the region between C-7 and E-5. The perched water that started from C-7 was considered to be derived from groundwater seepage at B-4 and 5, which spread toward the downslope region in the middle layer (Fig. 4.4a). At E-5 and F-4, almost the entire soil layer showed a saturated condition from the bedrock surface to the ground surface, and a relatively large infiltration flux occurred.

The existence of perched water reflected the highly heterogeneous distribution of hydraulic properties in this area. The soil under the perched saturated area was considered to have low permeability, which prevented vertical infiltration. At the same time, the water retaining capacity was low, which allowed the water to drain effectively and maintained the unsaturated condition. As described in Chapters 2 and 3, a relatively thick weathered bedrock layer (i.e., subsurface soil layer)
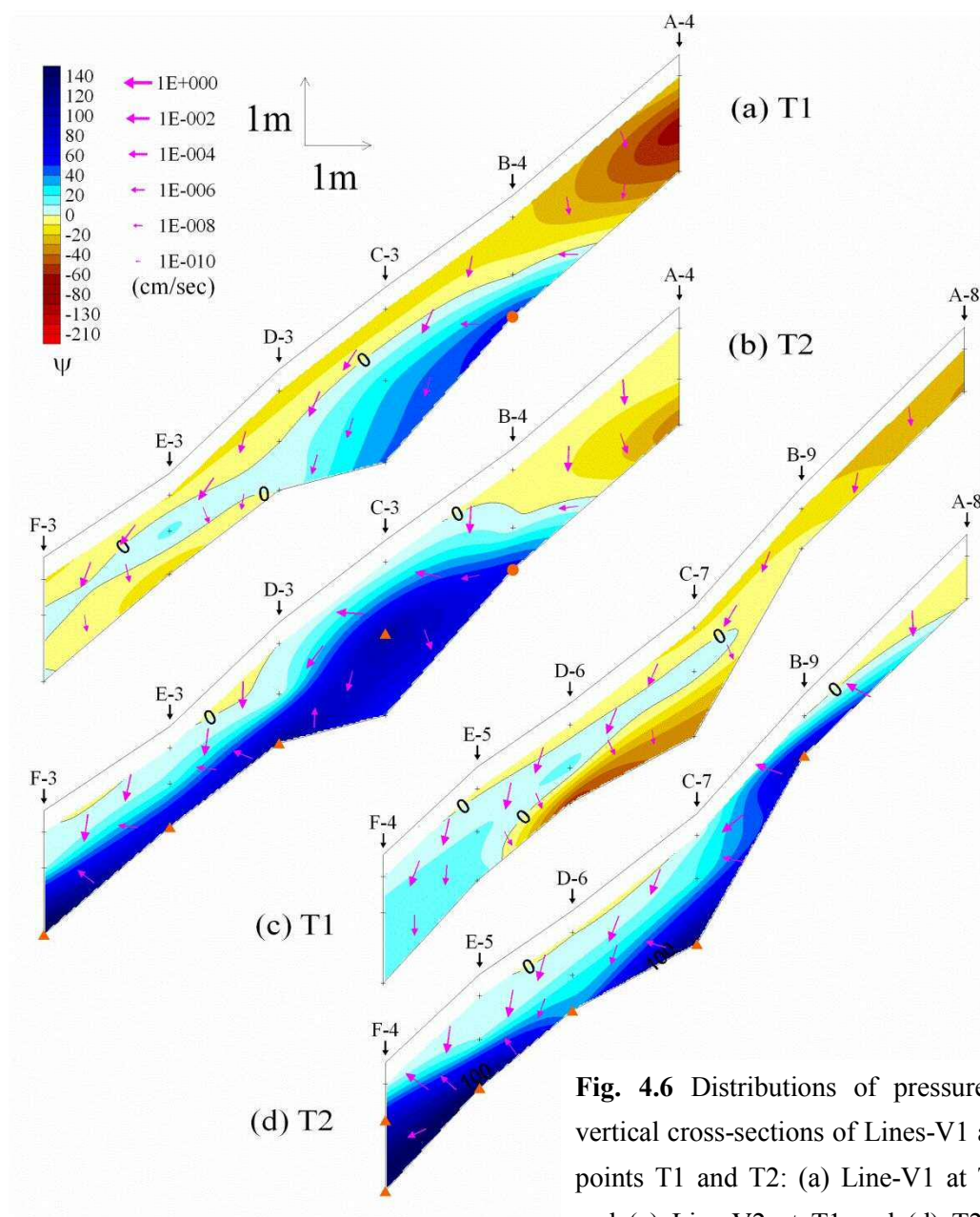
Fig. 4.6 Distributions of pressure head, ψ, in vertical cross-sections of Lines-V1 and V2 at time points T1 and T2: (a) Line-V1 at T1 and (b) T2 and (c) Line-V2 at T1 and (d) T2. Symbols and arrows have the same meaning as in Fig. 4.4.

exists below the surface soil layer at the studied hillslope. This weathered bedrock showed a lower hydraulic conductivity than that of the surface soil (Fig. 2.4). However, previous studies have suggested that fractures in the near-surface bedrock are distributed heterogeneously, which result in a large spatial variability of hydraulic conductivity (e.g., Montgomery et al., 1997 and 2002). The perched saturated area under no-rainfall conditions indicated that the weathered bedrock layer had low permeability, which prevented the vertical infiltration of water in the upper part of the layer, but also had a low water retaining capacity because of the heterogeneously distributed fractures inside the layer.

4.3.1.2 Peak for rainfall event

Next, we focused on the variation in ψ at the peak of the heavy rainfall event that occurred from 22 to 24 June 2011 (total rainfall was 102 mm; maximum rainfall was 13 mm/hr; Fig. 4.3a). Figure 4.3a shows the hyetograph and accumulated rainfall for the event. Figure 4.3b shows the temporal variations in ψ at representative points: B-4, B-5, C-1, E-2, and E-5. Figures 4.4d, 4.4e, and 4.4f illustrate the distributions of ψ in the middle layer, ψ at the soil-bedrock interface, and the vertical flux value, respectively, at the peak of the rainfall event (T2; 10:30 on 23 June 2011).

In the middle layer, a transient saturated zone expanded into upslope regions. In particular, ψ increased to more than 50 cmH$_2$O at C-3M and F-4M (denoted by triangles in Fig. 4.4d). The flux vectors indicated that the water mostly flow downward showing large values. At the soil-bedrock interface (Fig. 4.4e), a transient saturated zone covered almost the entire slope by an increase in ψ in the middle and upper regions of the slope (e.g., C-1 in Fig. 4.3b). It is noted that large increases in ψ were observed at 13 points (denoted by triangles in Fig. 4.4e). At these points, the ψ values increased to at least 50 cmH$_2$O. As a result, continuous high pressure zones (i.e., $\psi > 50$ cmH$_2$O) expanded from B-4 through F-3 in the right section and from B-9 through F-4 in the left section of the slope. Both of these high pressure zones converged at the lower region, showing a substantial ψ increase up to 100 cmH$_2$O. As shown in Figure 4.3b, the ψ value at E-5 spiked sharply to more than 100 cmH$_2$O, coinciding with the rainfall peaks, whereas ψ exhibited a slight increase at E-2, which was located in the same line as E-5. Although the flux vectors pointed upslope around the converging region (i.e., E-3 and 4), they mostly showed large values and pointed downward along the high pressure zones, indicating that a large quantity of water flowed toward the lower end of the slope through the zones. The exfiltration flux existed over the entire area of the left high pressure zone (i.e., B-9, C-7, and D-7 in Fig. 4.4f), lower part of the right high pressure zone (i.e., D-3), and in the converging region (i.e., E-3 to 5 and F-3). Such an exfiltration flux along the high pressure zones indicates that excess pore water pressure was generated along the zones. These results indicated that preferential water channels (e.g., Uchida et al., 2001; Jones, 2010) were passing through these points, which were activated during the rainfall event, flushing a large quantity of water rapidly to the lower end of the slope. In addition, a pipe could have produced such excess pressure in the surrounding soil when the accumulated water exceeded the transmission capacity (Roger and Selby, 1980; Pierson, 1983; Uchida et al., 2004).

Figure 4.5b illustrates the distribution of ψ in the vertical cross-sections of Lines-A to F at the peak of the rainfall event (T2; Fig. 4.3a). The transient saturated zone mostly covered the entire area up to the ground surface in Lines-B to F. A large infiltration flux was dominant in the shallow layer. However, at the points where perched water was detected under the no-rainfall condition (i.e., C-6, 7, D-4 to 8, and E-3; Fig. 4.4a), the ψ values showed large increases with a large exfiltration flux above the bedrock surface, with the exception of D-4 and 8. Moreover, the flux vectors showed a relatively small exfiltration flux at B-4 and 5 (denoted by circles in Fig. 4.4b), where ψ exhibited a

slight increase (Fig. 4.3b).

Figures 4.6b and 4.6d illustrate the distributions of ψ in the vertical cross-sections of Lines-V1 and V2, respectively, at the peak of the rainfall event (T2; Fig. 4.3a). In Line-V1, large increases in ψ were detected at C-3M, D-3, E-3, and F-3 (denoted by triangles). As a result, a high pressure zone with exfiltration flux, indicative of preferential flow channel, was continued from B-4 to F-3. In Addition, in Line-V2, a large increase of ψ was detected at B-9, C-7, D-6, E-5, and F-4M (denoted by triangles).

It should be noted that the preferential flow occurred within the area beneath the perched water, indicative of the weathered bedrock layer discussed above (i.e., E-3 and F-3 in Line-V1; C-7 and D-6 in Line-V2). These results indicate that lateral flow accumulated from the upslope area flowed into fractures in the weathered bedrock layer and acted as a preferential flow. Montgomery et al. (2002) also reported sharp and large ψ increases with exfiltrating hydraulic gradients during storm events in the weathered bedrock layer, which showed ψ waveforms similar to our results (i.e. E-5 in Fig. 4.3b). Thus, the following hydraulic properties were assumed for the weathered bedrock layer: the upper part of the layer had low permeability, which prevented the infiltration of water derived from perennial groundwater at B-4 and 5 (denoted by a circle in Fig. 4.6a) under a no-rainfall condition. Conversely, the lower part of the layer had high permeability compared to the upper part as a result of the fractures, which acted as a preferential flow channel and flushed the water derived from the lateral flow accumulated from the upslope area during a rainfall event.

4.3.1.3 Seasonal variability in ψ and hydrological data

Figure 4.7a summarizes the temporal variations in the hydrograph of the bedrock groundwater spring and trench flow throughout the observation period in 2011. Figure 4.7b also summarizes the temporal variations in the ψ values at representative points: B-4 and 5, C-1, and E-2 and 5 (the same points as shown in Fig. 4.3b). A hyetograph is also shown in Figure 4.7b.

At B-4 and 5, where especially high ψ values and exfiltration flux were detected under the no-rainfall condition (circles in Figs. 4.4b and 4.4c), high ψ values were maintained throughout the observation period, showing delayed peaks corresponding to large rainfall inputs during heavy storm events, followed by gradual recession limbs. These waveforms were quite similar to that of the bedrock groundwater spring in the old landslide scarp, which is located at about the same level as points B-4 and 5 (the left panel in Fig. 2.2). Such delayed responses, only to heavy storm events, and gradual recession limbs are distinctive trends of the bedrock groundwater level and seepage flow through bedrock fractures (Hirose et al., 1994; Onda et al., 2001; Katsura et al., 2008; Kosugi et al., 2008). These results confirmed that perennial groundwater is seeping from B-4 and 5, just as with the bedrock spring in the scarp. Moreover, it is presumed that perennial groundwater seepage also exists at
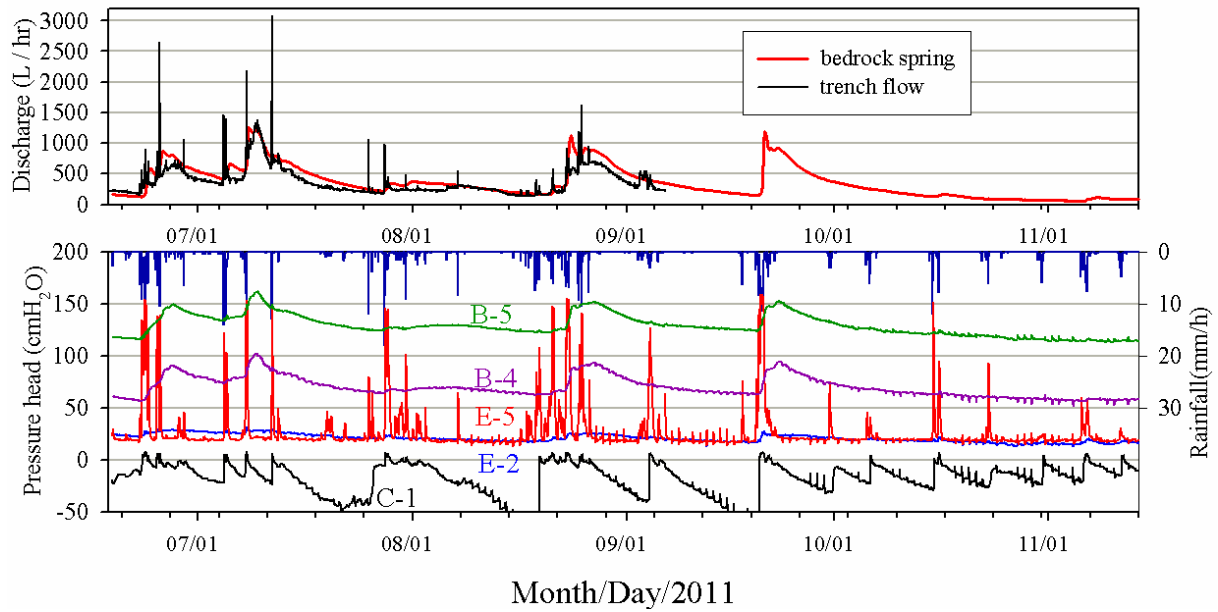
Fig. 4.7 (a) Temporal variations in the hydrograph of a bedrock groundwater spring in the old landslide scarp and trench flow from June to November 2011. (b) Temporal variations in pressure head, ψ, at B-4 and 5, C-1, and E-2 and 5 from June to November 2011.

C-9, where an isolated saturated area was observed at the soil-bedrock interface (Fig. 4.4b).

      Additionally, the trench flow volume under no-rainfall periods was quite similar to the ψ waveform at B-4 and 5. This result implies that almost all of the base flow discharge from the studied hillslope consists of the perennial groundwater seepage at B-4 and 5 and C-9 because the upper region of these points (i.e., points in Line-A) was dry, with relatively little water flux under the no-rainfall condition (e.g., Figs. 4.4b and 4.5a).

      At E-2, ψ remained positive throughout the observation period and exhibited a waveform similar to B-4 and 5 except for a slight ψ variation. This indicates that the perennial groundwater from B-4 and 5 spreads toward the lower region and supplies water constantly. At the region where the perennial groundwater was not supplied constantly, ψ should show rapid peaks with near-zero values coinciding with rainfall peaks, with negative values during no-rain periods, as at C-1.

      At E-5, which was located in the preferential flow channel within the weathered bedrock layer (e.g., Fig. 4.6d), ψ spiked sharply and had fairly high positive values (approximately 150 cmH_2O) coinciding with individual rainfall peaks. During no-rainfall periods, the ψ values remained uniform, just as at E-2, indicating that the perennial groundwater was supplied constantly at E-5 despite the low permeability of the layer of weathered bedrock. Because the amount of accumulated water was plentiful in the lower section of the slope, it is considered to have infiltrated through the low permeability layer, as shown in the large vertical infiltration flux at E-5 and F-4 (Fig. 4.6d).

4.3.2 Model calculation

4.3.2.1 Estimated distribution of hydraulic properties

   To reproduce the observed heterogeneous ψ distributions, spatial distributions of the hydraulic properties were assigned as shown in Figures 4.8 and 4.9. Figure 4.8 shows the estimated distribution of the hydraulic properties in the vertical cross-sections for each line. Figure 4.9 shows the locations of the weathered bedrock layer (low permeability soil and fractured soil), bedrock groundwater seepage area (source term), and water intake/outtake in the top view. The hydraulic properties of the surface soil were assigned to the triangular prisms facing the ground surface. The hydraulic properties of the subsurface soil were also assigned to the triangular prisms above the bedrock surface, except for the weathered bedrock layer. The heterogeneous hydrological properties of the weathered bedrock layer discussed above were represented as follows. We set a low permeability soil so that the water infiltration would be intercepted and perched water would be generated in the middle layer. Moreover, we set fractured soil having a relatively high hydraulic conductivity beneath the low permeability soil so that water could be drained under the no-rainfall condition and preferentially flow at the rainfall event.
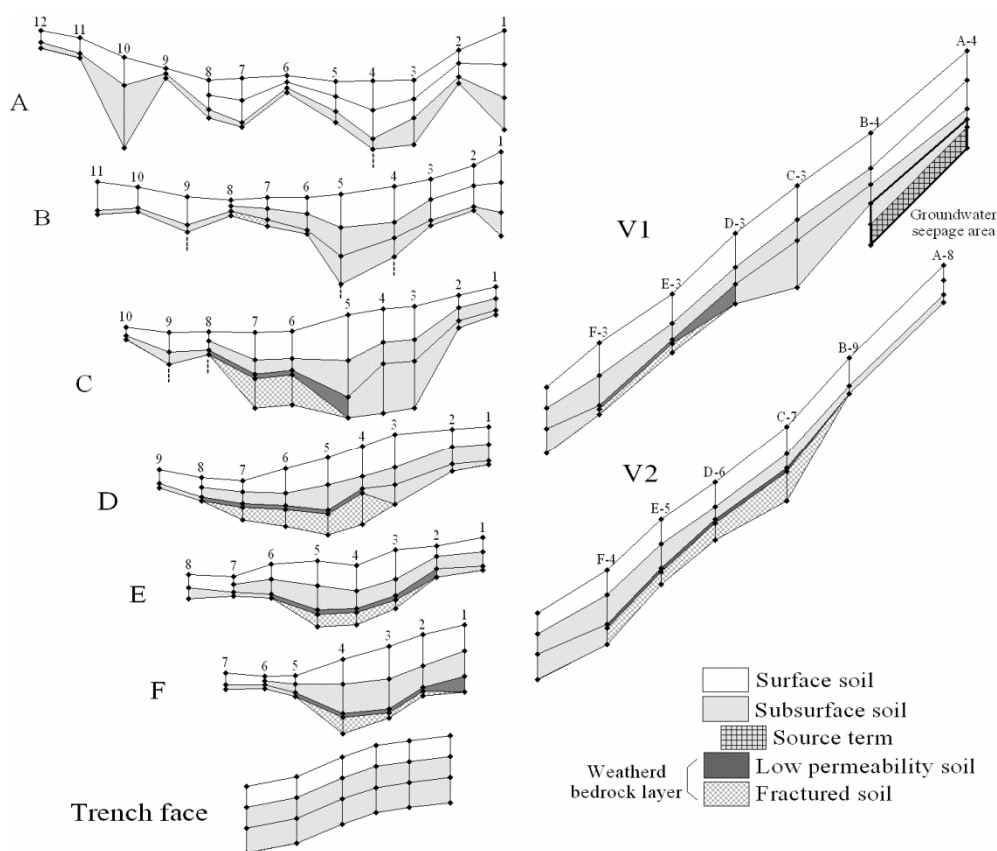

Fig. 4.8 Estimated distribution of hydraulic properties in vertical cross-sections in Lines-A to F, Lines- V1 and V2, and trench face. Dots denote the vertices of triangular prisms.
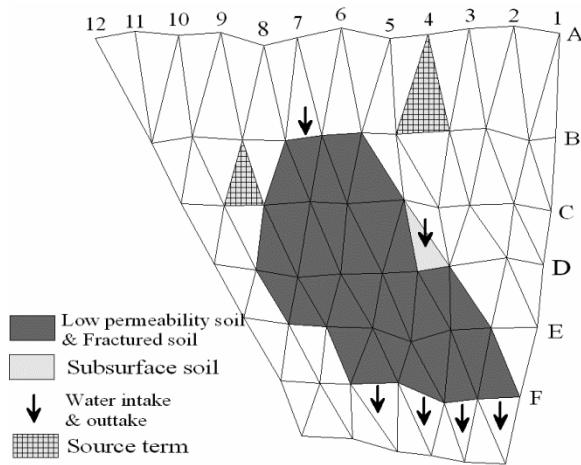
Fig. 4.9 Locations of weathered bedrock layer (low permeability soil and fractured soil), bedrock groundwater seepage area (source term), and water intake/outtake in top view.

To force the water flow above the low permeability soil area under the no-rainfall condition, the bedrock surface and low permeability soil were cohered to cover the fractured soil (e.g., C-5 and C-8 in Line-C and B-9 in Line-V2; Fig. 4.8). The lower end of the fractured soil area was not covered so that water could be drained from the area constantly (e.g., F-4 in Line-V2; water outtake in Fig. 4.8). Moreover, the area surrounded by points C-5 and D-3 and 4 was not covered by the low permeability soil to allow it to take water into the fractured soil in the lower section of the slope. Moreover, between B-7 and 8, the low permeability soil area just above the bedrock surface was opened to allow lateral flow into the fractured soil area during a rainfall event (water intake; Fig. 4.9).

The soil parameters used in the calculations were K_s, θ_s-θ_r, ψ_m, and σ, which are common to the lognormal distribution (LN) model (Kosugi, 1996) shown in Eqs. [2-1], [2-2], and [2-3]. The value of K_s was arbitrarily assumed to reproduce the observed ψ distributions. The other parameters, θ_s-θ_r and ψ_m, were estimated from the empirical relationships with K_s obtained by soil core samples collected near the study site (left panel in Fig. 2.2), and σ was fixed as the average of the observed values. In the LN model, K_s is correlated with ψ_m and σ (Kosugi, 1997) as follows:

$$\log K_s = \log B + \log \exp(\sigma^2) - 2\log(-\psi_m) \qquad [4\text{-}1]$$

where B is a constant. When σ is fixed, Eq. [4-1] shows a linear relationship between $\log K_s$ and $\log(-\psi_m)$. Figure 4.10a plots the observed and functional $\log K_s$ vs. $\log(-\psi_m)$ relationships. The functional $\log K_s$ vs. $\log(-\psi_m)$ curve expressed by Eq. [4-1] was derived by optimizing the constant B. Figure 4.10a shows that the plots of Eq. [4-1] fit the observation data well. Therefore, the value of ψ_m was estimated from this relationship. The value of K_s is also related to the effective porosity, θ_s-θ_r (e.g., Ahuja et al., 1989). The observed K_s had a linear correlation ($R^2 = 0.91$) with θ_s-θ_r, as shown in Figure 4.10b. Thus, the value of θ_s-θ_r was estimated from K_s by using the approximate equation shown in Figure 4.10b.
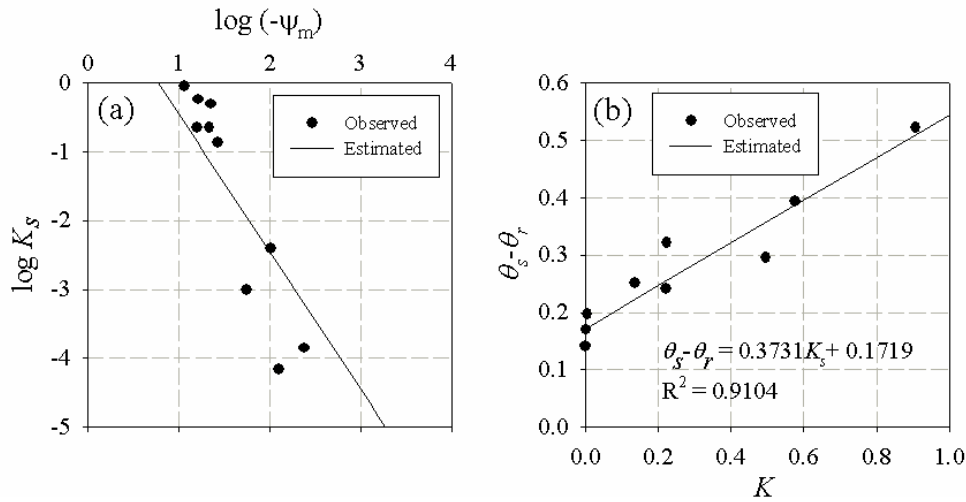
Fig. 4.10 (a) Observed log K_s vs. log($-\psi_m$) data and functional curve fitted by Eq. [4-1]. (b) Observed K_s vs. θ_s-θ_r data and regression line. The approximate equation and R^2 value are also shown.

Table 4.1 Soil hydraulic parameters K_s, θ_s-θ_r, ψ_m, and σ of four types of soil used in model calculations: surface soil, subsurface soil, low permeability soil, and fractured soil.

	θ_s-θ_r	ψ_m[cm]	σ	K_s[cm/s]
Surface soil	0.209	-18.9	1.89	0.1
Subsurface soil	0.173	-133	1.89	0.002
Low permeability soil	0.172	-5973	1.89	0.000001
Fractured soil	0.179	-42.2	1.89	0.02

Table 4.1 summarizes the soil hydraulic parameters, K_s, θ_s-θ_r, ψ_m, and σ, of four types of soil used in the model calculations: surface soil, subsurface soil, low permeability soil, and fractured soil.

4.3.2.2 Rainfall and groundwater input

The runoff from hillslopes can be separated into direct runoff and base flow (Chapman, 1999). The base flow is generally regarded to be caused by the bedrock groundwater, and the direct runoff is considered to result from transient water during a storm event. Figure 4.11a shows the discharge volume of trench flow from 21 to 25 June 2011. Note that unit of discharge volume was converted into mm/hr by dividing by the study area (74.0 m^2). Because the trench flow volume under the no-rainfall periods exhibited a waveform that was quite similar to ψ at B-4 and 5 (Figs. 4.7a and 4.7b), the base flow volume was estimated by fitting the waveform of ψ at B-4, which is also shown in Figure 4.11a. By subtracting the estimated base flow volume from the observed trench flow volume,
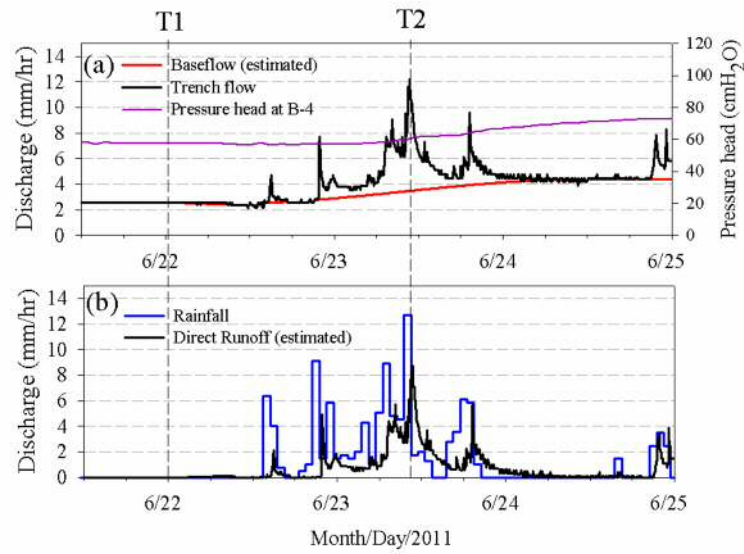
Fig. 4.11 (a) Volumes of observed trench flow, estimated base flow, and pressure head, ψ, at point B-4 and (b) volume of estimated direct runoff and hyetograph from 21 to 25 June, 2011. Broken lines indicate time points T1 and T2.

the direct runoff volume was estimated, as shown in Figure 4.11b. The direct runoff showed nearly the same peak values as the rainfall input, indicating that the contributing area for direct runoff roughly corresponded to the study area, whereas the study area had a broader upslope area (left panel in Fig. 2.2). The rainfall input in the upslope area was considered to be consumed by evapotranspiration or infiltration into deep bedrock. Thus, in the model calculation, the water input from the upslope area was not counted. Hourly records of precipitation rates were imposed on the ground surface of the model domain.

The groundwater seepage in the model is represented as a source term. At the groundwater seepage area, extra triangular prisms with two layers were added beneath the bottom of the domain. The source term was assigned to the lower layer of these extra prisms (A-4 and B-4 in Line-V1; Fig. 4.8). The source terms were assigned at the area surrounded by points B-4 and 5 and A-4 in the upper right section of the slope, and the area surrounded by points C-8, 9, and B-9 in the middle left section of the slope (Fig. 4.9). The estimated base flow volume (Fig. 4.11a) was imposed on the right and left source terms using a ratio of ten to one.

4.3.2.3 Calculated ψ distribution under no-rainfall condition

First, a model calculation was conducted to reproduce the ψ distribution under a no-rainfall condition. At all the calculation nodes, the initial ψ values were set to -30 cmH$_2$O. The base flow volume at T1 (Fig. 4.11a) was input to the source terms constantly for 72 hr to establish a steady condition. During the calculation, no rainfall values were input.
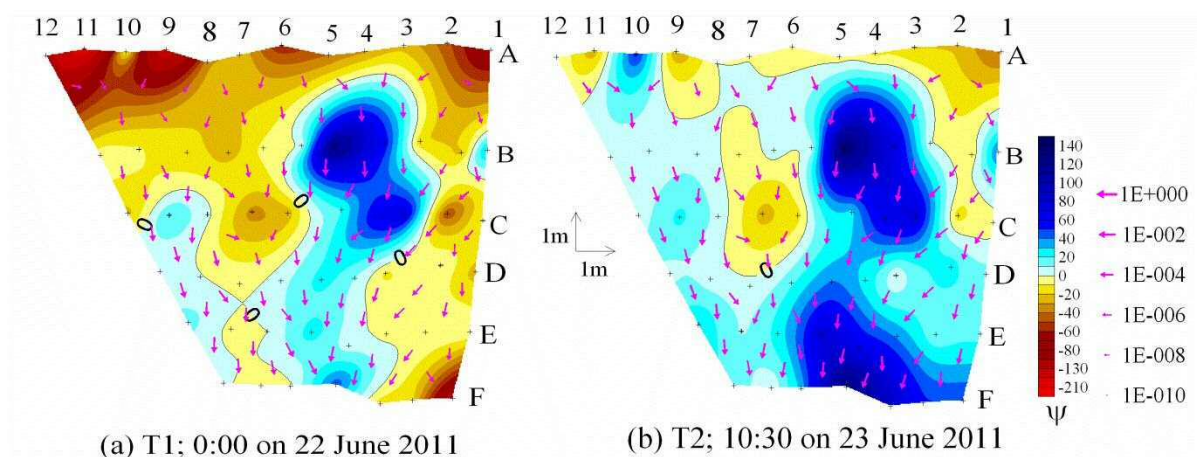
Fig. 4.12 Distributions of calculated pressure head, ψ, at the soil-bedrock interface at time points (a) T1 and (b) T2. Arrows denote the calculated magnitude and direction of water flux vectors.

Figure 4.12a illustrates the calculated ψ distribution at the soil-bedrock interface under the no-rainfall condition (T1; Fig. 4.3a). The crosses in Figures 12, 13, and 14 denote the vertices of the triangular prisms (the same as the dots in Fig. 4.8). The saturated area was generated from B-4 and 5 and C-9 where source terms were assigned (Fig. 4.9) and spread toward the lower region. In particular, high ψ values (approximately 120 cmH$_2$O) were calculated at B-4 and 5. These characteristics corresponded well to the observed ψ distribution (Fig. 4.4b). At C-6 and 7, where the hydraulic properties of the weathered bedrock layer were assigned, ψ showed negative values, which also corresponded to the observed data. However, a saturated area was calculated at D-4, 5, and 6, where ψ showed negative values in the observed distribution. Figure 4.13a illustrates the calculated ψ distributions in the vertical cross-sections of Lines-A to F before the rainfall event (T1; Fig. 4.3a). In Line-A, a relatively dry condition was calculated within the unsaturated region compared to the observed ψ distributions (Fig. 4.5a). In Lines-B and C, the ψ distributions notably corresponded to the observed data (Fig. 4.5a): a saturated area with high ψ values was calculated within a bedrock hollow at B-4 and 5 and no exfiltration flux was calculated. At C-6 and 7, where the observed ψ values were negative above the bedrock surface, the perched saturated area in the middle layer was successfully reproduced. The perched saturated area was also reproduced from D-5 to 8 in Line-D. However, a saturated area was also calculated just above the bedrock surface at these points. In addition, the ψ values above the bedrock surface were negative at D-1 to 3. These did not correspond to the observed data, which showed positive values at these points. In Lines-E and F, the groundwater level was lower than the observed data, and the ψ values above the bedrock surface were negative in the right sections of the lines. Figures 4.14a and 4.14c illustrate the distributions of the calculated ψ in the vertical
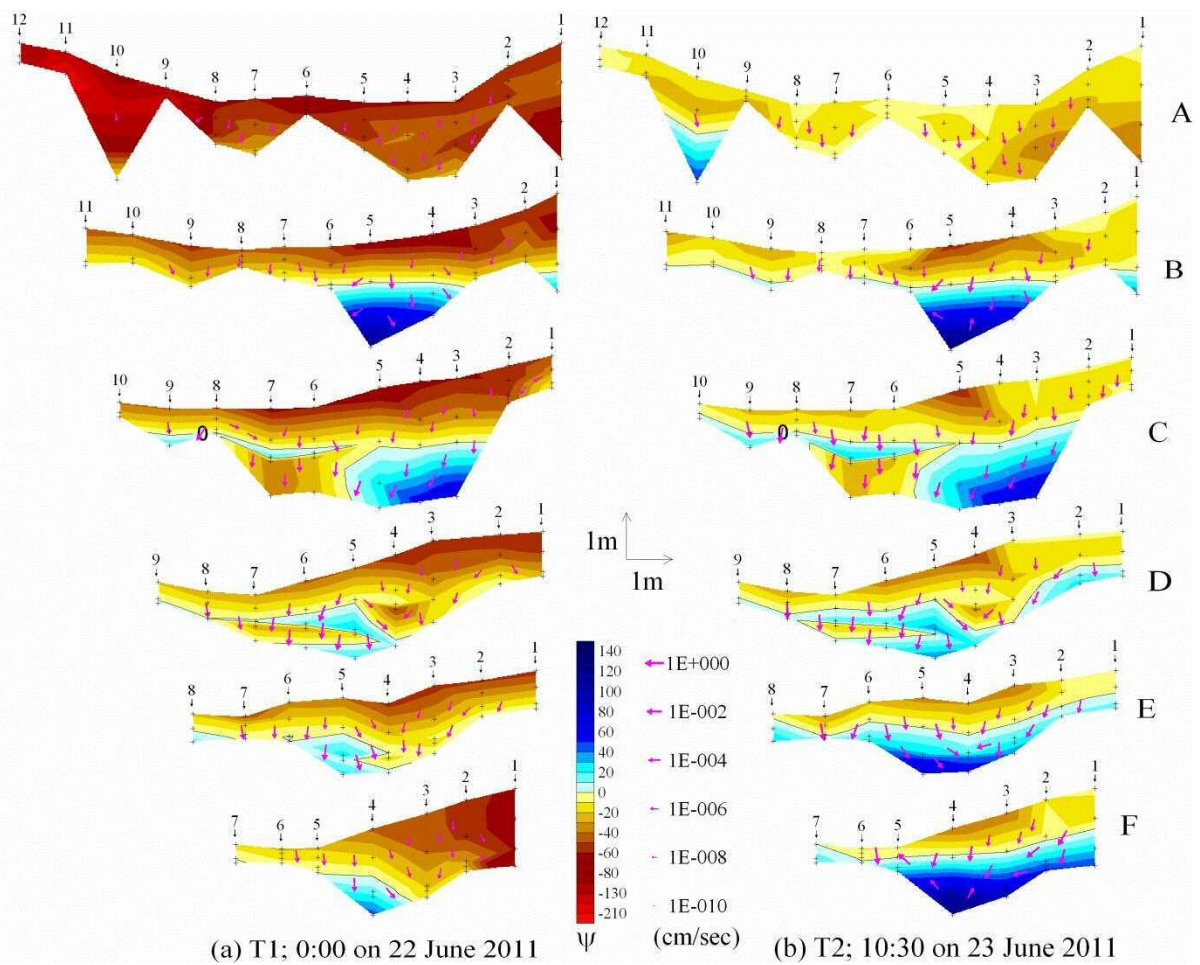
Fig. 4.13 Distributions of calculated pressure head, ψ, in the vertical cross-sections of Lines-A to F at time points (a) T1 and (b) T2. Arrows denote the calculated magnitude and direction of water flux vectors.

cross-sections of Lines-V1 and V2, respectively, under the no-rainfall condition (T1; Fig. 4.3a). The sudden appearance of groundwater between A-4 and B-4 was well reproduced compared to the observation data (Fig. 4.6a). However, the perched water in the middle layer at E-3 and F-3 was not calculated. Conversely, in Line-V2 (Fig. 4.14c), the perched saturated area and large lateral flow were calculated in the middle layer of C-7 and D-6, which corresponded well with the observed distribution (Fig. 4.6c).

Thus, the observed heterogeneous ψ distributions such as the bedrock groundwater seepage and perched water were reproduced well in the model calculation by introducing the source terms and stratified soils having high and low hydraulic conductivities in the weathered bedrock layer.
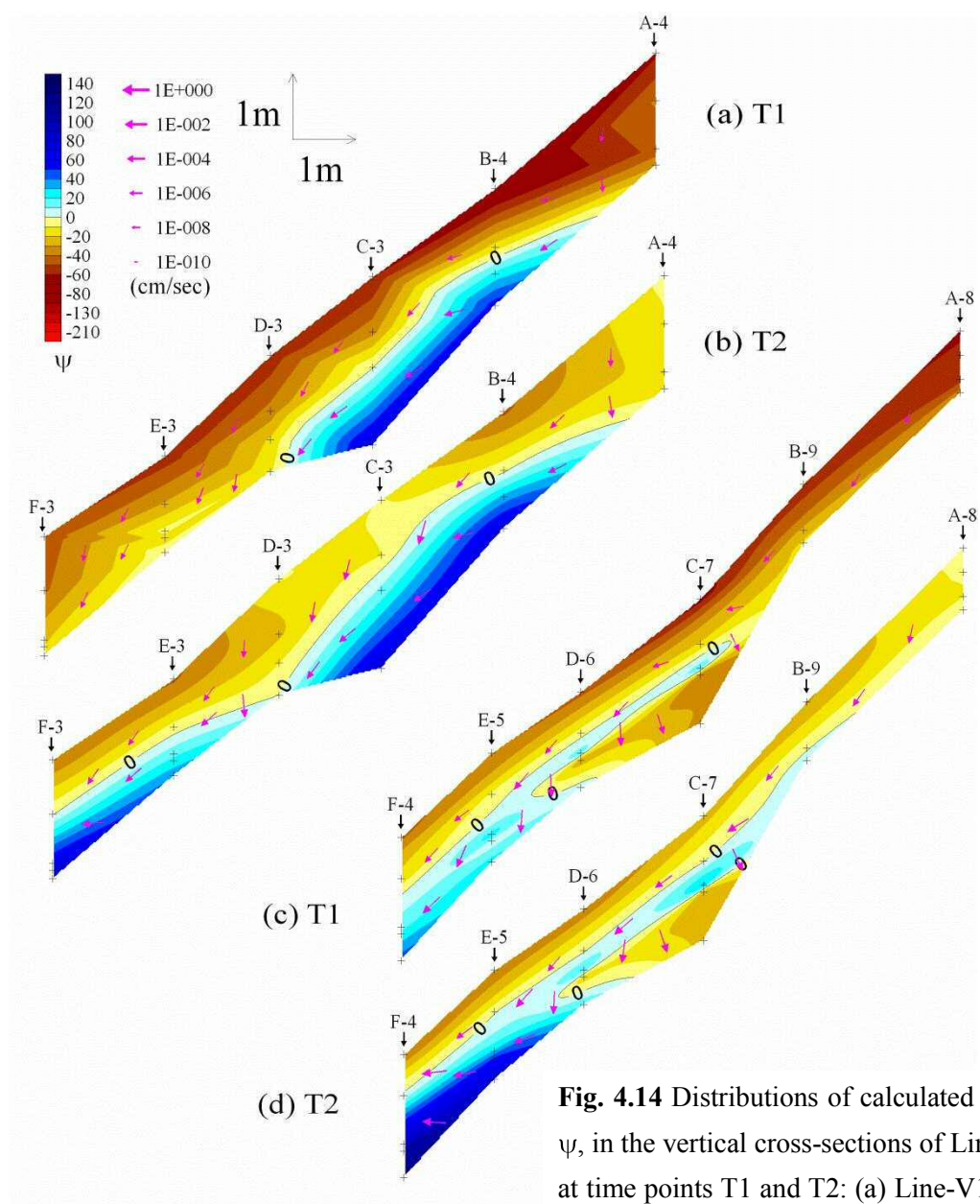
Fig. 4.14 Distributions of calculated pressure head, ψ, in the vertical cross-sections of Lines-V1 and V2 at time points T1 and T2: (a) Line-V1 at T1 and (b) T2 and (c) Line-V2 at T1 and (d) T2. Arrows denote the calculated magnitude and direction of water flux vectors.

4.3.2.4 Calculated ψ distribution at the peak of rainfall

Next, another calculation scenario was conducted to reproduce the ψ distribution at the peak of the rainfall event. The initial ψ values were set to the calculated ψ under the no-rainfall condition (T1; e.g., Fig. 4.12a) described above. The hourly precipitation (Fig. 4.11b) and base flow volume (Fig. 4.11a) from 22 to 25 June 2011 were input.

Figure 4.12b illustrates the calculated ψ distribution at the soil-bedrock interface at the peak of the rainfall (T2; Fig. 4.3a). Although a transient saturated zone covered the slope widely, negative ψ values were calculated at C-6 and 7. The continuous high pressure zones observed in the right and left sections (Fig. 4.4e) were not calculated. Nonetheless, the high pressure zone was calculated in Lines-E and F, corresponding to the observed data. Figure 4.13b illustrates the calculated ψ distributions in the vertical cross-sections of Lines-A to F before the rainfall event (T1; Fig. 4.3a). Although the saturated water level was lower than that in the observed data (Fig. 4.5b), the high pressure zones above the bedrock surface in Lines-E and F were successfully reproduced. It is notable that an exfiltration flux was calculated within the high pressure zone in Line-F, considering the fact that the accumulated water exceeded the transmission capacity of the weathered bedrock layer (Roger and Selby, 1980; Pierson, 1983; Uchida et al., 2004). Figures 4.14b and 4.14e illustrate the distributions of the calculated ψ in the vertical cross-sections of Lines-V1 and V2, respectively, at the peak of the rainfall (T2; Fig. 4.3a). In Line-V1, although ψ did not increase at D-3, a continuous high ψ area was calculated at E-3 and F-3, corresponding to the observed data (Fig. 4.6b). In Line-V2, a continuous high ψ area was also calculated at E-5 and F-4. However, negative ψ values were calculated at C-7 and D-6, where the observed ψ values showed a large increase (Fig. 4.6d).

Thus, the high pressure zones in the right and left sections of the slope generated at the peak of the rainfall were not reproduced by the model calculation. Because of the irregularly developed fractures within the weathered bedrock layer, the distribution of the hydraulic conductivity was considered to be highly heterogeneous. In previous studies that modeled preferential pipe flow, the parallel piped unit domains were separated from the surrounding soil domain, and water flow was solved using Manning's equation (e.g., Tsutsumi et al., 2005). To reproduce the preferential flow using only the distribution of the hydraulic conductivity, a larger finite element grid might be needed. As an alternative, the volume of water flow through the intakes in the model (Fig. 4.9) might not be sufficient to generate preferential flows. It is possible that the water infiltration into the weathered bedrock layer was activated when the vertical preferential flow networks were filled with water as a result of the large hydraulic gradients during storm events. Tsuboyama et al. (1994) found an increase in the macropore flow rate, which they attributed to the extension of macropore networks during wetter conditions. Nonetheless, the model calculation successfully reproduced the hydrological process at the rainfall event, where water flows into a weathered bedrock layer through water intakes, and the accumulated water generated excess pore water pressure at the lower section of the slope.

4.4 Conclusions

We analyzed the high-resolution and three-dimensional water movement data obtained by intensive tensiometer measurements to clarify the hydrological process, including heterogeneous

phenomena, in detail. Under a no-rainfall condition, especially high ψ values with an exfiltration flux were detected at points B-4 and 5 in the upper section of the slope. At these points, the temporal ψ waveforms showed delayed responses only to heavy storm events and gradual recession limbs, which indicated the existence of perennial groundwater seepage flow through bedrock fractures. The seepage water spread in the downslope direction and supplied water constantly to the lower section of the slope. At some points in the center of the slope, a perched saturated area was detected in the middle layer, while ψ exhibited negative values above the bedrock surface.

At the peak of a rainfall event, continuous high pressure zones (i.e., $\psi > 50$ cmH$_2$O) were generated in the right and left sections of the slope. Both of these high pressure zones converged at the lower region, showing a sharp ψ spike up to 100 cmH$_2$O. Along the high pressure zones, flux vectors showed large values and water exfiltration, indicating the occurrence of preferential flow. Moreover, the preferential flow occurred within the area beneath the perched water, indicating the existence of a weathered bedrock layer. This layer had low permeability, which prevented the vertical infiltration of water in the upper part of the layer, but had high permeability as a result of the fractures distributed heterogeneously inside the layer. These fractures acted as a preferential flow channel and flushed the water derived from lateral flow accumulated from the upslope area during the rainfall event.

To reproduce the observed heterogeneous ψ distributions, the spatial distributions of hydraulic properties were estimated and assigned to a physics-based three-dimensional simulation model. The base flow volume, which was estimated from both the observed trench flow and ψ waveform at a groundwater seepage point, was assigned to the source terms. The weathered bedrock layer was represented by stratified soils having high and low hydraulic conductivities. As a result, the model calculation reproduced well the observed heterogeneous ψ distributions such as the bedrock groundwater seepage under a no-rainfall condition. Moreover, the model calculation successfully reproduced the hydrological process at a rainfall event, where water flowed into the weathered bedrock layer through water intakes, and accumulated water generated an excess pore water pressure at the lower section of the slope, although the high pressure zones in the right and left sections of the slope were not reproduced.

As a consequence, the three-dimensional hydrological process including heterogeneous phenomena in the studied hillslope was elucidated, and the hydraulic properties such as the water supply and spatial distribution of the hydraulic conductivities were estimated. The hydrological process was well reproduced by the model calculation. In future studies, this study will contribute to the improvement of runoff/landslide prediction which takes into account the heterogeneous hydrological properties.

References

Ahuja, L.R., D.K. Cassel, R.R. Bruce, and B.B. Barnes. 1989. Evaluation of spatial distribution of hydraulic conductivity using effective porosity data. Soil Science 148(6):404-411.

Barcelo, M.D., and J.L. Nieber. 1981. Simulation of the hydrology of natural pipes in a soil profile. American Society of Agricultural Engineering, Paper No. 81-2026.

Barcelo, M.D., and J.L. Nieber. 1982. Influence of a soil pipe network on catchment hydrology. American Society of Agricultural Engineering, Paper No. 82-2027.

Chapman, T.G. 1999. A comparison of algorithms for streamflow recession and baseflow separation. Hydrol. Process. 13:701-714.

Freer, J., J.J. McDonnell, K.J. Beven, N.E. Peters, D.A. Burns, R.P. Hooper, B. Aulenbach, and C. Kendall. 2002. The role of bedrock topography on subsurface storm flow, Water Resour. Res. 38(12): 1269, doi: 10.1029/2001WR000872.

Fujimoto, M., K. Kosugi, Y. Hayashi, M. Tani, and T. Mizuyama. 2011. The effect of resolution of elevation model data on shallow land slide analysis. (In Japanese, with English abstract.) J. Jpn. Soc. Erosion Cont. Eng. 64(3):3-10.

Geuzaine, C., and J.F. Remacle. 2009. Gmsh: a three-dimensional finite element mesh generator with built-in pre- and post-processing facilities. Int. J. Number. Meth. Engng. 0:1-24.

Hopp, L., and J.J. McDonnell. 2009. Connectivity at the hillslope scale: Identifying interactions between storm size, bedrock permeability, slope angle and soil depth. J. Hydrol. 376: 378-391, doi: 10.1016/j.jhydrol.2009.07.047.

Jones, J.A.A., and L.J. Connelly. 2002. A semi-distributed simulation model for natural pipeflow. J. Hydrol. 262(1–4): 28-49. doi: 10.1029/2006/JF000509.

Jones, J.A.A., E.A. Sudicky, and R.G. McLaren. 2008. Application of a fully-integrated surface-subsurface flow model at the watershed-scale: A case study. Water Resour. Res. 44. W03407, doi: 10.1029/2006WR005603.

Jones, J.A.A. 2010. Soil piping and catchment response. Hydrol. Process. 24: 1548-1566, doi: 10.1002/hyp.7634.

Hirose T., Y. Onda, and Y. Matsukura. 1994. Runoff and solute characteristics in four small catchments with different bedrocks in the Abukuma mountains. Transactions, Jpn. Geomorphol. Uni. 15A: 31-48.

Katsura, S., K. Kosugi, N. Yamamoto, and T. Mizuyama. 2005. Saturated and unsaturated hydraulic conductivities and water retention characteristics of weathered granitic bedrock. Vadose Zone J. 5: 35–47, doi: 10.2136/vzj2005.0040.

Katsura, S., K. Kosugi, T. Mizutani, S. Okunaka, and T. Mizuyama. 2008. Effects of bedrock groundwater on spatial and temporal variations in soil mantle groundwater in a steep granitic headwater catchment. Water Resour. Res. 44: W09430, doi: 10.1029/2007WR006610.

Kosugi, K. 1996. Lognormal distribution model for unsaturated soil hydraulic properties. Water Resour. Res. 32(9): 2697-2703.

Kosugi, K. 1997. New diagrams to evaluate soil pore radius distribution and saturated hydraulic conductivity of forest soil. J. For. Res. 2:95-101.

Kosugi, K., S. Katsura, M. Katsuyama, and T. Mizuyama. 2006. Water flow processes in weathered granitic bedrock and their effects on runoff generation in a small headwater catchment. Water Resour. Res. 42: W02414, doi: 10.1029/2005WR004275.

Kosugi, K., S. Katsura, T. Mizuyama, S. Okunaka, and T. Mizutani. 2008. Anomalous behavior of soil mantle groundwater demonstrates the major effects of bedrock groundwater on surface hydrological processes. Water Resour. Res. 44: W01407, doi: 10.1029/2006WR005859.

Istok, J. 1989. Groundwater Modeling by the Finite Element Method. Water Resour. Monogr. Ser. 13:495 pp., AGU, Washington, D. C.

Montgomery, D.R., W.E. Dietrich, R. Tress, S.P. Anderson, J.T. Heffner, and K. Loague. 1997. Hydrologic response of a steep, unchanneled valley to natural and applied rainfall. Water Resour. Res. 33(1): 91-109.

Montgomery, D.R., W.E. Dietrich, and J.T. Heffner. 2002. Piezometric response in shallow bedrock at CB1: Implications for runoff generation and landsliding. Water Resour. Res. 38(12): 1274, doi: 10.1029/2002WR001429.

Nishiguchi Y., T. Uchida, T. Mizuyama, and K. Kosugi. 2005. An observation of spatial pore water pattern in a mountain hollow. (In Japanese, with English abstract.) J. Jpn. Soc. Erosion Cont. Eng. 57(5): 53-58.

Onda, Y., Y. Komatsu, M. Tsujimura, and J. Fujihara. 2001. The role of subsurface runoff through bedrock on storm flow generation. Hydrol. Process. 15:1693-1706, doi: 10.1002/hyp.234.

Pierson, T.C. 1983. Soil pipes and slope stability. Quality J. Engineering Geol. 16: 1-11.

Roger N.W., and M.J. Selby. 1980. Mechanisms of shallow translational landslide during summer rainstorm: North Island, New Zealand. Geografiska Annaler 62A: 11-21.

Terajima, T., and K. Moroto. 1990. Stream flow generation in a small watershed in granitic mountain. (In Japanese, with English abstract.) Transactions, Jpn. Geomorphol. Uni. 11:75-96.

Tsuboyama, Y., R. C. Sidle, S. Noguchi, and I. Hosoda. 1994. Flow and solute transport through the soil matrix and macropores of a hillslope segment. Water Resour. Res. 30:879-890.

Tsutsumi, D., R.C. Sidle, and K. Kosugi. 2005. Development of a simple lateral preferential flow model with steady state application in hillslope soils. Water Resour. Res. 41, W12420, doi: 10.1029/2004WR003877.

Uchida, T., K. Kosugi, and T. Mizuyama. 2001. Effects of pipeflow on hydrological process and its relation to landslide: a review of pipeflow studies in forested headwater catchments. Hydrol. Process. 15: 2151-2174, doi: 10.1002/hyp.281.

Uchida, T., Y. Asano, T. Mizuyama, and J.J. McDonnell. 2004. Role of upslope soil pore water pressure on subsurface stormflow dynamics. Water Resour. Res. 40(12) doi: 10.1029/2003WR002139.

Wilkinson, P.L., M.G. Anderson, and D.M. Lloid. 2002. An integrated hydrological model for rain-induces landslide prediction. Earth Surf. Process. Landforms 27: 1285-1297, doi: 10.1002/esp.409.

CHAPTER 5

The use of long-term intensive measurements of soil pore water pressure to analyze temporal variations in hydrological processes on a hillslope

5.1 Introduction

Previous studies have suggested that specific heterogeneous hydrological phenomena vary in magnitude and position over time. Preferential pipe flow (e.g., Uchida et al., 2001; Jones, 2010) exhibits temporal variations in location and flow volume. Lateral water flow through preferential pipes contributes to subsurface soil erosion, which develops the pipe network (e.g., Tsukamoto et al., 1988; Brian and Jones, 1997; Holden, 2006). The improved drainage capacity within the enhanced pipe network may dissipate the perched water table during a rainfall event (McDonnell, 1990; Sidle et al., 1995). In contrast, water readily fills the pipe cavity when it is plugged, which leads to local elevation of soil pore water pressure in the surrounding soil matrix during a rainfall event. These concepts of pipe flow processes were estimated using relatively short-term outlet discharge data from pipes, point-scale tensiometric data from field observations, and bench-scale experiments (e.g., Pierson, 1983).

Weathering of bedrock may also change hydrological properties on a hillslope, such as the topography of the bedrock surface, which controls subsurface storm flow patterns (Freer et al., 2002). Moreover, bedrock fractures developed by weathering contribute to changes in hydrological properties. Heterogeneously distributed fractures in the near-surface bedrock create large spatial variability in hydraulic conductivity (e.g., Olofsson et al., 1994; Montgomery et al., 1997, 2002). However, these processes of temporal variation in hydrological properties have not been observed directly in the field by long-term water movement measurements.

The objective of this chapter was to trace the variation in hydrological processes using long-term hydrological observations. We analyzed 4 years of observational data from the study hillslope based on the results of three-dimensional water movement observations presented in Chapter 4.

5.2 Materials and Methods
5.2.1 Tensiometer observations

We continuously monitored the soil pore water pressure (soil matric pressure head, ψ) at the
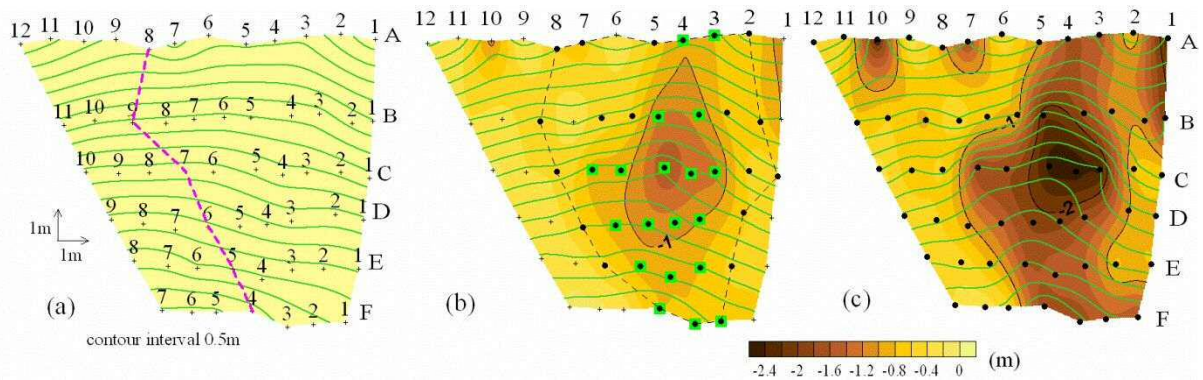
Fig. 5.1 (a) Ground surface topographic map and locations of all observation points. The broken line indicates the location of the vertical cross-section shown in Fig. 5.5, passing through A-8, B-9, C-7, D-6, E-5, and F-4. (b) Middle layer topographic map and soil thickness distribution from ground surface to the middle layer. Dots and squares denote the tensiometers installed in shallow and middle layers, respectively. Tensiometers were not installed in shallow and middle layers outside the domain bounded by the broken line. (c) Bedrock surface topographic map and soil thickness distribution from ground surface to bedrock surface. Dots denote tensiometers installed at the soil–bedrock interface. The contour interval of each topographic map is 0.5 m.

study site (described in Chapter 2) using densely nested tensiometers. Figure 5.1a shows the ground surface topographic map and locations of all observation points. Figures 5.1b and 5.1c show the topographic maps and soil thickness distributions of the middle layer and bedrock surface, respectively. The bedrock surface was determined by penetration resistance, N_c, which exceeded 100 based on recent studies conducted in granitic watersheds (Katsura et al., 2005; Kosugi et al., 2006). The description of the penetration test using the CPMP is shown in Chapter 3. The middle layer was the midpoint between the bedrock surface and the shallow tensiometers (described below). At points where shallow tensiometers were not installed, the middle layer was the midpoint between the bedrock surface and the ground surface.

From 1 June to 12 October 2008, we monitored ψ with 57 tensiometers installed at the soil–bedrock interface (denoted by dots in Fig.5.1c). The tensiometers were installed at all CPMP observation points (described in Chapter 3) along six horizontal lines (A–F) extending downward from the top of the slope (Fig. 5.1a). After 15 July 2008, we monitored ψ at point C-3 of the middle layer (named as C-3M) at a depth of 130 cm. From 1 June to 1 November 2009, we monitored ψ with an extra 54 tensiometers in addition to the original 57 tensiometers. Thirty-five extra tensiometers were installed at a depth of 30 cm (denoted by dots in Fig. 5.1b), which are referred to hereafter as shallow tensiometers. The other 19 tensiometers were installed in middle layers (denoted by squares in Fig.

5.1b) between the shallow and deep tensiometers at depths of 80–160 cm. We monitored ψ from 15 June to 20 October 2010 and from 15 June to 14 November 2011 with the same set of tensiometers in 2009.

The tensiometers were attached to pressure transducers (PA-850-102V-NGF; Copal Electronics, Shinjuku, Tokyo, Japan). ψ values were recorded at 5-min intervals throughout the observation period using a data logger (CR1000; Campbell Scientific, Logan, UT, USA).

5.2.2 Rainfall and discharge observations

From 1 June 2009, we observed discharge from the bedrock groundwater spring located inside the old landslide scarp adjacent to the study site (left panel in Fig. 2.2). The springwater was channeled into a 0.5-L tipping bucket that was leveled and fixed to a solid structure. Accumulated bucket tips were recorded at 5-min intervals throughout the observation period using the data logger. From 15 June to 6 September 2011, we observed subsurface trench flow from an artificial trench excavated approximately 2 m downslope from Line-F (right panel in Fig. 2.2). We monitored the trench flow volume using a 30° V-noch weir with a water-level recorder (DL/N70; Sensor Technik Sirnach AG, Sirnach, Switzerland) at 5-min intervals throughout the observation period. A rain gauge was placed in an open space on the ridge near the study hillslope (left panel in Fig. 2.2).

5.3 Results and Discussion
5.3.1 Comparison of water flow characteristics between 2009 and 2011
5.3.1.1 No-rainfall condition

We conducted a comparison of ψ variations between 2009 and 2011 to examine the annual changes in the hydrological process. First, we compared the distributions in ψ before the beginning of rainfall at time points T1 and T3, indicated by broken lines in Figures 5.2a and 5.2c. The rainfall amounts at T1 were 26 and 176 mm during the antecedent seven and fourteen days, respectively. Rainfall amount at T3 was 11 and 49 mm during antecedent seven and fourteen days, respectively, and this condition was dryer than that at T1.

Figures 5.3a and 5.3b illustrate the distribution of ψ in the middle layer and at the soil–bedrock interface, respectively, before the beginning of rainfall in 2009 (T1; 15:00 on 16 July 2009). At the points where tensiometers were not installed in the middle layer, ψ for the middle layer was calculated by interpolation of ψ values at shallow depths and the soil–bedrock interface (denoted by only dots in Fig. 5.1b) or by subtracting the difference in elevation head (vertical coordinates) from
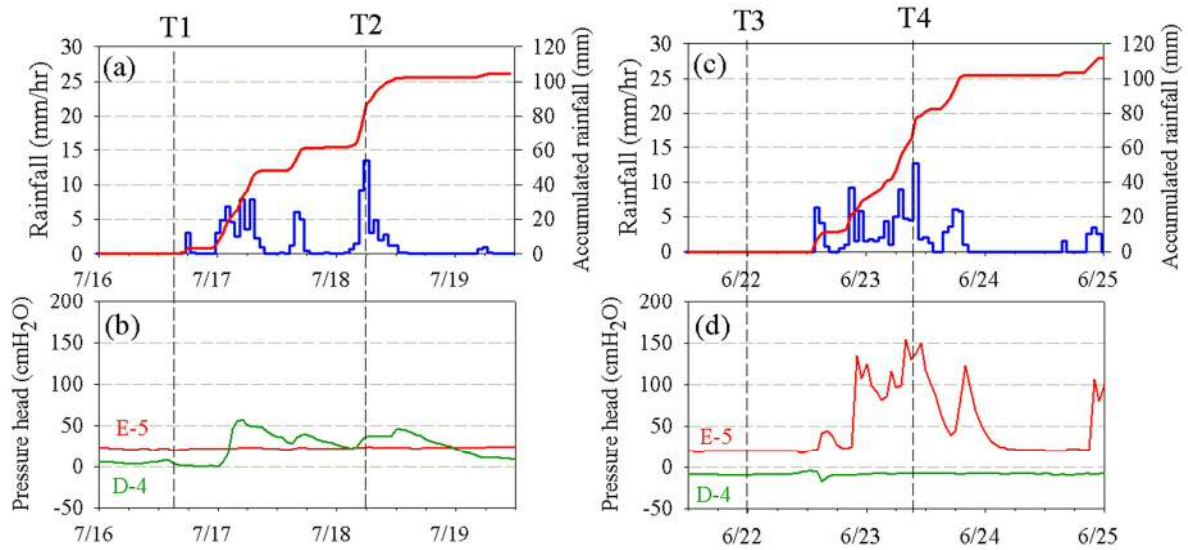
Fig. 5.2 (a) Hyetograph and accumulated rainfall from 16 to 20 July 2009. (b) Temporal variation in pressure head, ψ, at D-4 and E-5 from 16 to 20 July 2009. (c) Hyetograph and accumulated rainfall from 21 to 25 June 2011. (b) Temporal variation in ψ at D-4 and E-5 from 21 to 25 June 2011. Broken lines indicate time points T1–T4.

the ψ value at the soil–bedrock interface (outside the domain bounded by a broken line in Figs. 5.1b and 5.3a). Arrows in the figures denote the value and direction of the water flux vector, q. We set triangular elements composed of three tensiometer position nodes to calculate q. The mean hydraulic gradient in each element was estimated from the hydraulic head (i.e., total head, H) at each node, calculated as the sum of ψ and the vertical coordinates. In addition, hydraulic conductivity, K, for each element was calculated using the functional K-ψ curves shown in Figure 2.5b. Then, q was calculated by multiplying K by the mean hydraulic gradient.

The saturated area ($\psi \geq 0$) started at B-4 and 5 and extended toward the lower region in the middle layer (Fig. 5.3a). Flux vectors mostly pointed downward and showed large values in the saturated area. At the soil–bedrock interface (Fig. 5.3b), the saturated area started at B-4, 5, and C-9 (denoted by circles in Fig. 5.3b) and spread downward. Particularly high ψ values were observed at B-4 and 5 despite no rainfall. Flux vectors pointed downward and were large values in the saturated area. However, ψ showed an unsaturated condition in the middle section of the slope (i.e., C-5 to 7, D-5 to 7, and E-3), where the bedrock surface was hollowed (Fig. 5.1c) and did not correspond to the bedrock topography. At these points, ψ was positive in the middle layer (Fig. 5.3a), indicating the existence of perched water in the middle layer. Flux vectors showed quite small values in the unsaturated area at the soil–bedrock interface due to steep decline of K in the negative ψ range (Fig. 2.5b).

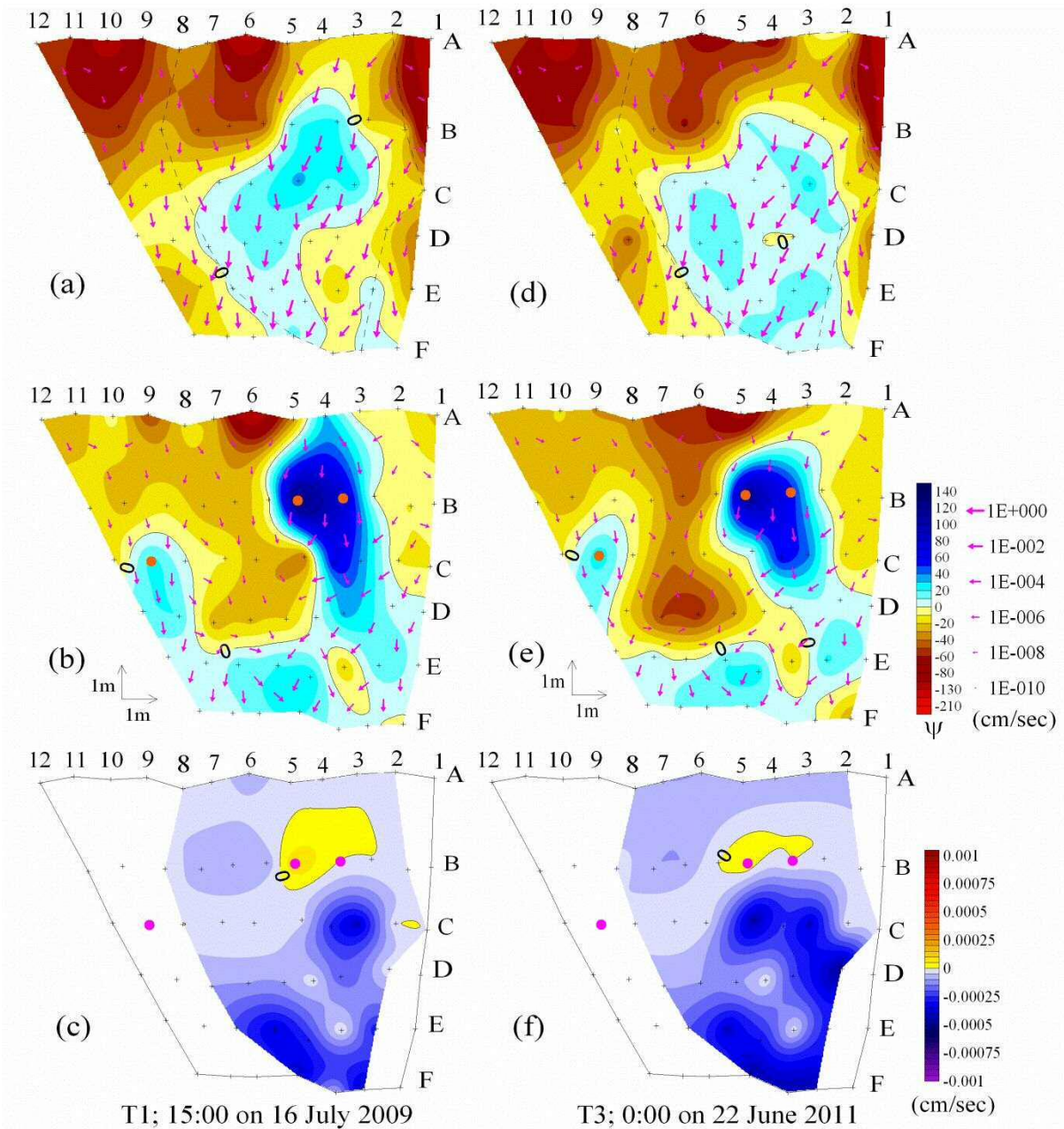T1; 15:00 on 16 July 2009

T3; 0:00 on 22 June 2011

Fig. 5.3 Distributions of pressure head, ψ, (a) in the middle layer and (b) at the bedrock surface, and (c) distribution of the vertical flux value at time point T1, denoted in Fig. 5.2a. Distributions of ψ (d) in the middle layer and (e) at the bedrock surface, and (f) distribution of the vertical flux value at time point T3, denoted in Fig. 5.2c. Circles denote the generation point of the saturated area at the soil–bedrock interface under the no-rainfall condition. Symbols and arrows have the same meaning as in Fig. 5.4. Broken line in (a) and (d) has the same meaning as in Fig. 5.1b.

In comparison with Figures 5.3a and 5.3b, Figures 5.3d and 5.3e illustrate the distribution of ψ in the middle layer and at the soil–bedrock interface, respectively, before the beginning of rainfall in 2011 (T3; 0:00 on 22 June 2011). In the whole area, ψ values were slightly lower than those in 2009 (Figs. 5.3a and 5.3b) due to smaller antecedent precipitation. In particular, the water level at B-4 and 5 at the soil–bedrock interface (Fig. 5.3e) was lower than that in 2009 (Fig. 5.3b). In the middle layer (Fig. 5.3d), the area around E-3M was saturated, whereas it was unsaturated in 2009 (Fig. 5.3a). Nevertheless, the shapes of the saturated area and the directions of the flux vectors in 2011 showed a similar trend to those in 2009 in both the middle layer and the soil–bedrock interface, indicating that the water flow domain under a no-rainfall condition varied only slightly from 2009 to 2011.

Figures 5.3c and 5.3f illustrate the vertical flux distributions in 2009 and 2011, respectively, calculated by multiplying K by the mean hydraulic gradient between the middle layer and soil–bedrock interface at each point. Note that we cut off the data at the points where a tensiometer was installed only at the soil–bedrock interface (outside the domain bounded by a broken line in Fig. 5.1b), because at least two data points are required to estimate the hydraulic gradient. A negative value indicates the infiltration flux, and a positive value indicates the exfiltration flux. Figures 5.3c and 5.3f show that the exfiltration flux existed at B-4 and 5, where particularly high ψ values were observed at the soil–bedrock interface (denoted by circles in Figs. 5.3b and 5.3e), although the infiltration flux was dominant throughout the slope. The result suggests that bedrock groundwater was seeping from B-4 and 5 despite no rainfall. Thus, the vertical flux distribution under a no-rainfall condition also showed similar trends in 2009 and 2011.

5.3.1.2 Peak for rainfall event

We compared the distributions of ψ at the peak of rainfall in 2009 and 2011. We focused on two heavy storm events that occurred from 16 to 19 July 2009 (total rainfall was 103 mm; maximum rainfall was 14 mm/hr; Fig. 5.2a) and from 22 to 24 June 2011 (total rainfall was 102 mm; maximum rainfall was 13 mm/hr; Fig. 5.2c). Figures 5.2a and 5.2c show the hyetographs and accumulated rainfall for the two events, both of which had nearly the same amount and intensity. Figures 5.2b and 5.2d show temporal variations of ψ at points D-4 and E-5.

Figures 5.4a, 5.4b, and 5.4c illustrate the distributions of ψ in the middle layer, ψ at the soil–bedrock interface, and the vertical flux value, respectively, at the peak of rainfall in 2009 (T2; 6:00 on 18 July 2009). In the middle layer (Fig. 5.4a), a transient saturated zone expanded into upslope regions by rainfall infiltration except at E-3M where ψ maintained negative. In particular, a large increase in ψ was observed at C-3M and F-4M (denoted by triangles in Fig. 5.4a). The flux vectors
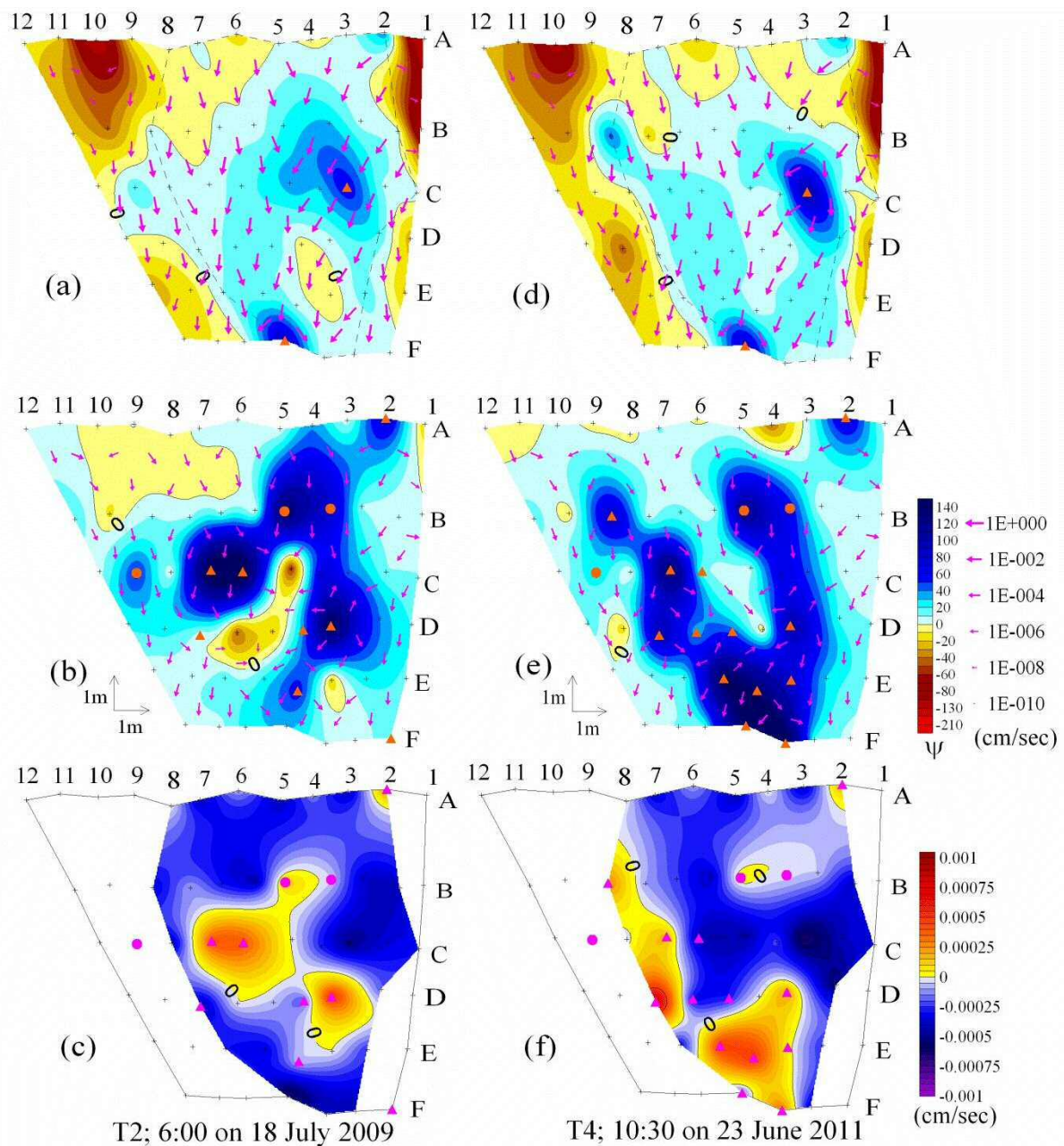
Fig. 5.3 Distributions of pressure head, ψ, (a) in the middle layer and (b) at the bedrock surface, and (c) distribution of vertical flux value at time point T2, denoted in Fig. 5.2a. Distributions of ψ (d) in the middle layer and (e) at the bedrock surface, and (f) distribution of vertical flux value at time point T4, denoted in Fig. 5.2c. Circles denote the generation point of the saturated area at the soil–bedrock interface under the no-rainfall condition. Triangles denote points showing a large increase in ψ at the peak of rainfall. Arrows denote the magnitude and direction of water flux vectors. Broken line in (a) and (d) has the same meaning as in Fig. 5.1b.

indicated that water mostly flowed downward., A transient saturated zone covered almost the whole slope at the soil-bedrock interface (Fig. 5.4b), whereas some points in the central and lower sections of the slope (i.e., C-5, D-5, 6, and E-3) remained unsaturated. Notably, a large increase in ψ was observed at six points (denoted by triangles in Fig. 5.4b). ψ values increased at least 50 cmH$_2$O at these points, coinciding with rainfall peaks (e.g., D-4 in Fig. 5.2b). As a result, a continuous high pressure zone (i.e., $\psi > 50$ cmH$_2$O) expanded from B-4 and passed through C-4 and D-3. However, the zone curved to the left because straight expansion toward the lower region was intercepted at E-3, where ψ showed a negative value. After the interception, the zone passed through D-4, E-4, and F-4 and then reached the lower end of the slope. In contrast, a high pressure zone also existed in the left section at C-6 and 7. However, expansion of the high pressure zone was intercepted by D-5 and 6, where ψ showed negative values. As a result, the left high pressure zone did not reach the lower end of the slope. Flux vectors indicated that water mostly flowed downward along the high pressure zones. The exfiltration flux existed in the left high pressure zone (i.e., C-6 and 7 in Fig. 5.4c) and in the lower part of the right high pressure zone (i.e., D-3). These points were located just above the D-5, 6, and E-3 points and remained unsaturated during a storm event (Fig. 5.4b). Infiltration flux occurred predominantly in the lower region of the slope.

In comparison with Figures 5.4a, 5.4b, and 5.4c, Figures 5.4d, 5.4e, and 5.4f illustrate the distributions of ψ in the middle layer, ψ at the soil–bedrock interface, and vertical flux value, respectively, at the peak of rainfall in 2011 (T4; 10:30 on 23 June 2011). A transient saturated zone expanded into upslope regions in the middle layer (Fig. 5.4d), including at E-3M, where ψ remained negative in 2009 (Fig. 5.4a). As in 2009, a large increase in ψ (denoted by triangles) was observed at C-3M and F-4M (Fig. 5.4a). However, large increase in ψ was observed at 13 points (denoted by triangles) at the soil–bedrock interface (Fig. 5.4e), whereas it was observed at six points in 2009 (Fig. 5.4b). In the right section of the slope, the continuous high pressure zone expanded from B-4 and passed through C-4, D-3, E-3, and F-3. Compared with 2009 (Fig. 5.4b), a large increase in ψ appeared at E-3 and F-3, and disappeared at D-4 (e.g., Fig. 5.2b and 5.2d) within the right high pressure zone. As a result, the right high pressure zone developed in a straight pattern. In the left section, the continuous high pressure zone started from B-9, passed through C-7, D-6, E-5, and F-4, and then reached the lower end of the slope. Compared with 2009 (Fig. 5.4b), a large increase in ψ appeared at B-9, D-6, and E-5 within the left high pressure zone. As a result, both high pressure zones converged in the lower region, resulting in a large ψ increase of up to 100 cm (e.g., E-5 in Fig. 5.2d).

Although flux vectors pointed upslope around the converging region (i.e., E-3 and 4), they mostly showed large values and pointed downward along the high pressure zones, indicating that a large quantity of water flowed toward the lower end of the slope through the zones. Exfiltration flux

existed in the whole area of the left high pressure zone (i.e., B-9, C-7, D-7 in Fig. 5.4f), lower part of the right high pressure zone (i.e., D-3), and in the converging region (i.e., E-3 to 5 and F-3). Such exfiltration flux along the high pressure zones indicates that excess pore water pressure was generated along the zones. These results indicate that preferential water channels (e.g., Uchida et al., 2001; Jones, 2010) were passing through these points, which were activated during the rainfall event and flushed a large quantity of water rapidly to the lower end of the slope. Additionally, a pipe produces the excess pressure in the surrounding soil when accumulated water exceeds transmission capacity (Roger and Selby, 1980; Pierson, 1983; Uchida, 2004).

Thus, the preferential water flow occurring at the soil–bedrock interface was intercepted at points D-5, 6, and E-3, in 2009 (Fig. 5.4b), whereas ψ remained negative during a rainfall event. In contrast, these three points showed a large increase in ψ in 2011(Fig. 5.4e) and a preferential channel was likely to be developed toward a lower direction. Such channel development was due to the erosive action of lateral water movement, which is one of the most important factors in pipe development (Tsukamoto et al., 1988; Brian and Jones, 1997; Holden, 2006). This is the first time that the development process of a preferential channel has been observed through multi-year observations of three-dimensional water flux. In contrast, the disappearance of the large ψ increase at D-4 (Fig. 5.4e) suggests that the right preferential channel developed straight from D-3 to E-3 and did not pass through D-4.

Exfiltration flux was detected in the converging region (i.e., E-3 to 5 and F-3; Fig. 5.4f) at the peak of rainfall in 2011. Although two channels were likely to develop by erosive action during the 3 years, the concentration of water exceeded the transmission capacity of the channels; thus, the excess water flowed upward into the middle layer, where hydraulic conductivity is higher than in the channels. Excess water was likely present in the converging region due to overabundant water accumulation in the two channels.

5.3.1.3 The hydrological process within the weathered bedrock layer

The detailed mechanism of water flow variations between 2009 and 2011 is shown clearly in Figure 5.5, which illustrates the distribution of ψ in vertical cross-section along the left high pressure zone, passing through A-8, B-9, C-7, D-6, E-5, and F-4 (denoted by broken line in Fig. 5.1a). Figures 5.5a and 5.5b show the distributions of ψ at the time points T1 and T2 in 2009 (Fig. 5.2a), and Figures 5.5c and 5.5d show the distributions of ψ at T3 and T4 in 2011 (Fig. 5.2c), respectively.

Under the no-rainfall conditions in 2009 and 2011 (Figs. 5.5a and 5.5c), the perched saturated area existed in the middle layer from C-7 to E-5, where flux vectors indicated the occurrence
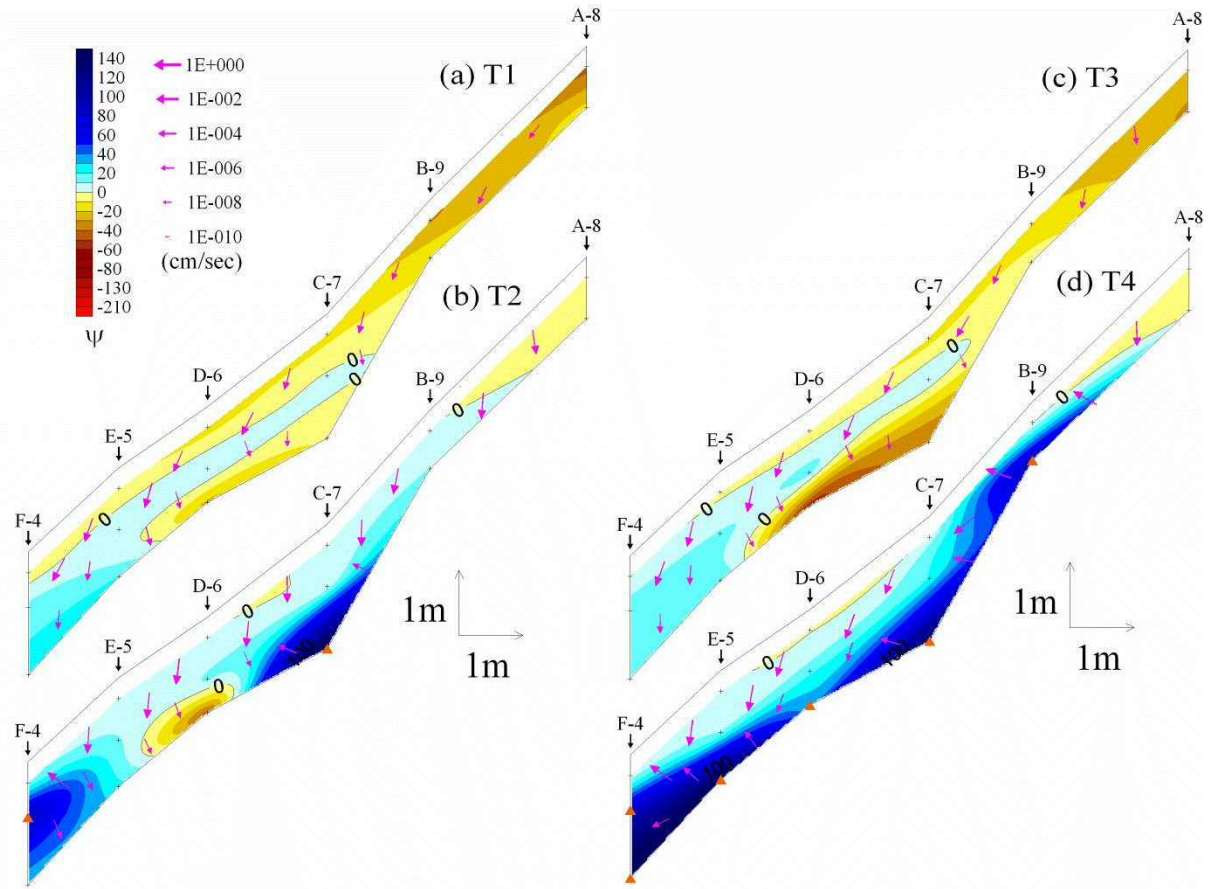
Fig. 5.3 Distributions of pressure head, ψ, in the vertical cross-section along the left high pressure zone denoted by the broken line in Fig. 5.1a at time points denoted in Figs. 5.2a and 5.2c: (a)T1, (b)T2, (c)T3, and (d)T4. Symbols and arrows have the same meaning as in Fig. 5.4.
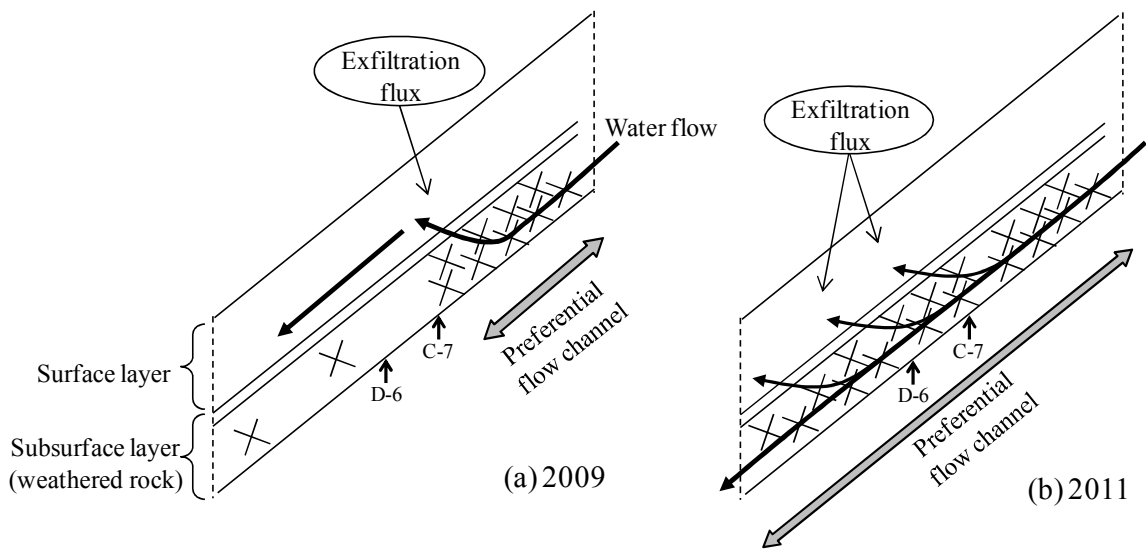

Fig. 5.6 Schematic illustrations of the hydrological process along the left preferential channel in (a) 2009 and (b) 2011.

of large lateral flow. Flux vectors indicated the occurrence of very small vertical infiltration in the unsaturated area beneath the perched water, indicating that the water mostly flowed above the middle layer, whereas very little infiltrated toward the bedrock surface under no-rainfall conditions. These results indicate that the soil layer in this area had low permeability, which prevents vertical infiltration of water. At the same time, the water-retaining capacity was low inside the layer. As described in Chapters 2 and 3, a relatively thick weathered bedrock layer (i.e., subsurface soil layer) exists below the surface soil layer at the study hillslope. The weathered bedrock showed lower hydraulic conductivity than did the surface soil (Fig. 2.4). However, previous studies have suggested that fractures in near-surface bedrock are distributed heterogeneously, creating large spatial variability in hydraulic conductivity (e.g., Montgomery et al., 1997, 2002). The development of a perched saturated area under no-rainfall conditions indicated that the weathered bedrock layer had low permeability, which prevented vertical infiltration of water in the upper part of the layer but resulted in low water-retaining capacity due to the fractures distributed heterogeneously inside the layer.

Notably, the preferential flow discussed above occurred within the weathered bedrock layer. At the peak of rainfall in 2009 (Fig. 5.5b), ψ exhibited a large increase at C-7 inside the layer, whereas ψ was unsaturated at D-6, indicating that the preferential flow channel was intercepted at D-6. The upward flux vectors at C-7 indicated that water ran upon the middle layer. In contrast, the high pressure zone continued above the bedrock surface from B-9 to F-4 in 2011 (Fig. 5.5d), where flux vectors pointed upward in almost the entire area due to excess water from the preferential water channel. These results indicate that lateral flow accumulating upslope flowed into fractures of the weathered bedrock layer and acted as preferential flow. Montgomery et al. (2002) also reported sharp and large ψ increases with exfiltrating hydraulic gradients during storm events in this layer, which showed a similar ψ waveform to our results (i.e., Fig. 5.2b and 5.2d). Variation in the distribution of the high pressure zone between 2009 and 2011 showed that the preferential flow channel through the fractures developed to pass through D-6 by weathering or erosive actions during the 3 years.

Figures 5.6a and 5.6b show schematic illustrations of the hydrological process along the left preferential channel in 2009 and 2011. Based on ψ and flux distributions in Fig. 5.5, we added the considerations of fracture development within the weathered bedrock layer. In 2009, the preferential flow channel within the fractures of weathered bedrock stopped at C-7 (Fig. 5.6a), where exfiltration flux was generated. Preferential flow above the bedrock surface did not reach D-6 because fractures within the weathered bedrock had not developed at D-6. In 2011(Fig. 5.6b), the preferential flow channel enlarged through the lower end of the slope because of the development of fractures and the erosive actions of water. As the volume of water exceeded the transmission capacity of the channel, the excess water flowed upward into the middle layer, showing an exfiltration flux.

5.3.2 Temporal variations in the hydrological process during 4 years

5.3.2.1 Seasonal variations in ψ and discharge data

Figure 5.7a summarizes the temporal variations in bedrock groundwater spring hydrograph in the old landslide scarp (left panel in Fig. 2.2) and trench flow (right panel in Fig. 2.2) from 2009 to 2011. Figures 5.7b and 5.7c also summarize the temporal variations in ψ values throughout the observation period from 2008 to 2011 at representative points: B-4, 5, C-1, and E-2 (Fig. 5.7b) and E-5 and F-3 (Fig. 5.7c). Hyetographs are also shown in Figures 5.7a, 5.7b, and 5.7c.

The bedrock groundwater spring hydrograph showed similar waveform to ψ values at B-4 and 5, which showed delayed dull peaks responding solely to heavy storm events. Particularly high ψ values and exfiltration flux were detected at B-4 and 5 under no-rainfall conditions (circles in Figs. 5.3b and 5.3e). Such delayed responses, only to heavy storm events, and gradual recession limbs are distinctive trends of bedrock groundwater level and seepage flow through bedrock fractures (Hirose et al., 1994; Onda et al., 2001; Katsura et al., 2008; Kosugi et al., 2008). These results confirmed that perennial groundwater was seeping from B-4 and 5 as in the bedrock spring of the scarp. ψ values remained positive throughout the observation period at E-2, and exhibited similar waveforms to B-4 and 5 except a slight variation of ψ. At C-1, ψ showed rapid peaks coinciding with rainfall peaks and a persistent decrease, with negative values during no-rain periods. These ψ responses to rainfall exhibited similar trends throughout the observation period from 2008 to 2011.

In contrast, the trend in ψ response varied during each rainfall event at points located within the preferential flow channel (e.g., D-4 and F-5; Figs. 5.2b and 5.2d). Figure 5.7c shows the temporal variations in ψ response throughout the observation period. ψ maintained uniform values at E-5, even during rainfall events, in 2008 and 2009. However, ψ spiked sharply and had quite high positive values (approximately 150 cmH$_2$O) in June and July 2010, coinciding with individual rainfall peaks. After August 2010, the peak ψ values decreased gradually, regardless of rainfall intensity. The peak ψ values showed quite high positive values again in 2011. Conversely, ψ spiked sharply and had quite high positive values (approximately 200 cmH$_2$O) at F-3, coinciding with individual rainfall peaks in 2008. However, peak ψ values decreased in 2009 and 2010, regardless of rainfall intensity. Finally, ψ spike response completely disappeared and ψ values remained uniform in 2011. These temporal alternations in the peak ψ values were independent of rainfall intensity.

Thus, the ψ spike response appeared and disappeared year by year, whereas other points exhibited similar ψ responses throughout the observation period. Additionally, the peak ψ spike response values increased and decreased irregularly each year.
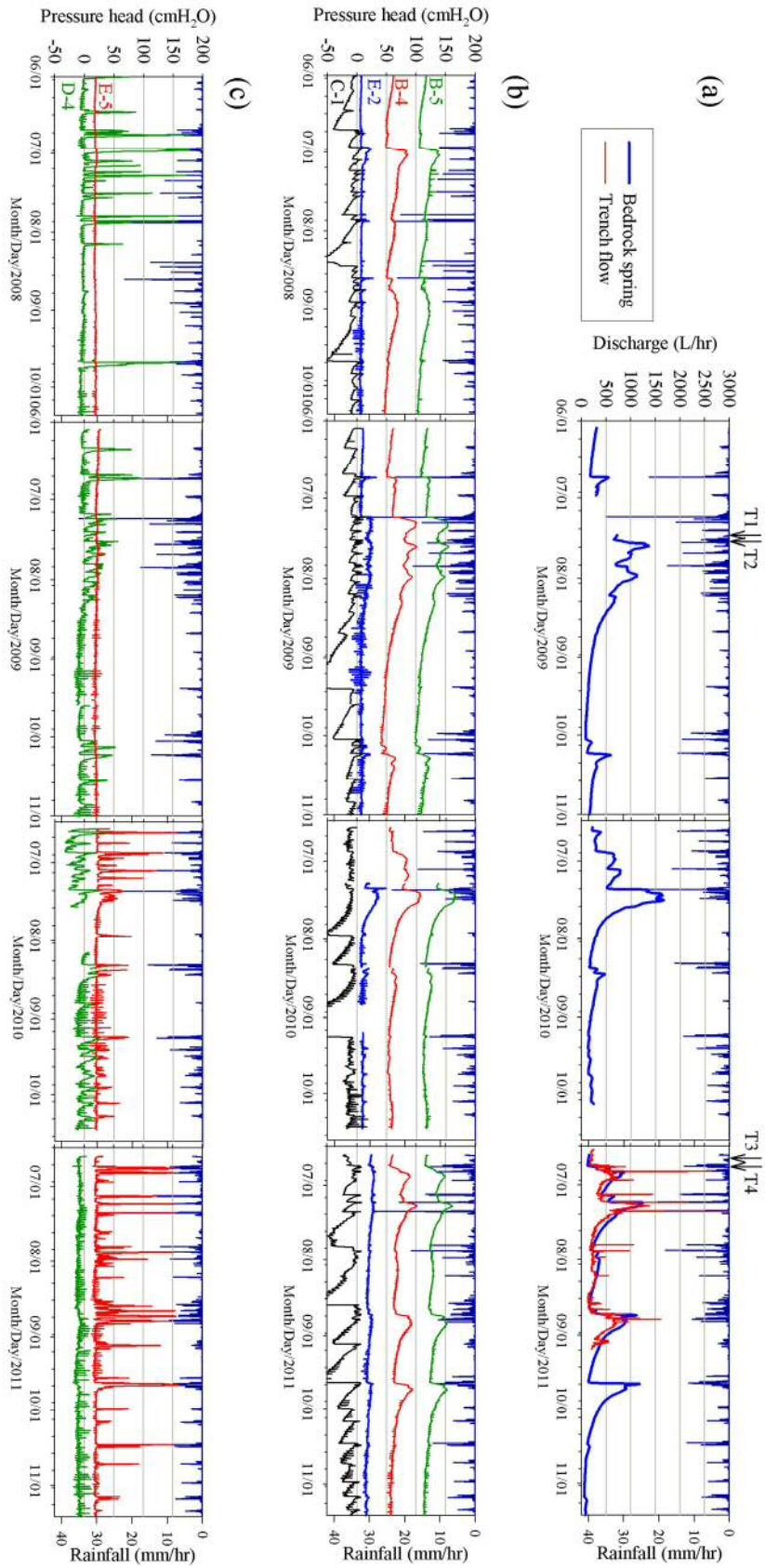
Fig. 5.7 (a) Temporal variations in the hydrograph of a bedrock groundwater spring in the old landslide scarp and trench flow from 2009 to 2011. Temporal variations in pressure head, ψ, throughout the observation period in 2008–2011 at representative points: (b) B-4, B-5, C-1, and E-2 and (c) E-5 and F-3. Hyetographs are also shown in (a), (b), and (c).

5.3.2.2 Temporal variations in the ψ spike response

Figure 5.8 demonstrates a simplification in the magnitude of the ψ spike response at E-5. Figure 5.8a shows the temporal variation in ψ and the hyetograph for 4 years at E-5 (same as E-5 in Fig. 5.7c). First, the amount of increase in ψ ($\Delta\psi$) was calculated by subtracting the base value from the raw ψ values. The base ψ value was fixed to the ψ value under dry conditions, which remained almost the same throughout the observation period: e.g., 20 cmH_2O at E-5 and -5 cmH_2O at D-4 (Fig. 5.7c). Because active water movement, such as preferential flow, occurs only in positive pressure areas, we set the base ψ value to 0 for points with a negative base value. Second, $\Delta\psi$ was divided by the maximal $\Delta\psi$ value throughout the observation period ($\Delta\psi_{max}$) to estimate the magnitude of ψ increase. Figure 5.8b shows the temporal variation in the magnitude of increase ($\Delta\psi$ / $\Delta\psi_{max}$) at E-5. Then, we classified the magnitude of the ψ spike response into three types based on $\Delta\psi$ / $\Delta\psi_{max}$ as follows: $0 \leq (\Delta\psi / \Delta\psi_{max}) < 0.2$ for no response, $0.2 \leq (\Delta\psi / \Delta\psi_{max}) < 0.6$ for a small response, and $0.6 \leq (\Delta\psi / \Delta\psi_{max}) \leq 1$ for a large response. Figure 5.8c shows the resulting simplified magnitude of the ψ spike response at E-5.
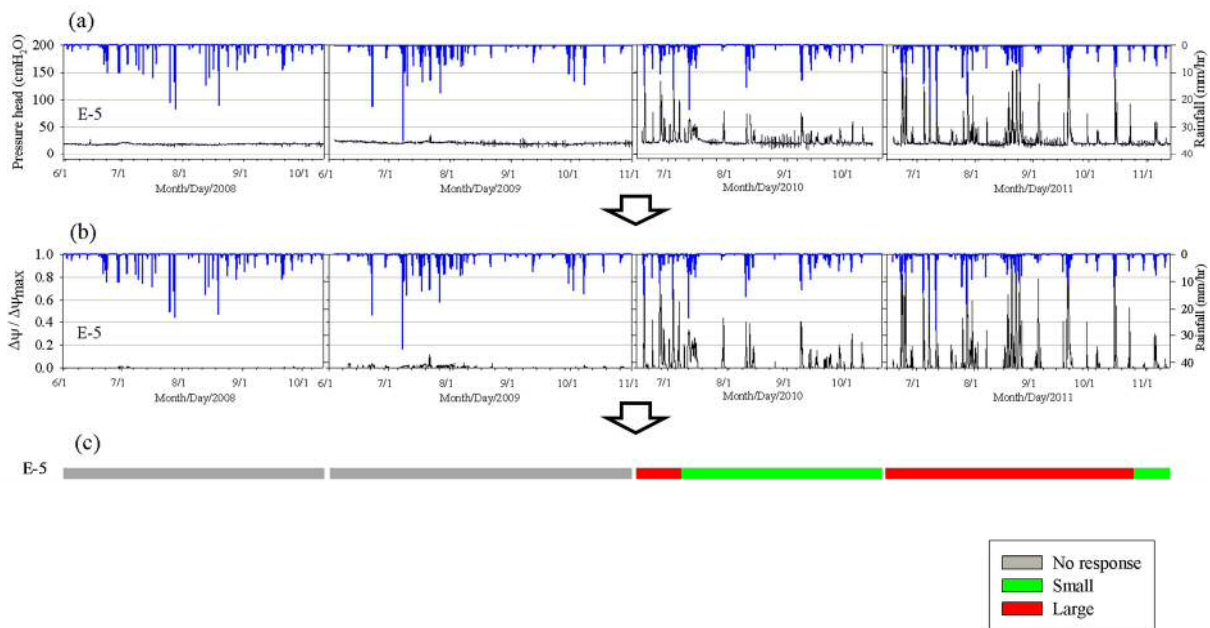

Fig. 5.8 An example demonstrating the process for simplifying the magnitude of the pressure head, ψ, spike response at E-5. (a) Temporal variation in ψ and hyetograph for 4 years at E-5. (b) Temporal variation in the magnitude of increase ($\Delta\psi$ / $\Delta\psi_{max}$) at E-5. (c) Simplified magnitude of the ψ spike response at E-5.
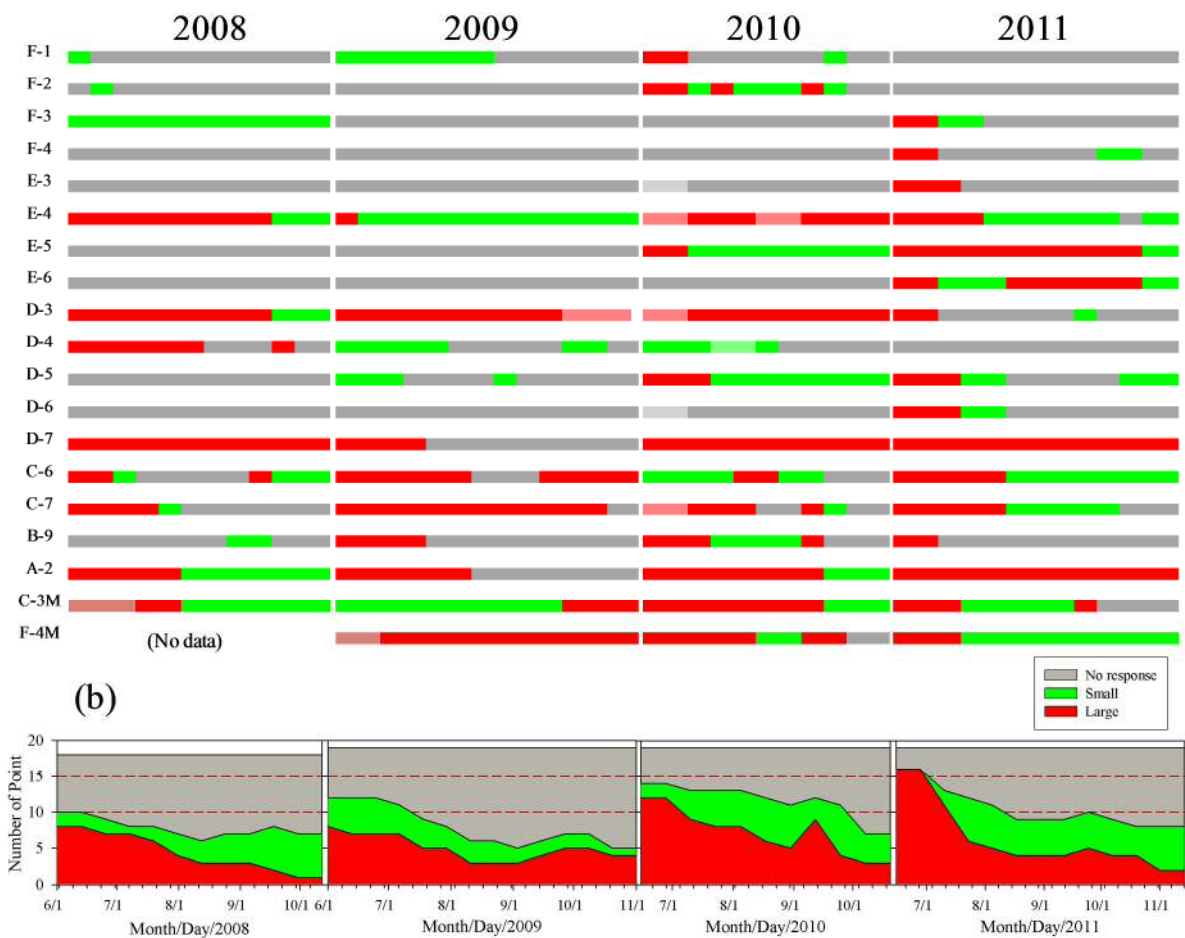
Fig. 5.9 (a) Simplified magnitude of the pressure head, ψ, spike response at 19 points throughout the entire observation period from 2008 to 2011. (b) Temporal variation in the number of points that exhibited large, small, and no ψ spike response from 2008 to 2011.

Figure 5.9a summarizes the simplified magnitude of the ψ spike response at 19 points throughout the entire observation period from 2008–2011, following the process shown in Figure 5.7a–c. Annual variations indicated that the response had appeared during the observation period at some points: e.g., at E-5, although no response was detected until 2009. Subsequently, ψ exhibited a large response in the first part of 2010 and most of 2011. Conversely, although ψ exhibited a large response in 2008 at D-4, only a small response was detected in 2009 and 2010. Finally, no response was detected in 2011. Moreover, the large, small, and no responses switched frequently within a year.

Figure 5.9b summarizes the temporal variation in the number of points that exhibited large, small, and no response from 2008 to 2011. The number of points that showed a large or small response tended to increase year by year, indicating that the preferential flow channels were enlarged by development of fractures and the erosive actions of water within the weathered bedrock layer. Rock

fractures generally develop due to physical weathering processes, such as freeze-thaw cycles (e.g., Nicholson and Nicholson, 2000). A sediment production process due to freeze-thaw cycles during the winter has been observed for many years on bare slopes located near the study hillslope (e.g., Fujita et al., 2005). On the other hand, previous studies have documented the change in soil hydraulic conductivity caused by freeze-thaw cycles. Cracks that develop during freeze-thaw cycling increase hydraulic conductivity because preferential flow occurs through the crack network (e.g., Othman and Benson, 1993). Thus, freeze-thaw cycling created fractures within the weathered bedrock layer at the study site during three winter seasons throughout the observation period. However, the number and proportion of large responses tended to decrease over time in each year (Fig. 5.9b). Fine particles may have been stuck within the fractures of weathered bedrock and washed out by water flow from spring to fall, resulting in improved transmission capacity of the channel. Fine particles are likely to have been generated within the fractures during freeze-thaw cycling in winter.

Thus, freeze-thaw cycles seem to play an important role in fracture development in the weathered bedrock layer. However, we did not obtain ψ data when freeze-thaw cycles occurred because we stopped observations under snowfall and the low tempretures of winter. Furthermore, no previous study has reported a change in rock hydraulic conductivity due to freeze-thaw cycles, although many soil studies have been conducted. Future studies should conduct ψ observations during the winter season using heaters to prevent tensiometers failure.

5.3.2.3 Temporally variable flow area

Figures 5.10a and 5.10b plot the location of all points showing ψ spike responses at the soil–bedrock interface. Figures 5.10a and 5.10b also illustrate the distribution of ψ in the middle layer and at the soil–bedrock interface, respectively, before the beginning of rainfall (T3; same as Fig. 5.3d and 5.3e). As shown in Fig. 5.9a, not all points exhibited a ψ spike response every year. Based on the existence or non-existence of responses in 2008 and 2011 (Fig. 5.9a), the points were classified into three types: responses existed (x) in both 2008 and 2011 (denoted by closed squares in Figs. 5.10a and 5.10b), (y) in 2011 but not in 2008 (denoted by open squares), and (z) in 2008 but not in 2011 (denoted by crosses). The connected area showing type (x) (e.g., D-3, E-4, and F-3) indicates that preferential flow occurred constantly throughout the observation period in that area. In the area showing type (y), the preferential flow channel was generated during the observation period by the development of fractures and erosive actions within the weathered bedrock layer. Conversely, the preferential channel transferred to another point in the type (z) area because the preferential channel developed straight during the observation period (e.g., D-4).
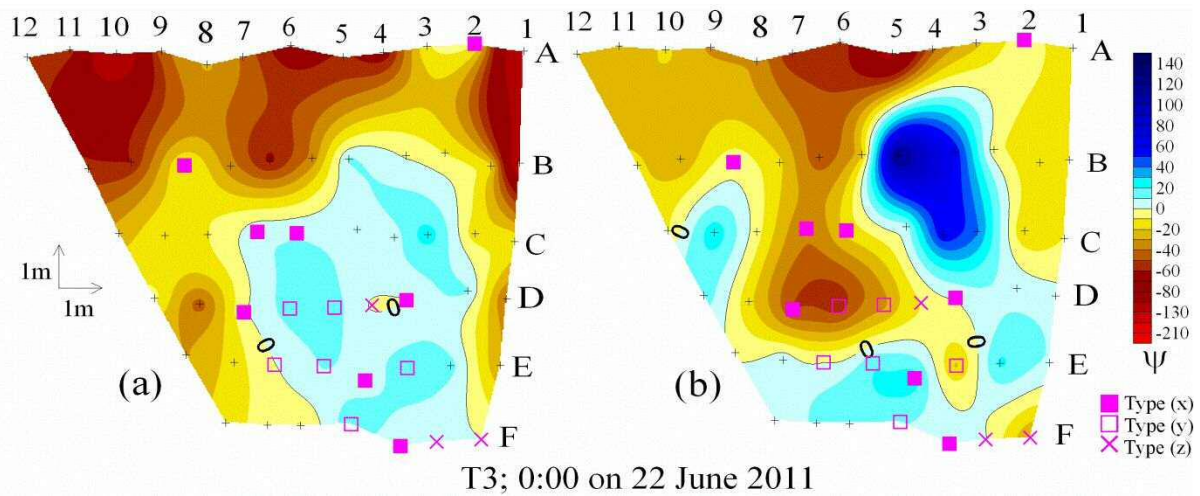
Fig. 5.10 Location and classification of all points that showed the pressure head, ψ, spike response at the soil–bedrock interface. Closed squares denote type (x): responses existed in both 2008 and 2011. Open squares denote type (y): responses occurred in 2011 but not in 2008. Crosses denote type (z): responses occurred in 2008 but not in 2011. Background colors show the distribution of ψ (a) in the middle layer and (b) at the soil–bedrock interface, respectively, at time point T3, denoted in Fig. 5.2c.

On the other hand, the location of points including types (x), (y), and (z) clearly corresponded to the points where ψ showed negative values at the soil–bedrock interface (Fig. 5.10b) and perched water was detected in the middle layer (Fig. 5.10a) under no-rainfall conditions (i.e., C-6, 7, D-3 to 7, and E-3). This result indicated that the fractured and weathered bedrock layer existed in this area because both perched water and preferential flow channel are distinctive characteristics of the weathered bedrock layer (discussed in Figs. 5.5 and 5.6). Montgomery et al. (2002) reported that the weathered and fractured bedrock layer significantly affected hillslope hydrological processes; lateral saturated drainage through the layer may lead to locally elevated ψ values and exfiltration flux. However, the temporal variability in the preferential flow domain within the layer has not been documented previously. We determined that this area acts as preferential flow domain, divided into three different temporal patterns described as types (x), (y), and (z). The hydrological processes in this area are critical to generate runoff and create shallow landslides because the temporal variation in preferential flow domain should induce an unexpected local increase in ψ. In this study, we revealed such a temporally variable flow area for the first time by multi-year observations of three-dimensional water flux.

5.4 Conclusions

We analyzed long-term three-dimensional water movement data obtained by intensive tensiometer nests to trace temporal variations in the hydrological process. First, we compared pressure head, ψ, variations between 2009 and 2011. The shapes of saturated areas and the directions of flux vectors under no-rainfall condition in 2011 showed a similar trend to that in 2009, indicating that the water flow domain under a no-rainfall condition varied only slightly from 2009 to 2011. In contrast, the ψ response to the rainfall event in 2009 was dramatically different from that in 2011, particularly at the soil–bedrock interface. Compared with 2009, continuous high pressure zones (i.e., $\psi > 50$ cmH$_2$O) generated above the bedrock surface developed straight toward the lower end of the slope in 2011. Direction and flux vector values indicated that the high pressure zones were an activated preferential water channel that appeared during rainfall events. This result indicated that the preferential channel likely developed due to the erosive action of lateral water movement from 2009 to 2011. Moreover, preferential channels were detected where a perched saturated area existed in the middle layer, indicating that preferential flow occurred within fractures of the weathered bedrock layer. Fractures were developed by erosive action and weathering from 2009 to 2011 (Figs. 5.6a and 5.6b).

Secondly, we focused on seasonal variations in ψ values throughout the observation period from 2008 to 2011. ψ spiked sharply and had quite high positive values at points located within the preferential flow channel. However, the ψ spike response appeared and disappeared year by year and the peak values increased and decreased irregularly each year independent of rainfall intensity, whereas other points exhibited similar ψ responses throughout the observation period.

The ψ spike response was observed at 19 points throughout the entire observation period of 2008 to 2011. However, not all points exhibited a ψ spike response every year. While preferential flow occurred constantly throughout the observation period in one area, a preferential flow channel was generated during the observation period in other areas. Conversely, the preferential channel was transferred to another point because it developed straight in other areas. The number of points showing a ψ spike response tended to increase year by year, indicating that the preferential flow channels were enlarged by development of fractures. However, the number of points showing a ψ spike response tended to decrease and the peak values tended to get smaller over time within each year, suggesting that fine particles stuck within the fractures of weathered bedrock were washed by water flow from spring to fall, thereby improving the channel transmission capacity.

This study revealed the temporal variation in the hydrological process due to preferential channel development by the erosive action of lateral flow and weathering of fractured bedrock. The effect of freeze-thaw cycles on variation in the hydrological process should be assessed by ψ observations during the winter season.

References

Bryan R.B., and J.A.A. Jones. 1997. The significance of soil piping process: inventory and prospect. Geomorphology 20: 209-218.

Freer, J., J.J. McDonnell, K.J. Beven, N.E. Peters, D.A. Burns, R.P. Hooper, B. Aulenbach, and C. Kendall. 2002. The role of bedrock topography on subsurface storm flow, Water Resour. Res. 38(12): 1269, doi: 10.1029/2001WR000872.

Fujita, M., T. Sawada, M. Shida, and M. Itoh. 2005. Characteristics on sediment production in the Takahara river basin. Annual J. Hydraulic Engineering JSCE 49: 1075-1080 (in Japanese with English summary).

Hirose T., Y. Onda, and Y. Matsukura. 1994. Runoff and solute characteristics in four small catchments with different bedrocks in the Abukuma mountains. Transactions, Jpn. Geomorphol. Uni. 15A: 31-48.

Holden, J. 2006. Sediment and particulate carbon removal by pipe erosion increase over time in blanket peatlands as a consequence of land drainage. J. Geophys. Res. 111, F02010, doi: 10.1029/2005JF000386.

Jones, J.A.A. 2010. Soil piping and catchment response. Hydrol. Process. 24: 1548-1566, doi: 10.1002/hyp.7634.

Katsura, S., K. Kosugi, T. Mizutani, S. Okunaka, and T. Mizuyama. 2008. Effects of bedrock groundwater on spatial and temporal variations in soil mantle groundwater in a steep granitic headwater catchment. Water Resour. Res. 44: W09430, doi: 10.1029/2007WR006610.

Kosugi, K., S. Katsura, T. Mizuyama, S. Okunaka, and T. Mizutani. 2008. Anomalous behavior of soil mantle groundwater demonstrates the major effects of bedrock groundwater on surface hydrological processes. Water Resour. Res. 44: W01407, doi: 10.1029/2006WR005859.

McDonnell, JJ. 1990. The influence of macropores on debris flow initiation. Quarterly J. Engineering Geology 23: 325–331.

Montgomery, D.R., W.E. Dietrich, R. Torres, S.P. Anderson, J.T. Heffner, and K. Loague. 1997. Piezometric response of a steep unchanneled valley to natural and applied rainfall. Water Resour. Res. 33: 91-109.

Montgomery, D.R., W.E. Dietrich, and J.T. Heffner. 2002. Piezometric response in shallow bedrock at CB1: Implications for runoff generation and landsliding. Water Resour. Res. 38(12): 1274, doi: 10.1029/2002WR001429.

Nicholson, D.T., and F.H. Nicholson. 2000. Physical deterioration of sedimentary rocks subjected to experimental freeze-thaw weathering. Earth Surf. Process. Landforms 25: 1295-1307.

Olofsson, B. 1994. Flow of groundwater from soil to crystalline rock. Hydrogeol. J. 2(3):71-83, doi: 10.1007/s100400050052.

Onda, Y., Y. Komatsu, M. Tsujimura, and J. Fujihara. 2001. The role of subsurface runoff through bedrock on storm flow generation. Hydrol. Process. 15:1693-1706, doi: 10.1002/hyp.234.

Othman M.A., and C.H. Benson. 1993. Effect of freeze-thaw on the hydraulic conductivity and morphology of compacted clay. Canadian Geotechnical J. 30(2): 236-246. doi: 10.1139/t93-020.

Pierson, T.C. 1983. Soil pipes and slope stability. Quarterly J. Engineering Geology 16: 1–11.

Roger N.W., and M.J. Selby. 1980. Mechanisms of shallow translational landslide during summer rainstorm: North Island, New Zealand. Geografiska Annaler 62A: 11–21.

Sidle, R.C., H. Kitahara, T. Terajima, and Y. Nakai. 1995. Experimental studies on the effects of pipeflow on throughflow partitioning. J. Hydrol. 165: 207-219.

Tsukamoto, Y., H. Minematsu, and I. Tange. 1988. Pipe development in hillslope soils in humid climate. Rolling Land Res. 6: 268-280 (in Japanese with English summary).

Uchida, T., K. Kosugi, and T. Mizuyama. 2001. Effects of pipeflow on hydrological process and its relation to landslide: a review of pipeflow studies in forested headwater catchments. Hydrol. Process. 15: 2151-2174, doi: 10.1002/hyp.281.

Uchida, T., Y. Asano, T. Mizuyama, and J.J. McDonnell. 2004. Role of upslope soil pore water pressure on subsurface stormflow dynamics. Water Resour. Res. 40(12), doi: 10.1029/2003WR002139.

CHAPTER 6

Conclusions

Heterogeneous hydrological properties in the foot slope area of mountainous hillslopes should be assessed to gain an understanding of hydrological phenomena and their effects on water flow and sediment transport. Intensive observation of water flux by using tensiometers is the most reliable way of analyzing heterogeneous hydrological phenomena. However, intensive observations using dense tensiometer nests have not been conducted in previous studies due to the lack of a measurement technique to detect the existence of heterogeneous hydrological properties hidden locally within a slope.

The objectives of this study were (1) to detect the existence of heterogeneous hydrological properties by using a new combined penetrometer-moisture probe (CPMP) (Chapter 3), (2) to clarify the detailed three-dimensional water movement by using tensiometer nests to construct a physics-based model for estimating the hydraulic properties inversely (Chapter 4), and (3) to investigate the temporal variation of hydrological properties by long-term observation (Chapter 5).

In Chapter 3, the new CPMP was applied to investigate the hydrological properties in a foot slope area by simultaneous measurements of the soil water content, θ, and the penetration resistance, N_c, of soil mantles. Using the CPMP, we obtained detailed spatial patterns of θ within the slope as well as soil thickness distributions for calculating the topographic indices. By comparing the topographic indices and θ, we could effectively detect the heterogeneous water distribution that exists independently of topographic flow convergence. The CPMP data corresponded well with pressure head values, ψ, observed using tensiometers under a no-rainfall condition. The distribution of saturated areas with concentrated soil water flux corresponded well with the high θ regions observed using the CPMP, indicating that we can estimate the complex shape of the hydrological base line and water flow domain from CPMP measurements without measuring ψ using tensiometers and soil hydraulic conductivity by collecting soil samples. Moreover, the CPMP successfully located a point of bedrock groundwater exfiltration which was otherwise hidden in the studied hillslope because it could detect a sudden increase in θ in the low-permeability subsurface layer. During a heavy rainfall event, preferential water flow was assumed to occur within the region where high θ values at the bedrock surface were observed by the CPMP. At points where the CPMP data indicated a thick subsurface layer with medium water content below a surface layer with large water content, intensive rainwater infiltration shifted the hydrological base line from the boundary between the surface and subsurface

layers to the bottom of the subsurface layer. Thus, complicated water movement phenomena during a storm event in a foot slope area can be inferred from the penetration resistance and water content distributions simultaneously measured by the CPMP under a no-rainfall condition.

In Chapter 4, high-resolution and three-dimensional water movement data obtained using intensive tensiometer nests were analyzed to clarify the hydrological process including heterogeneous phenomena in detail. Under a no-rainfall condition, perennial groundwater seepage was detected by exfiltration flux and temporal ψ waveforms, which showed delayed responses, only to heavy storm events, and gradual recession limbs. The seepage water spread toward the downslope direction and supplied water constantly to the lower section of the slope. At some points at the center of the slope, a perched saturated area was detected in the middle layer, while ψ exhibited negative values above the bedrock surface. At the peak of a rainfall event, continuous high pressure zones (i.e., ψ > 50 cmH₂O) were generated in the right and left sections of the slope. Both high pressure zones converged at a lower region, showing a sharp ψ spike up to 100 cmH₂O. Along the high pressure zones, flux vectors showed large values and water exfiltration, indicating the occurrence of preferential flow. Moreover, the preferential flow occurred within the area beneath the perched water, indicating the existence of a weathered bedrock layer. This layer had low permeability, which prevents vertical infiltration of water, in upper part of the layer but had high permeability due to fractures distributed heterogeneously inside the layer. The fractures act as preferential flow channels and flush the water derived from lateral flows accumulated from the upslope area during a rainfall event. To reproduce the observed heterogeneous ψ distributions, the spatial distribution of hydraulic properties were estimated and assigned to the physics-based three-dimensional simulation model. A base flow volume, which was estimated from both the observed trench flow and the ψ waveform at the groundwater seepage point, was assigned to the source terms. The weathered bedrock layer was represented by stratified soils having high and low hydraulic conductivities. The resulting model calculations reproduced well the observed heterogeneous ψ distributions, such as the bedrock groundwater seepage, under a no-rainfall condition. Moreover, the model calculations successfully reproduced the hydrological process during a rainfall event, where water flowed into the weathered bedrock layer through water intakes and the accumulated water generated excess pore water pressure at the lower section of the slope.

In Chapter 5, long-term three-dimensional water movement data obtained using intensive tensiometer nests (Chapter 4) were analyzed to trace the temporal variation of the hydrological process. Firstly, we made a comparison between the ψ variations in 2009 and 2011. The water flow domain under a no-rainfall condition varied only slightly from 2009 to 2011. On the other hand, the response of ψ to the rainfall event in 2009 was drastically different from that in 2011, particularly at the soil-bedrock interface. Compared to 2009, continuous high pressure zones were generated above the

bedrock surface, leading directly to the lower end of the slope in 2011. This result indicated that preferential channels were likely to develop due to the erosive action by lateral water movement and the weathering of fractures within the weathered bedrock layer from 2009 to 2011. At points located within preferential flow channels, ψ spiked sharply with considerably high positive values. The spike response of ψ was observed at 19 points throughout the whole observation period from 2008 to 2011. However, not all points exhibited a ψ spike response every year. While preferential flow occurred constantly throughout the observation period in one area, a preferential flow channel was generated during the observation period in another area. Conversely, the preferential channel in one area altered its course to pass another point because a preferential channel developed directly in another area. Overall, the number of points that showed a ψ spike response tended to increase every year, indicating that the preferential flow channels had been enlarged by the development of fractures. On the other hand, the number of points tended to decrease and the peak values tended to get smaller over time every year. It is possible that fine particles stuck within the fractures of the weathered bedrock was washed out by water flow from spring to fall and the transmission capacity of the channel was improved.

In this study, the three-dimensional hydrological process, including heterogeneous phenomena, in the studied hillslope was clarified using densely nested tensiometers, supported by CPMP observations. The heterogeneous hydrological properties, such as water supply and spatial distribution of hydraulic conductivities, were estimated and well reproduced by model calculations. Moreover, the temporal variation in hydrological properties due to preferential channel development by the erosive action of lateral flows and the weathering of fractured bedrock was clarified. The new CPMP technique proposed in this study enables intensive observations at various sites, accelerating the progress of studies on heterogeneous hydrological properties. The results obtained in this study will contribute to the improvement of runoff/landslide prediction that takes into account (i.e., spatially- and temporally-) heterogeneous hydrological properties.

ACKNOWLEDGEMENTS

January 2012

Naoya Masaoka